21

Purely irrotational theories of stability of viscoelastic fluids

As in the case of viscous fluids, very good approximations to exact results for viscoelastic fluids can be obtained from purely irrotational studies of stability. Here we consider RT instability (§21.1) and capillary instability (§21.2) of an Oldroyd B fluid. Viscoelastic effects enter into the irrotational analysis of RT instability through the normal stress at the free surface. For capillary instability, the short waves are stabilized by surface tension, and an irrotational viscoelastic pressure must be added to achieve excellent agreements with the exact solution. The extra pressure gives the same result as the dissipation as is true in viscous fluids where VPF works for short waves and VCVPF and DM give the same results for capillary instability.

21.1 Rayleigh-Taylor instability of viscoelastic drops at high Weber numbers

Movies of the breakup of viscous and viscoelastic drops in the high-speed airstream behind a shock wave in a shock tube have been reported by Joseph, Belanger and Beavers (1999). They performed a Rayleigh-Taylor stability analysis for the initial breakup of a drop of Newtonian liquid and found that the most unstable Rayleigh-Taylor wave fits nearly perfectly with waves measured on enhanced images of drops from the movies, but the effects of viscosity cannot be neglected. Here we construct a Rayleigh-Taylor stability analysis for an Oldroyd-B fluid using measured data for acceleration, density, viscosity and relaxation time λ_1. The most unstable wave is a sensitive function of the retardation time λ_2 which fits experiments when $\lambda_2/\lambda_1 = O(10^{-3})$. The growth rates for the most unstable wave are much larger than for the comparable viscous drop, which agrees with the surprising fact that the breakup times for viscoelastic drops are shorter. We construct an approximate analysis of Rayleigh-Taylor instability based on viscoelastic potential flow which gives rise to nearly the same dispersion relation as the unapproximated analysis.

21.1.1 Introduction

Aitken and Wilson (1993) studied the problem of the stability to small disturbances of an incompressible elastic fluid above a free surface. They derived dispersion relations for an Oldroyd fluid in the case where the fluid is bounded below by a rigid surface. When the retardation time and inertia are neglected the analysis predicts an unbounded growth rate at a certain Weissenberg number. The addition of inertia or retardation smooths this singularity. The work presented here differs from that of Aitken and Wilson in the following ways; in our work the two fluids are unbounded; we construct both an exact analysis and an approximate analysis based on potential flow; we aim to apply the analysis of Rayleigh-Taylor instability of viscoelastic drops using measured data; we compute and present dispersion relations emphasizing the role of the most dangerous wave associated with the maximum growth rate, thereby emphasizing the role of the huge acceleration in the drop breakup problem due to Rayleigh-Taylor instability; and we use the maximum growth rate to define a breakup time.

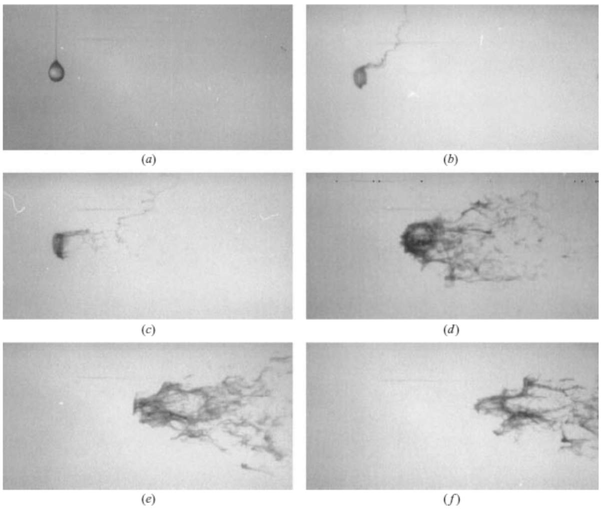

Fig. 21.1. Stages in the breakup of a drop of 2% aqueous solution of polyox (WSR 301; diameter = 2.9 mm) in the flow behind a Mach 2 shock wave. Air velocity = 432 m s^{-1}; dynamic pressure = 165.5 kPa; Weber number =15,200. Time (μs): (a) 0, (b) 55, (c) 95, (d) 290, (e) 370, (f) 435.

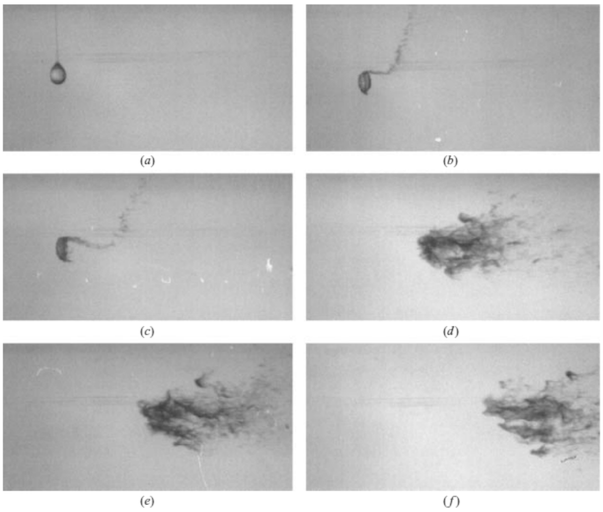

Fig. 21.2. Stages in the breakup of a drop of 2% aqueous solution of polyox (WSR 301; diameter = 2.9 mm) in the flow behind a Mach 3 shock wave. Air velocity = 755 m s^{-1}; dynamic pressure = 587.2 kPa; Weber number =54,100. Time (μs): (a) 0, (b) 30, (c) 45, (d) 170, (e) 195, (f) 235.

21.1.2 Experiments

21.1.2.1 Displacement-time graphs and accelerations

Displacement vs. time graphs for the Mach 3 experiments are shown in figure 21.5. The Mach 2 graphs are of similar form. The distance refers to the slowest moving drop fragment (the windward stagnation point); other parts of the fragmenting drop accelerate from rest even more rapidly. The graphs are nearly perfect parabolas for about the first 200 μs of the motion, which allows the initial acceleration to be obtained by fitting a curve of the form $x - x_o = \alpha(t - t_o)^2$. Values of the parameters α, t_o, x_o, and the initial acceleration are listed in table 21.2. It is noteworthy that in these graphs the acceleration is constant, independent of time for small times, and about 10^4-10^5 times the acceleration due to gravity depending upon the shock wave Mach number. In general there is a moderate decrease in acceleration with time over the course of the several hundred microseconds that it takes to totally fragment the drop.

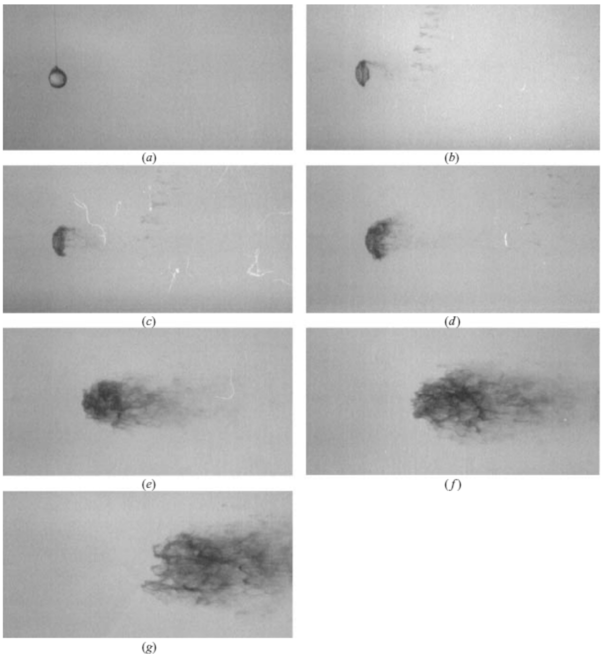

Fig. 21.3. Stages in the breakup of a drop of 2% aqueous solution of polyacrylamide (Cyanamer N-300LMW; diameter =3.2 mm) in the flow behind a Mach 3 shock wave. Air velocity = 771 m s^{-1}; dynamic pressure = 578.1 kPa; Weber number =82,200. Time (μs): (a) 0, (b) 45, (c) 60, (d) 90, (e) 145, (f) 185, (g) 225.

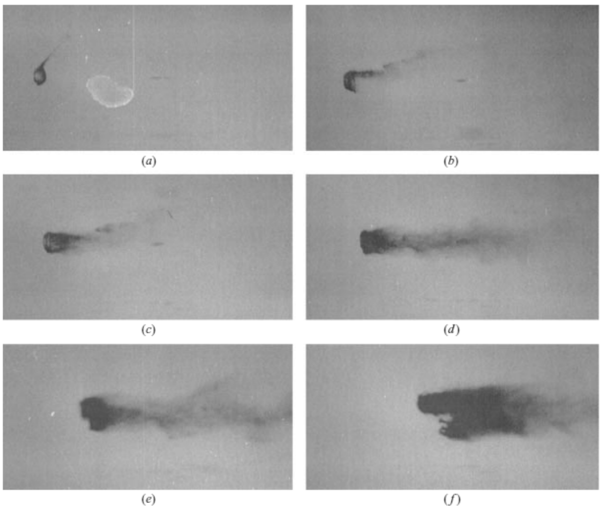

Fig. 21.4. Stripping breakup of a drop of 1 kg m^{-1} s^{-1} silicone oil (diameter = 2.6 mm) in the flow behind a Mach 3 shock wave. Air velocity = 767 m s^{-1}; dynamic pressure = 681.0 kPa Weber number =168,600. Time (μs): (a) 15, (b) 40, (c) 50, (d) 80, (e) 115, (f) 150.

The initial accelerations are an increasing function of the shock Mach number; the dynamic pressure which accelerates the drop increases with the free-stream velocity. At a fixed free-stream dynamic pressure there appears to be a tendency for the acceleration to decrease with drop size. If we take the drag on a spherical drop to be proportional to the drop diameter squared and the mass to the diameter cubed, then the acceleration is proportional to D^{-1} and decreases with increasing D.

(a) Liquid	Diameter (mm)	Viscosity (kg m^{-1} s^{-1})	Surface tension (N m^{-1})	Density (kg m^{-}3)	Relaxation time (s)	*Oh*	
Newtonian							
SO 1000	2.6	1	0.021	969		4.3	
Viscoelastic							
2% PO	2.9	35	0.063	990	0.21	82.3	
2% PAA	3.2	0.96	0.045	990	0.039	2.5	
(b) Liquid	Velocity (m s^{-1})	Density (kg m^{-3})	Pressure (kPa)	Dynamic pressure (kPa)	*T*2 temp (K)	Weber no. ($\times 10^3$)	Reynolds no. ($\times 10^3$)	Shock *M*
Newtonian								
SO 1000	438.8	1.876	269.2	180.6	502	44.7	80.6	2.03
SO 1000	767.4	2.312	523.7	681.0	792	168.6	129.1	3.02
Viscoelastic								
2% PO	431.7	1.776	252.3	165.5	497	15.2	84.2	2.01
2% PO	754.8	2.061	458.7	587.2	778	54.1	127.6	2.98
2% PAA	770.6	1.947	442.9	578.1	795	82.2	134.0	3.03

21.1. Experimental parameters: (a) liquid properties, (b) free-stream conditions. Relaxation time for PO and PAA are computed from measured values taken on the wave-speed meter, PO in the tables given by Joseph (1990) and PAA in Liu (1995).

Table 21.1.

21.1.3 Theory

The fluid mechanics of RT instability in an Oldroyd B fluid is controlled by acceleration as is true for viscous fluids discussed in chapter 9. The theoretical background discussed there works well for the problem here. Ortiz *et al.* 2003 developed a correlation for the acceleration of a liquid drop suddenly exposed to a high speed air stream. The correlation depends weakly on the viscosity through the Ohnesorge number and though it works also very well for viscoelastic drops, no viscoelastic parameter enters.

Liquid	Silicone oil		2% Aqueous PO		2% Aqueous PAA
Viscosity (kg m^{-1} s^{-1})	1	1	35	35	0.96
Shock Mach no.	2	3	2	3	3
α (m s^{-2})	1.463×10^5	5.561×10^5	0.687×10^5	3.240×10^5	2.461×10^5
x_0 (m)	-28.5×10^{-5}	7.45×10^{-5}	-17.7×10^{-5}	-0.046×10^{-5}	-6.16×10^{-5}
$t_0(s)$	-3.43×10^{-5}	0.21×10^{-5}	-5.07×10^{-5}	-0.12×10^{-5}	-1.49×10^{-5}
Initial acceleration (m s^{-2})	2.92×10^5	11.12×10^5	1.37×10^5	6.48×10^5	4.92×10^5
Max. accel. ($c = 0$) (m s^{-2})	1.07×10^5	4.05×10^5	0.86×10^5	3.07×10^5	2.74×10^5
Mean accel./ max. accel.	2.7	2.7	1.6	2.1	1.8

Table 21.2. *Curve-fitting parameters and initial accelerations for the liquid drops specified in table 21.1.*

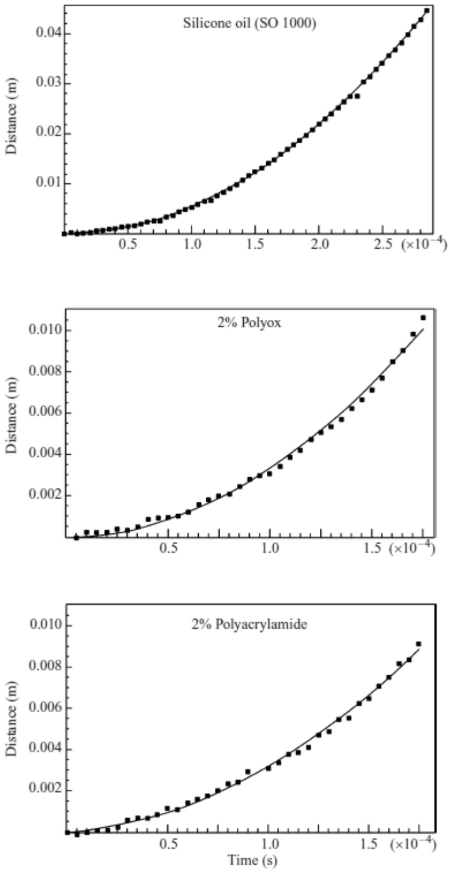

Fig. 21.5. Distance traveled vs. time. $x - x_0 = \alpha(t - t_0)^2$ where x_0 and t_0 are the extrapolated starting values from the curve fitting technique. The starting values x_0 and t_0 are uncertain within several pixels and several frames (5 μs per frame).

21.1.3.1 Stability analysis

The undisturbed interface between two fluids is located at $z = 0$, with a system of Cartesian coordinates $\boldsymbol{x} = (x, y, z) = (x_1, x_2, x_3)$ moving with acceleration $\boldsymbol{a}$:

$$\boldsymbol{a} = \boldsymbol{g} - \dot{\boldsymbol{V}} = \left(0,\ -g,\ -\dot{V}\right) = (0,\ -g,\ -a)\,. \tag{21.1.1}$$

For the conditions of the experiments described in this paper the drop moves in a horizontal plane and we may neglect g as at least four orders of magnitude smaller than $\dot{V}$. The undisturbed rest state is given by the pressure $\bar{p}^{(2)}$ in the heavy non-Newtonian fluid (the Oldroyd-B fluid) in $z > 0$ and $\bar{p}^{(1)}$ in the light Newtonian fluid in $z < 0$:

$$\bar{p}^{(2)} = p_0 - \rho_2 a z, \quad \bar{p}^{(1)} = p_0 - \rho_1 a z, \tag{21.1.2}$$

where p_0 is the pressure at the interface, ρ_2 denotes the density of the heavy fluid, and ρ_1 is the density of the light fluid. Small disturbances are superimposed upon the undisturbed state to give rise to the Rayleigh-Taylor instability, for which the equations in the heavy fluid (in $0 < z$) are given by

$$\rho_2 \frac{\partial \boldsymbol{u}^{(2)}}{\partial t} = -\nabla p^{(2)} + \nabla \cdot \tau^{(2)}, \tag{21.1.3a}$$

$$\nabla \cdot \boldsymbol{u}^{(2)} = 0, \tag{21.1.3b}$$

$$\tau_{ij}^{(2)} + \lambda_1 \frac{\partial \tau_{ij}^{(2)}}{\partial t} = 2\mu_2 \left(e_{ij}^{(2)} + \lambda_2 \frac{\partial e_{ij}^{(2)}}{\partial t} \right), \tag{21.1.3c}$$

$$e_{ij}^{(2)} = \frac{1}{2} \left(\frac{\partial u_i^{(2)}}{\partial x_j} + \frac{\partial u_j^{(2)}}{\partial x_i} \right), \tag{21.1.3d}$$

where $\boldsymbol{u}^{(2)} = \left(u^{(2)}, v^{(2)}, w^{(2)}\right) = \left(u_1^{(2)}, u_2^{(2)}, u_3^{(2)}\right)$ is the velocity disturbance, the viscous stress tensor $\tau_{ij}^{(2)}$ of the Oldroyd-B fluid is expressed as the constitutive equation (21.1.3c) with the strain tensor $e_{ij}^{(2)}$ and the viscosity μ_2; λ_1 is the relaxation time and λ_2 the retardation time; the conventional tensor notation is used here. Then, equations for disturbances in the light fluid (in $z < 0$) are given by

$$\rho_1 \frac{\partial \boldsymbol{u}^{(1)}}{\partial t} = -\nabla p^{(1)} + \nabla \cdot \tau^{(1)}, \tag{21.1.4a}$$

$$\nabla \cdot \boldsymbol{u}^{(1)} = 0, \tag{21.1.4b}$$

$$\tau_{ij}^{(1)} = 2\mu_1 e_{ij}^{(1)}, \tag{21.1.4c}$$

$$e_{ij}^{(1)} = \frac{1}{2} \left(\frac{\partial u_i^{(1)}}{\partial x_j} + \frac{\partial u_j^{(1)}}{\partial x_i} \right), \tag{21.1.4d}$$

where the viscous stress tensor $\tau_{ij}^{(1)}$ of the Newtonian fluid is expressed as (21.1.4c) with the strain tensor $e_{ij}^{(1)}$ and the viscosity μ_1.

Boundary conditions at the interface with its displacement h (at $z = h \approx 0$) are given by the continuity of velocity, the kinetic condition and the continuity of the stress:

$$\boldsymbol{u}^{(1)} = \boldsymbol{u}^{(2)}, \tag{21.1.5a}$$

$$\frac{\partial h}{\partial t} = w^{(1)} = w^{(2)}, \tag{21.1.5b}$$

$$\tau_{13}^{(1)} = \tau_{13}^{(2)}, \tag{21.1.5c}$$

$$\tau_{23}^{(1)} = \tau_{23}^{(2)}, \tag{21.1.5d}$$

$$-p^{(2)} + \tau_{33}^{(2)} + \rho_2 a h - \left(-p^{(1)} + \tau_{33}^{(1)} + \rho_1 a h\right) = -\gamma \Delta h, \tag{21.1.5e}$$

where γ is the surface tension and Δ is the horizontal Laplacian:

$$\Delta = \frac{\partial^2}{\partial x^2} + \frac{\partial^2}{\partial y^2}. \tag{21.1.6}$$

Further, the boundary conditions require that the disturbances vanish, respectively, as $z \to \pm\infty$.

The solution to the system of the disturbances may take the following form:

$$\left[\boldsymbol{u}^{(2)}, p^{(2)}, h, \boldsymbol{u}^{(1)}, p^{(1)}\right] = \left[\hat{\boldsymbol{u}}^{(2)}(z), \hat{p}^{(2)}(z), \hat{h}, \hat{\boldsymbol{u}}^{(1)}(z), \hat{p}^{(1)}(z)\right] \exp\left(nt + \imath k_x x + \imath k_y y\right) + c.c., \tag{21.1.7}$$

where n denotes the complex growth rate, $(k_x, k_y, 0)$ is the wavenumber vector of magnitude $k = \sqrt{k_x^2 + k_y^2}$, and *c.c.* stands for the complex conjugate of the preceding expression. Using (21.1.7), the constitutive equation (21.1.3c) is now written as

$$\tau_{ij}^{(2)} = 2\hat{\alpha} e_{ij}^{(2)}, \tag{21.1.8a}$$

with $\hat{\alpha}$ defined by

$$\hat{\alpha} = \mu_2 \frac{1+\lambda_2 n}{1+\lambda_1 n}. \tag{21.1.8b}$$

Taking this into account and taking rotation of (21.1.3a) and (21.1.4a) with using $\nabla \times \nabla \times \boldsymbol{u} = -\nabla^2 \boldsymbol{u}$ for incompressible fluid, we get the following equations:

$$\left(\nabla^2 - \frac{n\rho_1}{\mu_1}\right)\nabla^2 w^{(1)} = 0 \quad \text{in } z<0, \quad \left(\nabla^2 - \frac{n\rho_2}{\hat{\alpha}}\right)\nabla^2 w^{(2)} = 0 \quad \text{in } z>0, \tag{21.1.9}$$

for which the boundary conditions at the disturbed interface are written in terms of $w^{(1)}$ and $w^{(2)}$ as

$$\frac{\partial w^{(1)}}{\partial z} = \frac{\partial w^{(2)}}{\partial z}, \tag{21.1.10a}$$

$$\frac{\partial h}{\partial t} = w^{(1)} = w^{(2)}, \tag{21.1.10b}$$

$$\mu_1 \left(\Delta - \frac{\partial^2}{\partial z^2}\right) w^{(1)} = \hat{\alpha}\left(\Delta - \frac{\partial^2}{\partial z^2}\right) w^{(2)}, \tag{21.1.10c}$$

$$\begin{aligned} -\left(\rho_2 \frac{\partial^2 w^{(2)}}{\partial t \partial z} - \hat{\alpha}\nabla^2 \frac{\partial w^{(2)}}{\partial z}\right) + 2\hat{\alpha}\Delta \frac{\partial w^{(2)}}{\partial z} + \left(\rho_1 \frac{\partial^2 w^{(1)}}{\partial t \partial z} - \mu_1 \nabla^2 \frac{\partial w^{(1)}}{\partial z}\right) - 2\mu_1 \Delta \frac{\partial w^{(1)}}{\partial z} \\ + (\rho_2 - \rho_1)\, a\Delta h + \gamma \Delta^2 h = 0, \end{aligned} \tag{21.1.10d}$$

and the conditions away from the interface are

$$w^{(1)} \to 0 \quad \text{as } z \to -\infty, \quad w^{(2)} \to 0 \quad \text{as } z \to \infty. \tag{21.1.10e}$$

To satisfy (21.1.10e), the solutions to Eqs(21.1.9) are expressed as

$$w^{(1)} = A^{(1)} \exp(kz) + B^{(1)} \exp(q_1 z), \quad w^{(2)} = A^{(2)} \exp(-kz) + B^{(2)} \exp(-q_2 z), \tag{21.1.11}$$

with q_1 and q_2 defined by

$$q_1 = \sqrt{k^2 + \frac{n\rho_1}{\mu_1}}, \quad q_2 = \sqrt{k^2 + \frac{n\rho_2}{\hat{\alpha}}}. \tag{21.1.12}$$

After substituting (21.1.11) into the boundary conditions (21.1.10a)-(21.1.10d), we obtain an inhomogeneous system of linear equations for $A^{(1)}$, $B^{(1)}$, $A^{(2)}$ and $B^{(2)}$ which is solvable if and only if the determinant of the coefficient matrix vanishes. After a straightforward but tedious analysis we have the dispersion relation:

$$\begin{aligned} -\left[1 + \frac{1}{n^2}\left((\alpha_1 - \alpha_2)\, ak + \frac{\gamma k^3}{\rho_1 + \rho_2}\right)\right](\alpha_2 q_1 + \alpha_1 q_2 - k) - 4k\alpha_1\alpha_2 \\ +4\frac{k^2}{n}\frac{\mu_1 - \hat{\alpha}}{\rho_1 + \rho_2}\left[\alpha_2 q_1 - \alpha_1 q_2 + (\alpha_1 - \alpha_2)\, k\right] + 4\frac{k^3}{n^2}\left(\frac{\mu_1 - \hat{\alpha}}{\rho_1 + \rho_2}\right)^2 (q_1 - k)(q_2 - k) = 0, \end{aligned} \tag{21.1.13}$$

where

$$\alpha_1 = \frac{\rho_1}{\rho_1 + \rho_2}, \quad \alpha_2 = \frac{\rho_2}{\rho_1 + \rho_2}. \tag{21.1.14}$$

Then the experiment shows $\rho_2 \gg \rho_1$, for which $\alpha_2 \to 1$ and $\alpha_1 \to 0$. Moreover $\mu_1 \ll \hat{\alpha}$ in the experiment, so that (21.1.13) reduces to

$$-\left[1 + \frac{1}{n^2}\left(-ak + \frac{\gamma k^3}{\rho_2}\right)\right] - 4\frac{k^2}{n}\frac{\hat{\alpha}}{\rho_2} + 4\frac{k^3}{n^2}\left(\frac{\hat{\alpha}}{\rho_2}\right)^2 (q_2 - k) = 0. \tag{21.1.15}$$

Equation (21.1.15) approximates (21.1.13) with only a small error; it is appropriate for Rayleigh-Taylor instability in a vacuum.

The solution of (21.1.13) gives rise to a dispersion relation of the type shown in figure 9.2. The border of stability is given by a critical wavenumber with stability only when

$$k > k_c = \sqrt{\frac{\rho \dot{V}}{\gamma}} \tag{21.1.16}$$

independent of viscosity, relaxation or retardation time. Dispersion relations for our experiments are presented in figures 21.6-21.8 of §21.1.3.3.

21.1.3.2 Viscoelastic potential flow analysis of stability

Rayleigh-Taylor instability at an air-liquid or vacuum-liquid surface is one of the many cases in which accurate results may be obtained using potential flow. For viscous potential flow the viscosity enters only in the normal component of the viscous stress. The dispersion relations for viscous flow and viscous potential flow derived in JBB (see Chapter 17), though different, give values for the wavenumber and the growth rate of the most dangerous wave that are in good agreement. Viscous potential theory yields values for the wavenumber that are about 2% higher, and values for the growth rate that are about 8.8% higher, than the corresponding values from fully viscous theory (JBB, table 3). This shows that the main physical effect of viscosity is on the normal stress balance.

The results given in JBB carry over to viscoelastic potential flows as we now show. We now require for each fluid that the potential ϕ gives the velocity disturbance ($\boldsymbol{u} = \nabla\phi$) and satisfies the Laplace equation

$$\nabla^2 \phi = 0, \tag{21.1.17}$$

and the pressure disturbance is given by Bernoulli's equation

$$\rho \frac{\partial \phi}{\partial t} + p + \rho a z = -\frac{\rho}{2} \left| \nabla \phi \right|^2 \approx 0, \tag{21.1.18}$$

for the same undisturbed state that was given in §21.1.3.3. Then the boundary conditions are given by (21.1.5a) and (21.1.5c) at the disturbed interface and (21.1.10e) away from the interface. The normal stress balance (21.1.10d) is now written, using (21.1.18), as

$$\rho_2 \frac{\partial \phi^{(2)}}{\partial t} + \tau_{33}^{(2)} + \rho_2 a h - \left(\rho_1 \frac{\partial \phi^{(1)}}{\partial t} + \tau_{33}^{(1)} + \rho_1 a h \right) = -\gamma \Delta h, \tag{21.1.19}$$

where

$$\frac{\tau_{33}}{2\mu} = e_{33} = \frac{\partial w}{\partial z} = \frac{\partial^2 \phi}{\partial z^2} = k^2 \phi. \tag{21.1.20}$$

Thus the solutions to (21.1.17) that vanish respectively as $z \to \pm\infty$ may be expressed as

$$w^{(1)} = A^{(1)} \exp(kz) \quad \text{in } z < 0, \quad w^{(2)} = A^{(2)} \exp(-kz) \quad \text{in } z > 0. \tag{21.1.21}$$

Substitution of these into the boundary conditions using (21.1.10b) leads to the dispersion relation:

$$1 = \frac{\alpha_2 - \alpha_1}{n^2} k a - \frac{k^3 \gamma}{n^2 (\rho_2 + \rho_1)} - \frac{2k^2}{n} \frac{\hat{\alpha} + \mu_1}{\rho_2 + \rho_1}. \tag{21.1.22}$$

Without much loss of generality, we may put $\alpha_1 = 0$, $\alpha_2 = 1$ and $\hat{\alpha} \gg \mu_1$, so that the dispersion relation becomes

$$1 = \frac{ka}{n^2} - \frac{k^3 \gamma}{n^2 \rho_2} - \frac{2k^2}{n} \frac{\hat{\alpha}}{\rho_2}, \tag{21.1.23}$$

which can then be written as a cubic equation for the growth rate n.

It is interesting to note here that (21.1.23) for viscoelastic potential flow gives the same growth rate as the dispersion relation (21.1.15) for fully viscous flow if q_2 in (21.1.15) is approximated as

$$q_2 - k = \sqrt{k^2 + \frac{n \rho_2}{\hat{\alpha}}} - k \approx \frac{n \rho_2}{2k\hat{\alpha}}, \tag{21.1.24}$$

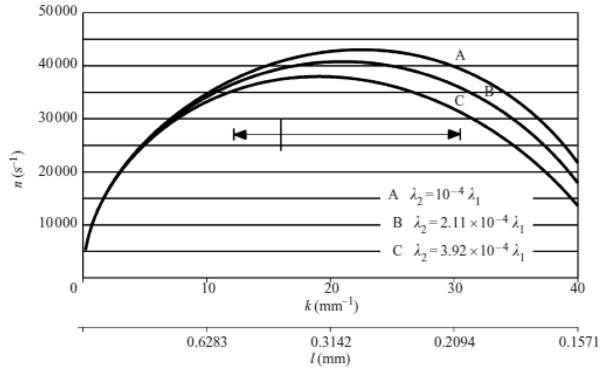

Fig. 21.6. The growth rate n versus the wavenumber k from (21.1.15) for 2% PO ($M_s = 2$); $\lambda_1 = 0.21$ s. The average wavelength and scatter from a very early time in the experiment are indicated.

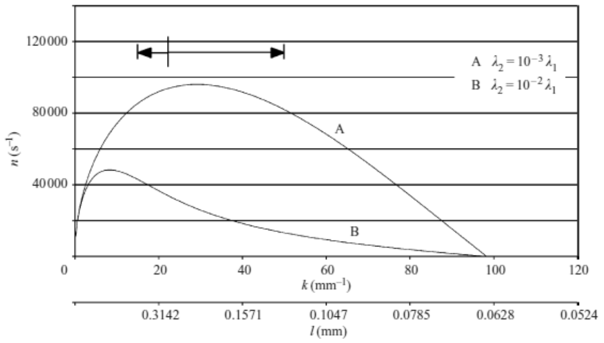

Fig. 21.7. The growth rate n versus the wavenumber k from (21.1.15) for 2% PO ($M_s = 3$); $\lambda_1 = 0.21$ s. The average wavelength and scatter from a very early time in the experiment are indicated.

i.e., under the condition that

$$\frac{n\rho_2}{2k\hat{\alpha}} \ll 1. \tag{21.1.25}$$

Thus, under this condition, the theory of viscoelastic potential flow may provide a good approximation of fully viscous theory.

21.1.3.3 Comparison of the exact and potential flow analysis

Based on the data for the experimental conditions cited in Tables 21.1 and 21.2, the dispersion relation (21.1.15) is used to calculate the stability conditions, and the results are depicted in figure 21.6: 2% PO ($M_s = 2$); figure 21.7: 2% PO ($M_s = 3$); and figure 21.8: 2% PAA ($M_s = 3$). In each of the figures several plots of the dispersion relation (21.1.15) are shown for a fxed (known) value of the relaxation time and various assumed values of the retardation time λ_2. The growth rates are computed at increments in the wavenumber of 200 m^{-1} from $k = 0$ to the critical value. The dispersion relation (21.1.23) from viscoelastic potential theory gives rise to graphs that are nearly identical to those in figures 21.6-21.8.

For comparison of (21.1.23) and (21.1.15), values of the wavenumber k, wavelength l and growth rate n of the most dangerous wave are shown in table 21.3, 2% PO ($M_s = 2$); table 21.4, 2% PO ($M_s = 3$); and table 21.5, 2% PAA ($M_s = 3$). These results show that the set of values of the growth rate and the wavenumber given by the viscoelastic potential analysis and the corresponding set of values obtained from the exact stability analysis are at the same level of good agreement as in the Newtonian case. The wavenumber predicted from viscoelastic potential analysis is greater than the corresponding value from fully viscoelastic theory by between 0 and 5.4% (with two exceptions): the growth rates from viscoelastic potential analysis are between 8.5% and 9.0% higher than predicted by fully viscoelastic theory, except at the smallest values of λ_2.

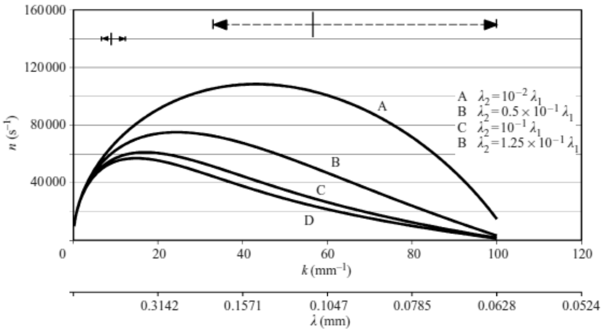

Fig. 21.8. The growth rate n vs. the wavenumber k from (21.1.15) for 2% PAA ($M_s = 3$); $\lambda_1 = 0.034$ s. The average wavelength and scatter from a very early time in the experiment are indicated. Also shown by dotted lines are the average wavelength and scatter for the set of waves of small wavelength which appear to be superimposed on the long wavelength waves.

	Exact			Viscoelastic potential			Percent difference	
λ_2/ (s^{-1})	k (m^{-1})	l (mm)	n (s^{-1})	k (m^{-1})	l (mm)	n (s^{-1})	k	n
$\lambda_1/5$	600	10.472	6331.7	800	7.8539	6870.9	33.3	8.5
$\lambda_1/8$	1000	6.2832	7425.1	1000	6.2832	8077.7	0	8.8
$\lambda_1/10$	1000	6.2832	7991.5	1200	5.2359	8684.8	20.0	8.2
$\lambda_1/20$	1800	3.4907	10061.5	1800	3.4907	10945.9	0	8.8
$\lambda_1/100$	4800	1.3090	17000.0	5000	1.2566	18489.8	4.2	8.8
$\lambda_1/1000$	15 000	0.4189	32238.7	15 800	0.3977	34849.6	5.3	8.1
$\lambda_1/10000$	22 400	0.2805	43036.2	23 600	0.2662	45074.9	5.4	4.7
0	24 200	0.2596	45697.3	25 000	0.2513	47119.7	3.3	3.1

Table 21.3. *2% PO ($M_s = 2$). Values of the wavenumber k, wavelength l and growth rate n of the most dangerous wave for the experimental conditions given in tables 21.1 and 21.2; the retardation time λ_2 is changed against the relaxation time λ_1. The values of k and n predicted by viscoelastic potential theory are higher than the corresponding fully viscoelastic predictions. The differences are indicated as a percentage of the fully viscoelastic values.*

	Exact			Viscoelastic potential			Percent difference	
λ_2 (s^{-1})	k (m^{-1})	l (mm)	n (s^{-1})	k (m^{-1})	l (mm)	n (s^{-1})	k	n
$\lambda_1/5$	1200	5.2359	17925.3	1200	5.2359	19496.0	0	8.8
$\lambda_1/8$	1600	3.9269	20968.4	1600	3.9269	22801.0	0	8.7
$\lambda_1/10$	1800	3.4907	22584.4	1800	3.4907	24549.0	0	8.7
$\lambda_1/20$	3000	2.0944	28424.1	3000	2.0944	30915.1	0	8.8
$\lambda_1/100$	8200	0.7662	48320.5	8400	0.7480	52541.6	2.4	8.7
$\lambda_1/1000$	29 200	0.2152	96037.0	30 600	0.2053	103 960	4.8	8.2
$\lambda_1/10000$	49 400	0.1272	138 925	51 600	0.1218	145 138	4.5	4.4
0	55 600	0.1130	152 570	56 600	0.1110	155 111	1.8	1.7

Table 21.4. *As table 21.3 but for 2% PO ($M_s = 3$).*

	Exact			Viscoelastic potential			Percent difference	
λ_2/ (s^{-1})	k (m^{-1})	l (mm)	n (s^{-1})	k (m^{-1})	l (mm)	n (s^{-1})	k	n
$\lambda_1/5$	11 200	0.5610	49081.4	11 400	0.5512	53350.0	1.8	8.7
$\lambda_1/8$	14 800	0.4245	57009.4	15 200	0.4134	61948.0	2.7	8.7
$\lambda_1/10$	17 000	0.3696	61112.1	17 400	0.3611	66389.7	2.4	8.6
$\lambda_1/20$	24 400	0.2575	75051.4	25 400	0.2474	81393.6	4.1	8.5
$\lambda_1/100$	43 200	0.1454	108 441	45 400	0.1384	115 536	5.1	6.5
$\lambda_1/1000$	56 400	0.1114	133 671	57 800	0.1087	136 333	2.5	2.0
$\lambda_1/10000$	59 000	0.1065	138 403	59 400	0.1058	139 290	0.7	0.6
0	59 400	0.1058	139 007	59 800	0.1051	139 633	0.7	0.5

Table 21.5. *As table 21.3 but for 2% PAA ($M_s = 3$).*

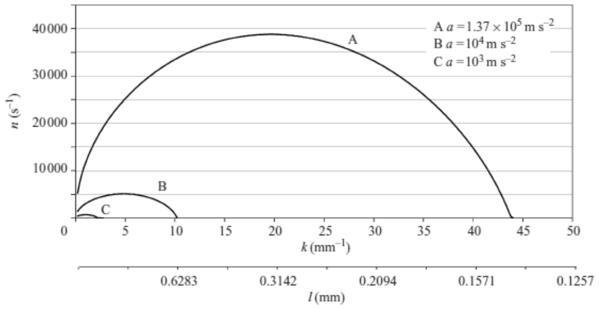

Fig. 21.9. The effect of acceleration on the dispersion relation for 2% PO; $\lambda_1 = 0.21$ s, $\lambda_2 = 3.3 \times 10^{-4}\lambda_1$.

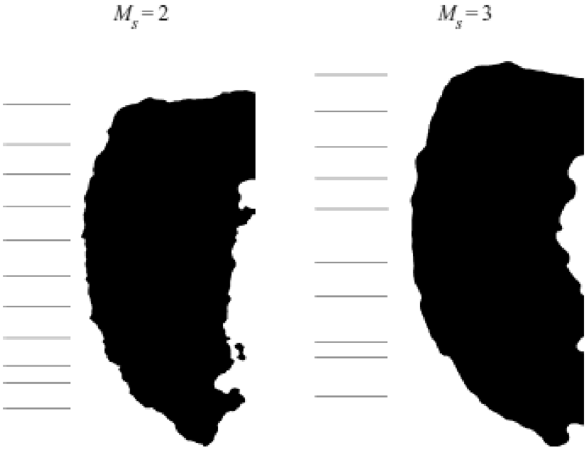

Fig. 21.10. Rayleigh-Taylor waves in 2% PO.

21.1.4 Comparison of theory and experiment

We now compare the Rayleigh-Taylor stability theory with experiments on drop breakup for the three viscoelastic cases discussed in §21.1.2. For comparison, we repeat results from JBB for a 1.0 kg m^{-1} s^{-1} silicone oil whose viscosity nearly matches the 0.96 kg m^{-1} s^{-1} polyacrylamide. Figure 21.12 21.12, taken from JBB, shows the waves on drops of this Newtonian liquid at very early times in the motion at shock Mach numbers of 2 and 3.

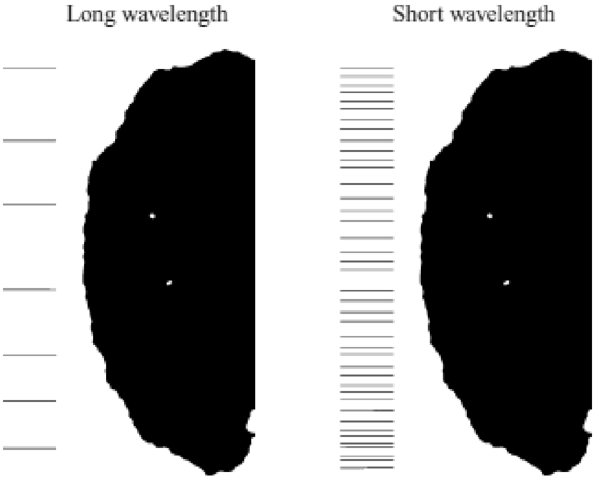

Fig. 21.11. Rayleigh-Taylor waves in 2% PAA.

The waves on both the polyox and polyacrylamide drops were smaller and more difficult to identify than the waves on the Newtonian liquids shown, for example, in Engel [1958, Fig. 9], Hwang *et al* [1996, Fig. 8], and in JBB. For example, the measured average wavelengths for the 1.0 kg m^{-1} s^{-1} silicone oil are about 2.0 mm and 1.25 mm for shock Mach numbers of 2 and 3 respectively, while the corresponding values for the 2% polyox solution are 0.39 mm and 0.20 mm. In an attempt to identify the waves more clearly on the computer screen Adobe Photoshop$^{\mathrm{TM}}$ was used to exaggerate the contrast. We then measured the lengths of the waves by first locating the troughs across the front of the drop on the computer screen, and then measuring the distance between troughs in pixels which were finally converted to millimeters using a predetermined scaling factor for each frame. The enhanced contrast images are shown in Figure 21.10 for the 2% aqueous polyox and Figure 21.11 for the 2% polyacrylamide. The tick marks identify the wave troughs. Like the Newtonian liquids in JBB, the troughs are easier to identify on the computer screen than in the printed figure. The length of the waves increases with time because the waves are ultimately forced apart by high pressures in the wave troughs; from this it follows that the length of unstable waves should be measured at the earliest times for which all the waves can be identified.

The early appearance and short life of distinctly identifiable Rayleigh-Taylor waves is illustrated in Figure 9.9 (a), which shows contrast-enhanced images from a repeat movie of the breakup of a drop (2.9 mm diameter) of 2.0% aqueous solution of polyox at a shock Mach number of 2.9 made several months after the earlier work. The four images in Figure 9.9 (a) show the drop at 5 μs intervals starting at 30 μs after the passage of the shock wave. As before, the images are clearer and the waves are much easier to identify on the computer screen than in the printed version where they appear pixelated. The waves have wavelengths of 5 pixels, which translates to 0.2 mm on the scaling used for this movie, in frames (i), (ii), and (iii) but in (iv) the waves are becoming less distinct and only a few 5-pixel wavelengths could be found. For times greater than that of frame (iv) the front face of the drop becomes very irregular as the drop sheds liquid and begins to break up.

The time interval in which the waves can be identified appears to correspond to the interval in which the original almost-spherical drop is undergoing severe deformation as the front and back faces are being flattened and the cross-sectional area to the flow is increasing. This deformation is shown in Figure 9.9 (b) which presents the movie images corresponding to the contrast-enhanced images of Figure 9.9 (a). When the drop of polyox is injected into the test section of the shock tube it leaves a thin, trailing thread of liquid connecting it to the injection needle. The disintegration of the thread is visible in the frames of Figure 9.9 (b). The dark area that moves downstream from the top of the drop is the liquid that formed the small web at the top of the drop where the thread was attached. Figure 9.9 (b) also indicates that liquid starts to be torn from the equator of the drop about 30 μs after exposure to the high-speed flow.

Returning to Figure 21.11, there is some uncertainty in the measurements of the wavelengths from the 2% PAA picture because there appeared to be two sets of waves, a distinct set with an average wavelength of 0.70 mm with a second set of smaller waves superimposed on the larger waves. The wavelengths of the smaller waves were very irregular, with values between approximately 0.05 mm and 0.24 mm. Smaller, but less distinct, waves could also be identified over parts of the front face of the polyox drops.

On Figures 21.6-21.8 we graph dispersion relations corresponding to measured data given in tables 21.1 and 21.2. The retardation time λ_2 is a fitting parameter. The dispersion graphs are sensitive to values of λ_2 as is shown in Figures 21.6-21.8, where for each figure values for λ_2 have been chosen to yield curves such that the wavelengths of maximum growth are close to the interval of instability defined from the experiments, which is also included on the figures. From these we may estimate a λ_2 which centers the wavelength of maximum growth in the interval of instability. The estimated values of λ_2 needed to achieve agreement are uniformly small, ranging from $\lambda_2 \approx \lambda_1/5000$ for 2% aqueous polyox at $M_s = 2$, to $\lambda_2 \approx \lambda_1/100$ for 2% aqueous PAA at $M_s = 3$. Boltzman has described the viscosity of a fluid as an effect of relaxed elastic modes and it is given as the area under the shear relaxation modulus. Joseph [1990, chapter 18] interpreted the retardation time as representing the effect of the most rapidly relaxing modes; it depends on the time of observation as well as the material. The small value of the retardation time which matches theory and experiment reported here is as might be expected in such an explosive and short-time (10-50 μs) event as produces Rayleigh-Taylor waves on drops suddenly exposed to a high speed airstream.

Liquid	Shock Mach number	Approx. n (s^{-1})	Time for $A = 10A_0$ (μs)	Experimental blow-off time (μs)
SO 1000	3	48 769	47	40
2% PO	3	90 000	25	30
2% PO	2	38 000	60	50
2% PAA: Short	3	110 000	20	35
Long		75 000	30	

Table 21.6. *Comparison of measured breakup times (defined as the time at which liquid first starts to 'blow-off' the perimeter of the drop) with predicted times* $\hat{t}_b$ *calculated from equation* $\hat{t}_b = \ln M/n$ *with* $M = 10$ *and using values of n from the fully viscoelastic analysis.*

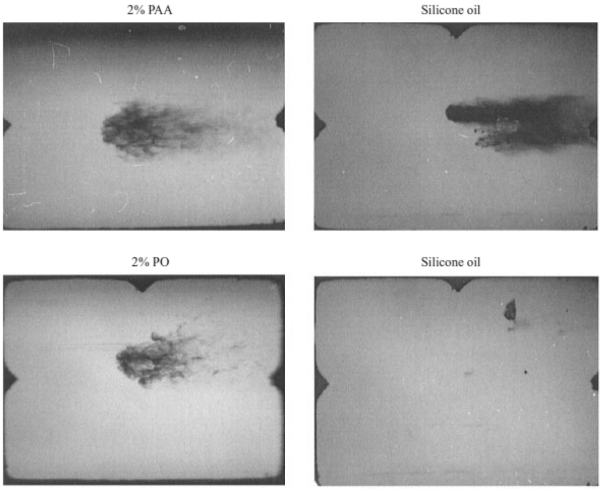

Fig. 21.12. Droplet configurations for 2% PAA, 2% PO, and two different silicone oils 170 μs after passing of the shock over the drop under the same conditions ($M_s = 3$). The top pair of photographs compares PAA with a silicone oil of approximately the same viscosity (1 kg m^{-1} s^{-1}). The bottom pair compares 2% PO (viscosity = 35 kg m^{-1} s^{-1}) with a silicone oil that has a viscosity of about one-third that of the PO (10 kg m^{-1} s^{-1}).

In the previous paragraph we have argued that λ_2 is not fixed but depends at least on some conditions of external excitation and that Rayleigh-Taylor disturbances are so fast that the response of the drops is highly elastic (small values of λ_2).

21.2 Purely irrotational theories of the effects of viscosity and viscoelasticity on capillary instability of a liquid cylinder

Capillary instability of a liquid cylinder can arise when either the interior or exterior fluid is a gas of negligible density and viscosity. The shear stress must vanish at the gas-liquid interface but it does not vanish in irrotational flows. Joseph and Wang (2004) derived an additional viscous correction to the irrotational pressure. They argued that this pressure arises in a boundary layer induced by the unphysical discontinuity of the shear stress. Wang, Joseph and Funada (2005) showed that the dispersion relation for capillary instability in the Newtonian case is almost indistinguishable from the exact solution when the additional pressure contribution is included in the irrotational theory. Here we extend the formulation for the additional pressure to potential flows of viscoelastic fluids in flows governed by linearized equations, and apply this additional pressure to capillary instability of viscoelastic liquid filaments of Jeffreys type. The shear stress at the gas-liquid interface cannot be made to vanish in an irrotational theory, but the explicit effect of this uncompensated shear stress can be removed from the global equation for the evolution of the energy of disturbances. This line of thought allows us to present the additional pressure theory without appeal to boundary layers. The validity of this purely irrotational theory can be judged by comparison with the exact solutions of Navier-Stokes equations. Here we show that our purely irrotational theory is in remarkably good agreement with the exact solution in linear analysis of the capillary instability of a viscoelastic liquid cylinder.

21.2.1 Introduction

Capillary instability of a liquid cylinder of mean radius R leading to capillary collapse can be described as a neckdown due to surface tension γ in which fluid is ejected from the throat of the neck, leading to a smaller neck and greater neckdown capillary force as seen in the diagram in Fig. 21.13.

Capillary instability of Newtonian fluids was studied by Rayleigh (1879) following earlier work by Plateau (1873) who showed that a long cylinder of liquid is unstable to disturbances with wave lengths greater than $2\pi R$. The analysis of Rayleigh is based on potential flow of an inviscid liquid. Tomotika (1935) studied the capillary instability and gave an exact normal mode solution of the linearized Navier-Stokes equations.

The linear analysis of capillary instability of viscoelastic fluids has been done by Middleman (1965), Goldin *et al.* (1969), Goren and Gottlieb (1982). They showed that the growth rates are larger for the viscoelastic fluids than for the equivalent Newtonian fluids.

Funada and Joseph (2002, 2003) presented potential flow analyses of capillary instability of viscous and viscoelastic fluids. In their studies, the flow is assumed to be irrotational but the viscous and viscoelastic effects are retained (viscous or viscoelastic potential flow, VPF). The viscous and viscoelastic stresses enter into the analyses through the normal stress balance at the interface. Funada and Joseph compared their results based on potential flow to the unapproximated normal mode results (Tomotika 1935). They showed that the results with viscous and viscoelastic effects retained are in better agreement with the unapproximated results than those assuming inviscid fluids.

The capillary instability can be viewed as a free surface problem when either the interior or the exterior fluid is a gas of negligible density and viscosity. One difficulty in the potential flow analyses of free surface problems is that the non-zero irrotational shear stress violates the zero-shear-stress condition at the free surface. Joseph and Wang (2004) derived an additional viscous correction for the irrotational pressure, which arises in the boundary layer induced by the unphysical discontinuity of the shear stress. Wang, Joseph and Funada (2005) applied this additional pressure contribution to the potential flow analysis of capillary instability of Newtonian fluids. They showed that the results computed with the additional pressure contribution are almost indistinguishable from the exact results. Here we extend the formulation for the additional pressure correction to potential flows of viscoelastic fluids in flows governed by linearized equations (viscoelastic correction of viscoelastic potential flow, VCVPF), and apply this additional pressure correction to capillary instability of viscoelastic liquid filaments of Jeffreys type. The results are in remarkably good agreement with those obtained from the unapproximated normal mode analysis for viscoelastic fluids.

The linear stability analysis given here and elsewhere indicates that the liquid jets are less stable with increasing elasticity, which contradicts the observation in experiments. A possible explanation of this contradiction is

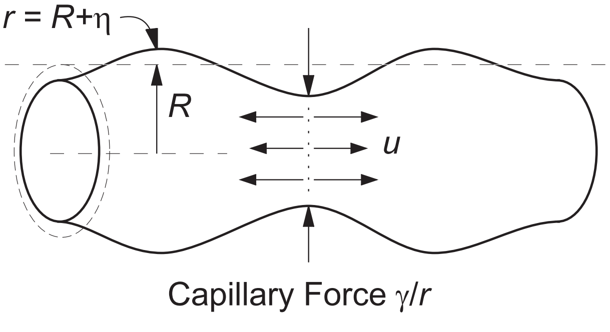

Fig. 21.13. Capillary instability. The force γ/r drives fluid away from the throat, leading to collapse.

related to the linear stability analysis of a stressed filament at rest (Entov 1978). One difficulty is that a stressed filament at rest is not a permanent solution.

21.2.2 Linear stability equations and the exact solution (Tomotika 1935)

In an undisturbed rest state, the long cylinder of a viscoelastic liquid is surrounded by a gas of negligible density and viscosity. We use cylindrical coordinates (r,θ,z) and consider small axisymmetric disturbances. The linearized governing equations of the interior liquid are

$$\nabla\cdot\boldsymbol{u}=0, \tag{21.2.1}$$

$$\rho\frac{\partial\boldsymbol{u}}{\partial t}=-\nabla p+\nabla\cdot\tau \tag{21.2.2}$$

where $\boldsymbol{u}=u\boldsymbol{e}_r+w\boldsymbol{e}_z$ is the velocity, ρ is the density, p is the pressure, and τ is the extra stress. The extra stress may be modeled by Jeffreys model

$$\tau+\lambda_1\frac{\partial\tau}{\partial t}=2\mu\left(\mathbf{D}+\lambda_2\frac{\partial\mathbf{D}}{\partial t}\right), \tag{21.2.3}$$

where $\mathbf{D}$ is the rate of strain tensor, μ is the viscosity, λ_1 and λ_2 are the relaxation and retardation times, respectively. Suppose that we have normal mode solutions with the growth rate σ:

$$\tau=\exp(\sigma t)\tilde{\tau}\ \text{ and }\ \mathbf{D}=\exp(\sigma t)\tilde{\mathbf{D}}, \tag{21.2.4}$$

then (21.2.3) leads to

$$\tilde{\tau}=\frac{1+\lambda_2\sigma}{1+\lambda_1\sigma}2\mu\tilde{\mathbf{D}}\quad\Rightarrow\quad\tau=\frac{1+\lambda_2\sigma}{1+\lambda_1\sigma}2\mu\mathbf{D}. \tag{21.2.5}$$

The momentum equation (21.2.2) becomes

$$\rho\frac{\partial\boldsymbol{u}}{\partial t}=-\nabla p+\nabla\cdot\left(\frac{1+\lambda_2\sigma}{1+\lambda_1\sigma}2\mu\mathbf{D}\right)=-\nabla p+\frac{1+\lambda_2\sigma}{1+\lambda_1\sigma}\mu\nabla^2\boldsymbol{u}. \tag{21.2.6}$$

The shear and normal stress boundary conditions are

$$\frac{1+\lambda_2\sigma}{1+\lambda_1\sigma}\mu\left(\frac{\partial u}{\partial z}+\frac{\partial w}{\partial r}\right)=0\ ; \tag{21.2.7}$$

$$-p+\frac{1+\lambda_2\sigma}{1+\lambda_1\sigma}2\mu\frac{\partial u}{\partial r}=\gamma\left(\frac{\partial^2\eta}{\partial z^2}+\frac{\eta}{R^2}\right), \tag{21.2.8}$$

where η is the varicose displacement. The governing equations (21.2.1) and (21.2.6) and boundary conditions (21.2.8) and (21.2.7) are the same as those for a Newtonian fluid except that $\dfrac{1+\lambda_2\sigma}{1+\lambda_1\sigma}\mu$ replaces μ.

Following scales are used to construct dimensionless governing equations: the cylinder diameter D for length, $U=\sqrt{\gamma/(\rho D)}$ for velocity, $T=D/U$ for time and $p_0=\rho U^2$ for pressure. The dimensionless momentum equation is (we use the same symbols for dimensionless variables)

$$\frac{\partial\boldsymbol{u}}{\partial t}=-\nabla p+\frac{\hat{\mu}}{\sqrt{J}}\nabla^2\boldsymbol{u}, \tag{21.2.9}$$

where

$$\hat{\mu}=\frac{1+\hat{\lambda}_2\sigma}{1+\hat{\lambda}_1\sigma} \tag{21.2.10}$$

with

$$\hat{\lambda}_1=\lambda_1\frac{U}{D}=\lambda_1\sqrt{\frac{\gamma}{\rho D^3}}\ \text{ and }\ \hat{\lambda}_2=\lambda_2\frac{U}{D}=\lambda_2\sqrt{\frac{\gamma}{\rho D^3}}, \tag{21.2.11}$$

and

$$J = \rho\gamma D/\mu^2 \tag{21.2.12}$$

is the Reynolds number and $J^{-1/2}$ is the Ohnesorge number. The dimensionless boundary conditions at the cylinder surface $R = 0.5$ are

$$-p + 2\frac{\hat{\mu}}{\sqrt{J}}\frac{\partial u}{\partial r} = \frac{\partial^2 \eta}{\partial z^2} + \frac{\eta}{R^2}; \tag{21.2.13}$$

$$\frac{\hat{\mu}}{\sqrt{J}}\left(\frac{\partial u}{\partial z} + \frac{\partial w}{\partial r}\right) = 0. \tag{21.2.14}$$

A solution of (21.2.9) which satisfies both the boundary conditions (21.2.13) and (21.2.14) takes the following form:

$$\psi = [A_1 r I_1(kr) + A_2 r I_1(k_v r)]\exp(\sigma t + \mathrm{i}kz), \quad u = \frac{1}{r}\frac{\partial \psi}{\partial z}, \quad w = -\frac{1}{r}\frac{\partial \psi}{\partial r}, \tag{21.2.15}$$

$$\eta = H\exp(\sigma t + \mathrm{i}kz), \tag{21.2.16}$$

where k is the wavenumber and I_1 denotes the first kind modified Bessel function of the first order. Substitution of (21.2.15) and (21.2.16) into (21.2.13) and (21.2.14) leads to the solvability condition, which is given as the dispersion relation of σ:

$$\begin{vmatrix} 2k^2 I_1(kR) & \left(k^2 + k_v^2\right) I_1(k_v R) \\ F_1 & F_2 \end{vmatrix} = 0 \tag{21.2.17}$$

where

$$F_1 = \sigma I_0(kR) + 2\frac{\hat{\mu}k^2}{\sqrt{J}}\left(\frac{\mathrm{d}I_1(kR)}{\mathrm{d}(kR)}\right) - \left(\frac{1}{R^2} - k^2\right)\frac{k}{\sigma}I_1(kR), \tag{21.2.18}$$

$$F_2 = 2\frac{\hat{\mu}kk_v}{\sqrt{J}}\left(\frac{\mathrm{d}I_1(k_v R)}{\mathrm{d}(k_v R)}\right) - \left(\frac{1}{R^2} - k^2\right)\frac{k}{\sigma}I_1(k_v R), \tag{21.2.19}$$

with $k_v = \sqrt{k^2 + \frac{\sqrt{J}}{\hat{\mu}}\sigma}$. This solution satisfies the governing equations and all the boundary conditions and is an exact solution†.

21.2.3 Viscoelastic potential flow (VPF)

It is easy to show that the momentum equation (21.2.9) admits potential flow solutions. Take curl of equation (21.2.9) and use $\boldsymbol{u} = \nabla\phi$, we obtain

$$\nabla \wedge \frac{\partial \nabla\phi}{\partial t} = \nabla \wedge (-\nabla p) + \frac{\hat{\mu}}{\sqrt{J}}\nabla \wedge \nabla^2\nabla\phi. \tag{21.2.20}$$

Both sides of (21.2.20) are zero, therefore potential flow solutions are compatible in this problem. The pressure integral can also be easily obtained from (21.2.9),

$$\nabla\left(\frac{\partial \phi}{\partial t}\right) = -\nabla p_p + \frac{\hat{\mu}}{\sqrt{J}}\nabla\nabla^2\phi \quad \Rightarrow \quad p_p = -\frac{\partial \phi}{\partial t}, \tag{21.2.21}$$

where p_p denotes the pressure from the potential flow solution and it is equal to the pressure from the inviscid potential flow.

The potential flow solution is given by

$$\phi = A\mathrm{i}I_0(kr)\exp(\sigma t + \mathrm{i}kz), \quad u = \frac{\partial \phi}{\partial r}, \qquad w = \frac{\partial \phi}{\partial z}, \tag{21.2.22}$$

---

† In our former paper (Wang, Joseph & Funada 2005), the exact solution of the linearized equations was called the fully viscous flow (FVF) solution.

$$\eta = H \exp(\sigma t + \mathrm{i}kz). \tag{21.2.23}$$

Substitution of the potential flow solution into the normal stress balance (21.2.13) leads to the dispersion relation

$$\frac{I_0(kR)}{I_1(kR)}\sigma^2\left(1+\hat{\lambda}_1\sigma\right)+\left(1+\hat{\lambda}_2\sigma\right)\sigma\frac{2k^2}{\sqrt{J}}\left[\frac{I_0(kR)}{I_1(kR)}-\frac{1}{kR}\right]-k\left(\frac{1}{R^2}-k^2\right)\left(1+\hat{\lambda}_1\sigma\right)=0, \tag{21.2.24}$$

which is a cubic equation of σ and has explicit solutions.

When $J \to \infty$, equation (21.2.24) reduces to

$$\frac{I_0(kR)}{I_1(kR)}\sigma^2 = k\left(\frac{1}{R^2}-k^2\right), \tag{21.2.25}$$

which is the dispersion relation for inviscid potential flow (IPF) solution. The IPF solution does not allow viscous or viscoelastic effects.

21.2.4 Dissipation and the formulation for the additional pressure contribution

Joseph and Wang (2004) derived a viscous pressure contribution in addition to the irrotational pressure for the potential flow solutions of Newtonian fluids by considering the dissipation of energy. Here we extend the analysis to a viscoelastic fluid of Jeffereys type in flows governed by linearized equations. We start from the momentum equation

$$\rho\frac{\mathrm{d}\boldsymbol{u}}{\mathrm{d}t} = \nabla\cdot\mathbf{T} \Rightarrow \quad \boldsymbol{u}\cdot\rho\frac{\mathrm{d}\boldsymbol{u}}{\mathrm{d}t} = (\nabla\cdot\mathbf{T})\cdot\boldsymbol{u}, \tag{21.2.26}$$

where $\mathbf{T}$ is the total stress. It follows that

$$\begin{aligned}\rho\frac{\mathrm{d}}{\mathrm{d}t}\left(\frac{1}{2}\boldsymbol{u}\cdot\boldsymbol{u}\right) &= \nabla\cdot(\mathbf{T}\cdot\boldsymbol{u}) - \nabla\boldsymbol{u}:\mathbf{T}\\ &= \nabla\cdot(\mathbf{T}\cdot\boldsymbol{u}) - (\mathbf{D}+\boldsymbol{\Omega}):(-p\mathbf{1}+2\hat{\mu}\mu\mathbf{D})\\ &= \nabla\cdot(\mathbf{T}\cdot\boldsymbol{u}) - \mathbf{D}:(-p\mathbf{1}+2\hat{\mu}\mu\mathbf{D})\\ &= \nabla\cdot(\mathbf{T}\cdot\boldsymbol{u}) - 2\hat{\mu}\mu\mathbf{D}:\mathbf{D}.\end{aligned}$$

It follows that

$$\frac{\mathrm{d}}{\mathrm{d}t}\int_V\left(\frac{\rho}{2}\boldsymbol{u}\cdot\boldsymbol{u}\right)\mathrm{d}V = \int_\Omega \boldsymbol{n}\cdot(\mathbf{T}\cdot\boldsymbol{u})\;\mathrm{d}\Omega - 2\hat{\mu}\mu\int_V \mathbf{D}:\mathbf{D}\mathrm{d}V, \tag{21.2.27}$$

where V is the volume occupied by the viscoelastic fluid, Ω is the boundary of V, and $\boldsymbol{n}$ is the outward normal of V on Ω. We have shown that the potential flow is a solution of the momentum equation in this problem. Thus we can insert the velocity and stress tensor evaluated on the potential flow into (21.2.27) to obtain

$$\frac{\mathrm{d}}{\mathrm{d}t}\int_V\left(\frac{\rho}{2}\boldsymbol{u}\cdot\boldsymbol{u}\right)\mathrm{d}V = \int_\Omega\left[(-p_p+\tau_{rr})u+\tau_{rz}w\right]\;\mathrm{d}\Omega - 2\hat{\mu}\mu\int_V \mathbf{D}:\mathbf{D}\;\mathrm{d}V. \tag{21.2.28}$$

At the free surface, the potential flow leads to a non-zero irrotational shear stress and does not satisfy the zero-shear-stress condition. We introduce a pressure contribution p_c in addition to the irrotational pressure p_p; p_c cancels out the power due to the unphysical irrotational shear stress in the energy equation and (21.2.27) becomes

$$\frac{\mathrm{d}}{\mathrm{d}t}\int_V\left(\frac{\rho}{2}\boldsymbol{u}\cdot\boldsymbol{u}\right)\mathrm{d}V = \int_\Omega\left[(-p_p-p_c+\tau_{rr})u\right]\;\mathrm{d}\Omega - 2\hat{\mu}\mu\int_V \mathbf{D}:\mathbf{D}\;\mathrm{d}V. \tag{21.2.29}$$

Comparing (21.2.28) and (21.2.29), we obtain

$$\int_\Omega \tau_{rz}w\;\mathrm{d}\Omega = \int_\Omega(-p_c)u\;\mathrm{d}\Omega, \tag{21.2.30}$$

which is the same as the formulation for the additional pressure contribution as in the potential flow of a viscous Newtonian fluid (Joseph and Wang 2004). However, the calculation of τ_{rz} in viscoelastic fluids is different than in Newtonian fluids. The additional pressure contribution p_c depends strongly on viscoelastic parameters and is determined solely by the irrotational flow.

21.2.5 The additional pressure contribution for capillary instability

Now we consider the additional pressure contribution for the potential flow analysis of capillary instability. Joseph and Wang (2004) showed that in linearized problems, the governing equation for the additional pressure contribution is

$$\nabla^2 p_c = 0. \tag{21.2.31}$$

It is easy to show that (21.2.31) holds for the viscoelastic fluid under consideration here. Solving (21.2.31), we obtain

$$-p_c = \sum_{j=0}^{\infty} C_j \mathrm{i} I_0(jr)\exp(\sigma t + \mathrm{i}jz), \tag{21.2.32}$$

where C_j are constants. With the additional pressure contribution, the normal stress balance becomes

$$-p_p - p_c + 2\hat{\mu}\frac{1}{\sqrt{J}}\frac{\partial u}{\partial r} = \frac{\partial^2 \eta}{\partial z^2} + \frac{\eta}{R^2}, \tag{21.2.33}$$

which gives rise to

$$\begin{aligned}&\left\{A\sigma I_0(kR) + C_k I_0(kR) + \frac{2\hat{\mu}k^2}{\sqrt{J}}A\left[I_0(kR) - \frac{I_1(kR)}{kR}\right]\right\}\exp(\sigma t + \mathrm{i}kz)\\ &+\sum_{j\neq k} C_j I_0(jR)\exp(\sigma t + \mathrm{i}jz) = A\frac{k}{\sigma}I_1(kR)\left(\frac{1}{R^2} - k^2\right)\exp(\sigma t + \mathrm{i}kz).\end{aligned} \tag{21.2.34}$$

By orthogonality of Fourier series, $C_j = 0$ if $j \neq k$. The coefficient C_k can be determined using (21.2.30). The left hand side of (21.2.30) is

$$\int_\Omega \tau_{rz} w^* \mathrm{d}\Omega = \frac{\hat{\mu}}{\sqrt{J}} 4\pi l R A A^* k^3 I_0(kR) I_1(kR)\exp(\sigma + \sigma^*)t, \tag{21.2.35}$$

where l is the length of one wave period and "*" denotes conjugate variables. On the other hand,

$$\int_\Omega (-p_c) u^* \mathrm{d}\Omega = 2\pi l R C_k A^* k I_0(kR) I_1(kR)\exp(\sigma + \sigma^*)t. \tag{21.2.36}$$

It follows that $C_k = 2\frac{\hat{\mu}}{\sqrt{J}}Ak^2$ and

$$-p_c = \mathrm{i}Ak^2\frac{2\hat{\mu}}{\sqrt{J}}I_0(kr)\exp(\sigma t + \mathrm{i}kz). \tag{21.2.37}$$

Inserting C_k into (21.2.34), we obtain

$$\sigma I_0(kR) + \frac{2\hat{\mu}k^2}{\sqrt{J}}I_0(kR) + \frac{2\hat{\mu}k^2}{\sqrt{J}}\left[I_0(kR) - \frac{I_1(kR)}{kR}\right] = \frac{k}{\sigma}I_1(kR)\left(\frac{1}{R^2} - k^2\right),$$

which can be written as

$$\frac{I_0(kR)}{I_1(kR)}\sigma^2\left(1 + \hat{\lambda}_1\sigma\right) + \left(1 + \hat{\lambda}_2\sigma\right)\sigma\frac{2k^2}{\sqrt{J}}\left[\frac{2I_0(kR)}{I_1(kR)} - \frac{1}{kR}\right] - k\left(\frac{1}{R^2} - k^2\right)\left(1 + \hat{\lambda}_1\sigma\right) = 0. \tag{21.2.38}$$

Equation (21.2.38) is the dispersion relation from the viscoelastic correction of VPF (VCVPF).

If the pressure correction (21.2.37) is inserted back into the governing equation (21.2.9), we obtain

$$\frac{\partial \boldsymbol{u}_c}{\partial t} = -\nabla p_c + \frac{\hat{\mu}}{\sqrt{J}}\nabla^2 \boldsymbol{u}_c, \tag{21.2.39}$$

where $\boldsymbol{u}_c$ is the velocity correction induced by the pressure correction p_c. We can find a potential flow solution $\boldsymbol{u}_c = \nabla\phi_c$, such that $\nabla^2\boldsymbol{u}_c = \nabla\nabla^2\phi_c = 0$ and

$$\nabla\frac{\partial}{\partial t}\phi_c = -\nabla p_c. \tag{21.2.40}$$

It can be readily shown that

$$\phi_c = \frac{\mathrm{i}}{\sigma} A k^2 \frac{2\hat{\mu}}{\sqrt{J}} I_0(kr) \exp(\sigma t + \mathrm{i}kz). \tag{21.2.41}$$

Thus the pressure correction p_c which is proportional to $J^{-1/2}$ induces a velocity correction proportional to $J^{-1/2}$. This velocity correction gives rise to uncompensated shear stress proportional to J^{-1} which may induce a new pressure correction now proportional to J^{-1}. In this way we may generate, successively, irrotational solutions proportional to increasing powers of $J^{-1/2}$. We believe that only the first pressure correction proportional to $J^{-1/2}$ is of physical significance; the higher order corrections are not considered in the normal stress balance (21.2.33).

21.2.6 Comparison of the growth rate

We compare the dispersion relation (21.2.38) from VCVPF with (21.2.24) from VPF, (21.2.25) from IPF and (21.2.17) from the exact solution. Equations (21.2.17), (21.2.24), (21.2.25) and (21.2.38) are solved by numerical methods for the growth rate σ and the values of σ are compared.

First we examine two practical cases: 2% PAA in air and 2% PEO in air (following Funada and Joseph 2003). We choose the diameter of the fluid cylinder to be 1 cm. The σ vs. k plots for 2% PAA and 2% PEO are shown in Figs. 21.14 and 21.15, respectively. These figures show that the results from VCVPF are almost indistinguishable from the exact solution, whereas IPF and VPF overestimates σ significantly.

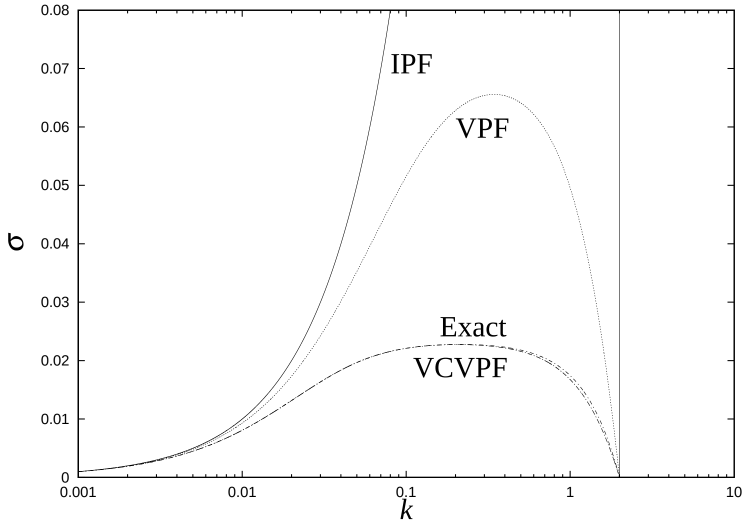

Fig. 21.14. The growth rate σ vs. k from inviscid potential flow (IPF), viscoelastic potential flow (VPF), viscoelastic correction of VPF (VCVPF) and the exact solution. The growth rates for the exact solution and VCVPF are almost the same. The fluid is 2% PAA, $\rho = 0.99$ g cm^{-1}, $\mu = 96$ P, $\gamma = 45.0$ dyn cm^{-1}, $\lambda_1 = 0.039$ s, $\lambda_2 = 0$ s, $J = 4.834 \times 10^{-3}$, $\hat{\lambda}_1 = 0.263$.

Capillary instability is controlled by three dimensionless numbers: J, $\hat{\lambda}_1$, and $\hat{\lambda}_2$. We vary these parameters and present the computed growth rate in Figs. 21.16–21.19. The Reynolds number J ranges from 10^{-4} to 10^4, $\hat{\lambda}_1$ ranges from 0.1 to 1000, and $\hat{\lambda}_2$ ranges from 0 to 100. In all the cases, the growth rates from VCVPF are in excellent agreement with the exact solution, indicating that our additional pressure contribution is valid for a wide range of controlling parameters.

Figures 21.16 and 21.17 show that the growth rates increase with $\hat{\lambda}_1$ when J and $\hat{\lambda}_2$ are fixed. Comparing Figs. 21.17 and 21.18, it can be seen that the effect of $\hat{\lambda}_2$ is opposite to that of $\hat{\lambda}_1$; the growth rates decreases with $\hat{\lambda}_2$. When $\hat{\lambda}_1 = \hat{\lambda}_2$, the fluid becomes Newtonian. When the Reynolds number is as high as 10^4 (Fig. 21.19), IPF and VPF slightly over-estimate the maximum growth rate whereas the VCVPF results are almost the same as the the exact solution.

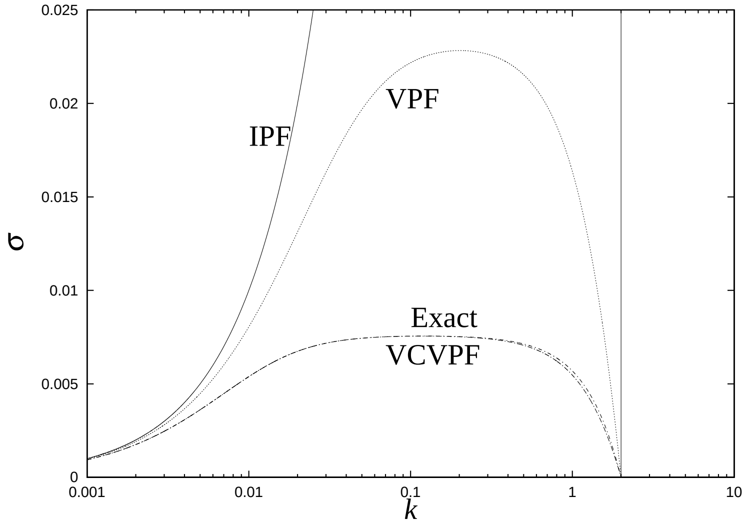

Fig. 21.15. The growth rate σ vs. k from inviscid potential flow (IPF), viscoelastic potential flow (VPF), viscoelastic correction of VPF (VCVPF) and the exact solution. The results of the exact solution and VCVPF are almost the same. The fluid is 2% PEO, $\rho = 0.99$ g cm^{-1}, $\mu = 350$ P, $\gamma = 63.0$ dyn cm^{-1}, $\lambda_1 = 0.21$ s, $\lambda_2 = 0$ s, $J = 5.091 \times 10^{-4}$, $\hat{\lambda}_1 = 1.676$.

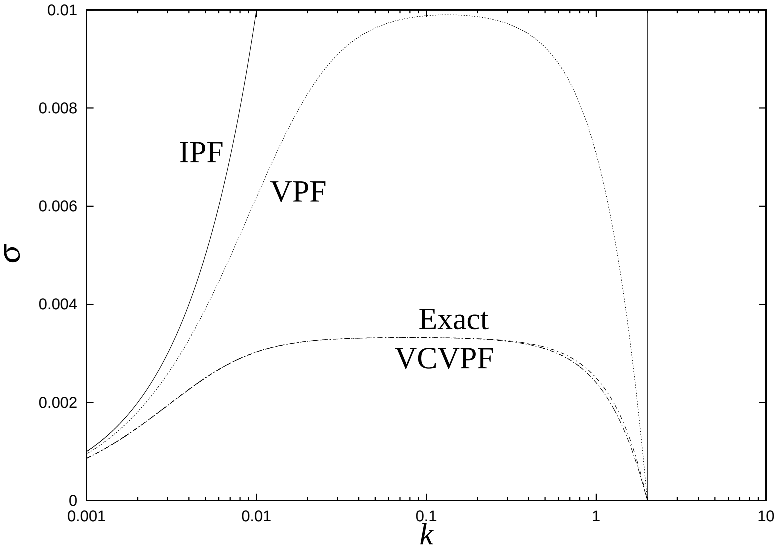

Fig. 21.16. The growth rate σ vs. k from inviscid potential flow (IPF), viscoelastic potential flow (VPF), viscoelastic correction of VPF (VCVPF) the exact solution. $J = 10^{-4}$, $\hat{\lambda}_1 = 0.1$, $\hat{\lambda}_2 = 0$.

In Table 21.7 we present the maximum growth rate σ_m and the associated wavenumber k_m computed from VPF, VCVPF and the exact solution. The value of σ_m given by VPF is several times larger than the exact result when J is small. VCVPF gives excellent approximation to the values of σ_m and k_m in all the cases.

21.2.7 Comparison of the stream function

Next we compare the stream functions from VPF, VCVPF and the exact solution at the same wave number. The wave number chosen for the comparison is k_m at which the maximum growth rate σ_m occurs in the exact solution. The relation between the constants A_1 and A_2 in the exact stream function (21.2.15) and A in the potential flow solution (21.2.22) must be established before one can compare the stream functions. Here this relation is obtained by assuming that the magnitude of the disturbance H is the same in the exact solution and in the potential flow solution.

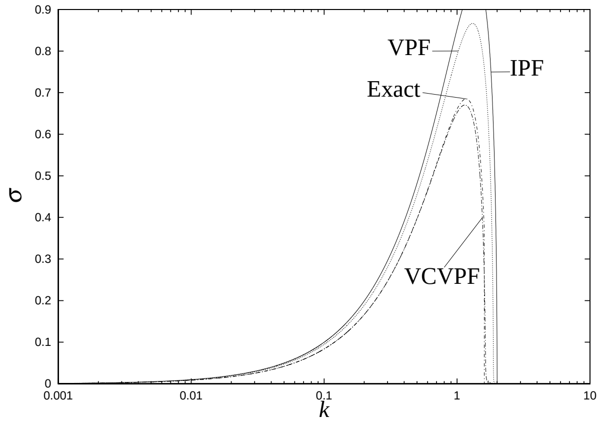

Fig. 21.17. The growth rate σ vs. k from inviscid potential flow (IPF), viscoelastic potential flow (VPF), viscoelastic correction of VPF (VCVPF) and the exact solution. $J = 10^{-4}$, $\hat{\lambda}_1 = 1000$, $\hat{\lambda}_2 = 0$.

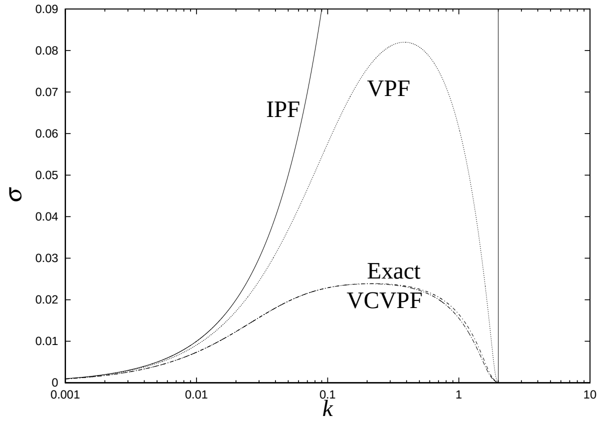

Fig. 21.18. The growth rate σ vs. k from inviscid potential flow (IPF), viscoelastic potential flow (VPF), viscoelastic correction of VPF (VCVPF) and the exact solution. $J = 10^{-4}$, $\hat{\lambda}_1 = 1000$, $\hat{\lambda}_2 = 100$.

We use a superscript 'E' for quantities appearing in the exact solution and (21.2.15) and (21.2.16) are rewritten as

$$\psi^E = \left[A_1^E r I_1(kr) + A_2^E r I_1(k_v r)\right]\exp(\sigma^E t + \mathrm{i}kz), \tag{21.2.42}$$

$$\eta^E = H^E \exp(\sigma^E t + \mathrm{i}kz). \tag{21.2.43}$$

The relation between A_1^E and A_2^E is determined by the zero-shear-stress condition at $r \approx R$:

$$A_2^E = \frac{-2k^2 I_1(kR)}{(k^2 + k_v^2) I_1(k_v R)} A_1^E. \tag{21.2.44}$$

Therefore we can write the stream function as

$$\psi^E = A_1^E r\left[I_1(kr) - \frac{2k^2 I_1(kR)}{(k^2 + k_v^2) I_1(k_v R)} I_1(k_v r)\right]\exp(\sigma^E t + \mathrm{i}kz). \tag{21.2.45}$$

The amplitude of the disturbance H^E is related to A_1^E through the kinematic condition:

$$H^E = \frac{\mathrm{i}k}{\sigma^E}\left(1 - \frac{2k^2}{k^2 + k_v^2}\right) I_1(kR) A_1^E. \tag{21.2.46}$$

Now we consider the potential flow solution which is indicated by a superscript 'P'. The stream function and the disturbance are given by

$$\psi^P = A^P r I_1(kr)\exp(\sigma^P t + \mathrm{i}kz), \tag{21.2.47}$$

$$\eta^P = H^P \exp(\sigma^P t + \mathrm{i}kz), \tag{21.2.48}$$

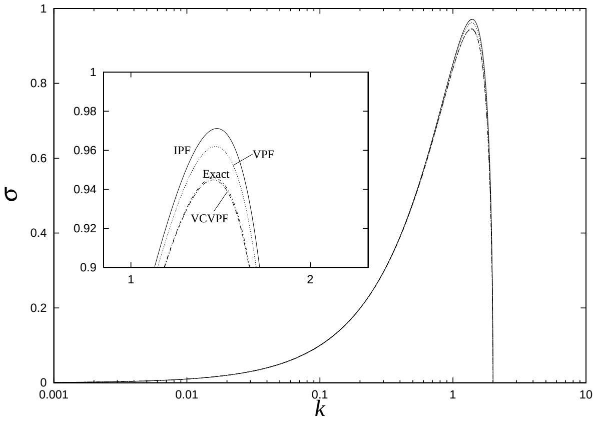

Fig. 21.19. The growth rate σ vs. k from inviscid potential flow (IPF), viscoelastic potential flow (VPF), viscoelastic correction of VPF (VCVPF) and the exact solution. $J = 10^4$, $\hat{\lambda}_1 = 0.1$, $\hat{\lambda}_2 = 0$. When the Reynolds number J is large, viscoelastic effects are relatively small, and the four curves are close; but differences among them can be seen near the peak growth rate. The inset is the amplified plot for the region near the peak growth rate. VCVPF is the best approximation to the exact solution.

Table 21.7. *Maximum growth rate σ_m and the associated wavenumber k_m for viscoelastic potential flow (VPF), viscoelastic correction of VPF (VCVPF) and the exact solution in Figs. 21.14–21.19. For inviscid potential flow (IPF) solution, k_m =1.394 and σ_m =0.9711 in all the 6 cases.*

Fig.	VPF		VCVPF		exact solution	
	k_m	σ_m	k_m	σ_m	k_m	σ_m
21.14	3.439e-01	6.557e-02	2.052e-01	2.274e-02	2.135e-01	2.278e-02
21.15	2.025e-01	2.283e-02	1.183e-01	7.554e-03	1.229e-01	7.559e-03
21.16	1.331e-01	9.899e-03	7.831e-02	3.322e-03	8.154e-02	3.323e-03
21.17	1.309e+00	8.665e-01	1.144e+00	6.703e-01	1.170e+00	6.850e-01
21.18	3.848e-01	8.200e-02	2.101e-01	2.384e-02	2.186e-01	2.390e-02
21.19	1.386e+00	9.618e-01	1.374e+00	9.447e-01	1.375e+00	9.458e-01

respectively. The amplitude of the disturbance H^P is related to A^P through the kinematic condition:

$$H^P = \frac{\mathrm{i}k}{\sigma^P} A^P I_1(kR). \tag{21.2.49}$$

We assume that the amplitude of the disturbance is the same in the exact solution and the potential flow solution. Thus $H^E = H^P$ and it follows that

$$A^P = A_1^E \frac{\sigma^P}{\sigma^E} \left(1 - \frac{2k^2}{k^2 + k_v^2}\right). \tag{21.2.50}$$

Then the stream function of the potential flow can be written as

$$\psi^P = A_1^E \frac{\sigma^P}{\sigma^E} \left(1 - \frac{2k^2}{k^2 + k_v^2}\right) r I_1(kr) \exp(\sigma^P t + \mathrm{i}kz). \tag{21.2.51}$$

Now we can compare (21.2.45) and (21.2.51). The stream function is decomposed into two parts, the exponential function depending on t and z and the rest part depending on r. Since we are comparing the stream functions at the same wave number k_m, the comparison of the exponential function is equivalent to the comparison of the growth rate. In Table 21.8, we list the values of the growth rate σ computed from VPF, VCVPF and the exact solution. In all the cases, the growth rate from VPF is larger than the exact result, whereas the growth rate

Table 21.8. *The growth rate σ computed from viscoelastic potential flow (VPF), viscoelastic correction of VPF (VCVPF) and the exact solution at the same wave number k_m. In the exact solution, k_m is the wave number for the maximum growth rate.*

J	$\hat{\lambda}_1$	$\hat{\lambda}_2$	k_m	σ^{VPF}	σ^{VCVPF}	σ^E
4.834×10^{-3}	0.263	0	0.2135	0.06345	0.02274	0.02278
5.091×10^{-4}	1.676	0	0.1229	0.02252	0.007554	0.007559
10^{-4}	0.1	0	0.08154	0.009843	0.003322	0.003323
10^{-4}	1000	0	1.170	0.8495	0.6696	0.6850
10^{-4}	1000	100	0.2186	0.07718	0.02384	0.02390
10^{4}	0.1	0	1.375	0.9617	0.9447	0.9458

from VCVPF is very close to the exact result. The rest part of the stream function depends on r and we define

$$SF(r) = \frac{\sigma^{VPF}}{\sigma^E}\left(1 - \frac{2k^2}{k^2 + k_v^2}\right) r I_1(kr) \quad \text{for} \quad \text{VPF}; \tag{21.2.52}$$

$$SF(r) = \frac{\sigma^{VCVPF}}{\sigma^E}\left(1 - \frac{2k^2}{k^2 + k_v^2}\right) r I_1(kr) \quad \text{for} \quad \text{VCVPF}; \tag{21.2.53}$$

$$SF(r) = r\left[I_1(kr) - \frac{2k^2 I_1(kR)}{(k^2 + k_v^2) I_1(k_v R)} I_1(k_v r)\right] \quad \text{for} \quad \text{the exact solution.} \tag{21.2.54}$$

Three examples for the comparison of the function $SF(r)$ are shown in Figs. 21.20, 21.21 and 21.22. The curves for $SF(r)$ are very close to straight lines, indicating power functions. This can also be seen from (21.2.52), (21.2.53) and (21.2.54). The expansion of the modified Bessel function gives

$$I_1(kr) = \frac{kr}{2} + \frac{k^3 r^3}{16} + \frac{k^5 r^5}{384} + O(r^7). \tag{21.2.55}$$

Higher order terms of r may be neglected because $0 \leq r \leq 0.5$ inside the cylinder. If we only keep the first term in the expansion, the stream functions (21.2.52) and (21.2.53) become, respectively

$$SF(r) = \frac{\sigma^{VPF}}{\sigma^E}\left(1 - \frac{2k^2}{k^2 + k_v^2}\right)\frac{kr^2}{2} + O(r^4) \quad \text{for} \quad \text{VPF}; \tag{21.2.56}$$

$$SF(r) = \frac{\sigma^{VCVPF}}{\sigma^E}\left(1 - \frac{2k^2}{k^2 + k_v^2}\right)\frac{kr^2}{2} + O(r^4) \quad \text{for} \quad \text{VCVPF}. \tag{21.2.57}$$

For (21.2.54), we also expand $I_1(kR)$ and $I_1(k_v R)$ and keep only the leading term, which gives rise to

$$\begin{aligned} SF(r) &= \frac{kr^2}{2} - \frac{2k^2 \frac{kR}{2}}{(k^2 + k_v^2)\frac{k_v R}{2}} \frac{k_v r^2}{2} + O(r^4) \\ &= \left(1 - \frac{2k^2}{k^2 + k_v^2}\right)\frac{kr^2}{2} + O(r^4) \quad \text{for} \quad \text{the exact solution.} \end{aligned} \tag{21.2.58}$$

Equations (21.2.56), (21.2.57) and (21.2.58) show that the functions $SF(r)$ are approximately quadratic functions for small r and this is confirmed in Figs. 21.20, 21.21 and 21.22. The comparison of the leading terms of $SF(r)$ depends directly on the growth rate σ^{VPF}, σ^{VCVPF} and σ^E. Since $\sigma^{VPF} > \sigma^E$, the curves for $SF(r)$ of VPF are higher than those for the exact solution. On the other hand, σ^{VCVPF} is very close to σ^E and the curves for VCVPF and the exact solution almost overlap. Combining the comparison of the growth rate in Table 21.8 and the comparison of the function $SF(r)$ in Figs. 21.20, 21.21 and 21.22, we show that the stream function given by VCVPF is in remarkably good agreement with the exact solution. This result indicates that the vorticity plays a small role in the exact solution and our VCVPF solution, which is based solely on potential flow, can give an excellent approximation to the flow.

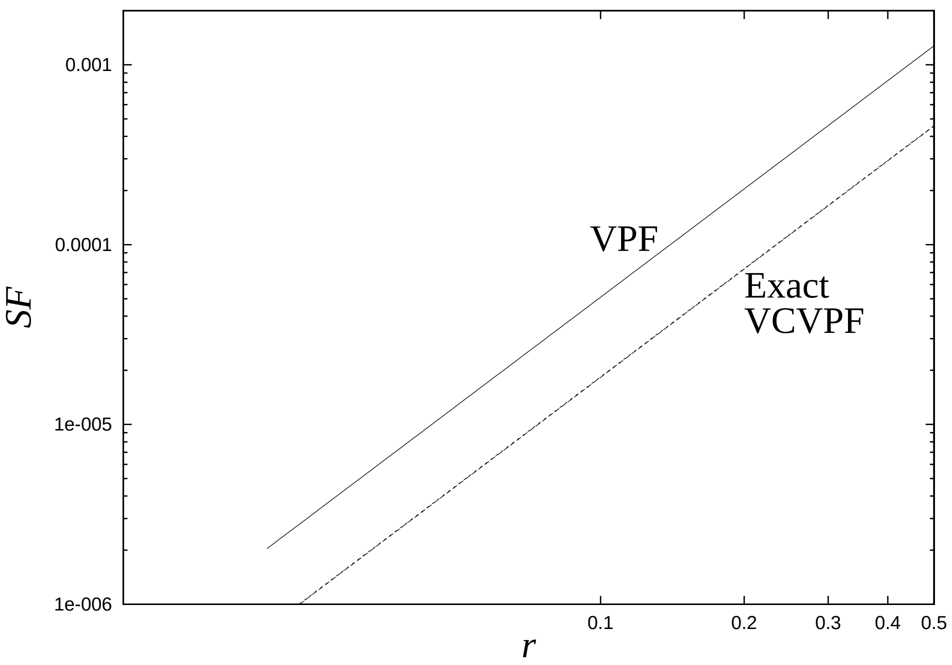

Fig. 21.20. The part of the stream function depending on r defined in (21.2.52), (21.2.53) and (21.2.54) for viscoelastic potential flow (VPF), viscoelastic correction of VPF (VCVPF) and the exact solution respectively. The fluid is 2% PAA, $J = 4.834 \times 10^{-3}$, $\hat{\lambda}_1 = 0.263$, $\hat{\lambda}_2 = 0$. The wave number for the maximum growth rate $k_m = 0.2135$ is chosen for the comparison.

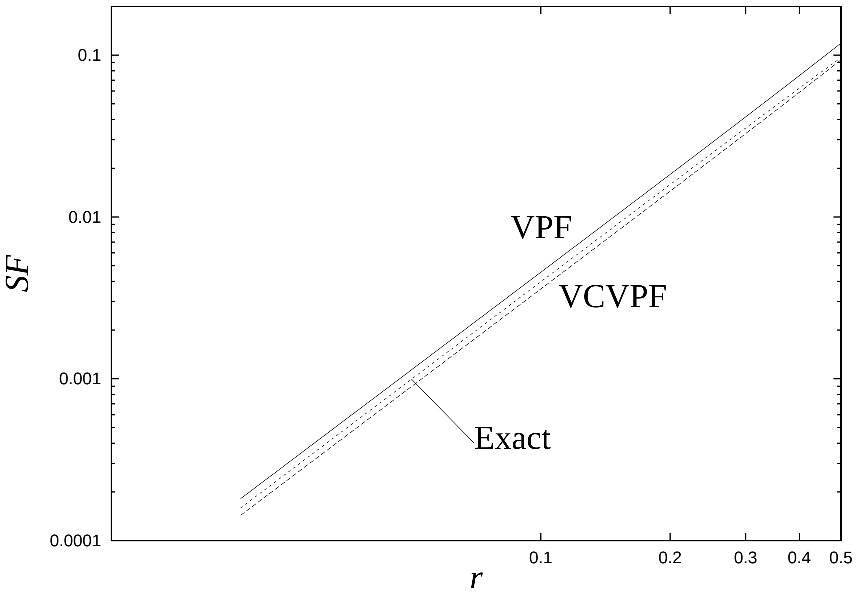

Fig. 21.21. The part of the stream function depending on r defined in (21.2.52), (21.2.53) and (21.2.54) for viscoelastic potential flow (VPF), viscoelastic correction of VPF (VCVPF) and the exact solution respectively. In this case, $J = 10^{-4}$, $\hat{\lambda}_1 = 1000$, $\hat{\lambda}_2 = 0$. The wave number for the maximum growth rate $k_m = 1.170$ is chosen for the comparison.

21.2.8 Discussion

Chang, Demekhin, and Kalaidin (1999) did a long wave study of the stretching dynamics of bead-string filaments for FENE and Oldroyd-B fluids. They also did a long wave study of linear stability and their results can be compared to ours. To this end, we first convert the parameters used by Chang *et al.* to the parameters used by us. In the notation of Chang *et al.* Ca is the capillary number, We is the Weissenberg number and S is the retardation number. We linearize the stress equation of Chang *et al.* and reduce it to a form comparable to our

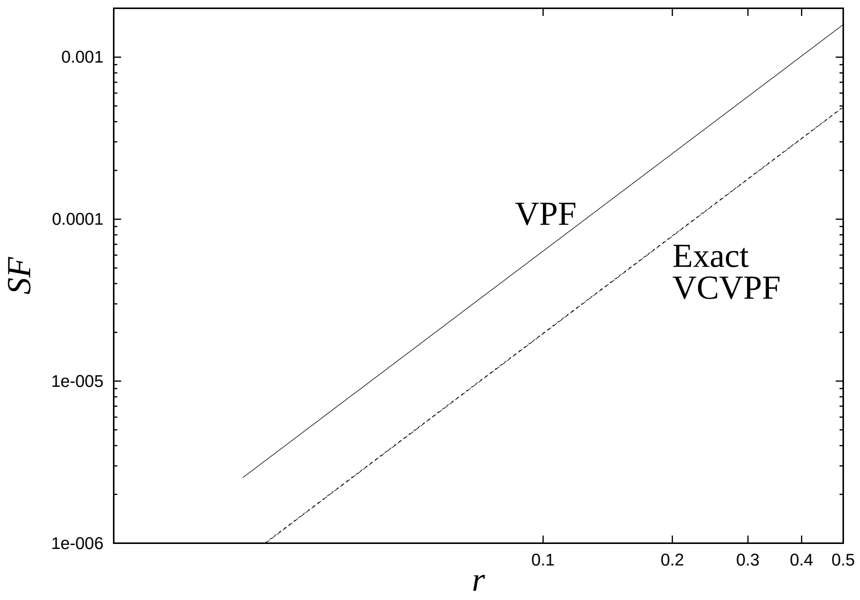

Fig. 21.22. The part of the stream function depending on r defined in (21.2.52), (21.2.53) and (21.2.54) for viscoelastic potential flow (VPF), viscoelastic correction of VPF (VCVPF) and the exact solution respectively. In this case, $J = 10^{-4}$, $\hat{\lambda}_1 = 1000$, $\hat{\lambda}_2 = 100$. The wave number for the maximum growth rate $k_m = 0.2186$ is chosen for the comparison.

Jeffreys model (21.2.3), then the relation between We and S used by Chang *et al.* and $\hat{\lambda}_1$ and $\hat{\lambda}_2$ used by us is revealed. After taking the different length and time scales into account, we can express the parameters in Chang *et al.* in terms of our parameters

$$Ca = 2/J, \quad We = 4\hat{\lambda}_1/\sqrt{J}, \quad \text{and} \quad S = \hat{\lambda}_2/\hat{\lambda}_1. \tag{21.2.59}$$

Then the dispersion relation given by the linear stability analysis of Chang *et al.* (their Equation (16)) can be written as

$$\hat{\lambda}_1\sigma^3 + \left(1 + 3k^2\frac{\hat{\lambda}_2}{\sqrt{J}}\right)\sigma^2 + \left[\frac{3k^2}{\sqrt{J}} - \frac{k^2\hat{\lambda}_1}{4}(4-k^2)\right]\sigma - \frac{k^2}{4}(4-k^2) = 0. \tag{21.2.60}$$

Now we consider the dispersion relation (21.2.38) from the VCVPF method. The dimensionless radius $R = 1/2$ and the Bessel functions can be expanded for small k

$$\frac{I_0(kR)}{I_1(kR)} = \frac{4}{k} + \frac{k}{8} - \frac{k^3}{768} + O(k^5), \quad \frac{2I_0(kR)}{I_1(kR)} - \frac{1}{kR} = \frac{6}{k} + \frac{k}{4} - \frac{k^3}{384} + O(k^5). \tag{21.2.61}$$

Inserting (21.2.61) into (21.2.38), we can obtain

$$\begin{aligned}&\left(1 + \frac{k^2}{32}\right)\hat{\lambda}_1\sigma^3 + \left[1 + \frac{k^2}{32} + 3k^2\frac{\hat{\lambda}_2}{\sqrt{J}}\left(1 + \frac{k^2}{24}\right)\right]\sigma^2 \\ &+ \left[\frac{3k^2}{\sqrt{J}}\left(1 + \frac{k^2}{24}\right) - \frac{k^2\hat{\lambda}_1}{4}(4-k^2)\right]\sigma - \frac{k^2}{4}(4-k^2) + O(k^4) = 0.\end{aligned} \tag{21.2.62}$$

The expansion of the Bessel functions can also be applied to the exact solution and the result will be compared to (21.2.60) and (21.2.62). After some arrangement, the dispersion relation (21.2.17) of the exact solution can be written as

$$\begin{aligned}&\frac{4k^3k_v}{\sqrt{J}}\hat{\mu}\left[\frac{I_0(k_vR)}{I_1(k_vR)} - \frac{1}{k_vR}\right] - \frac{2k^2(k^2+k_v^2)}{\sqrt{J}}\hat{\mu}\left[\frac{I_0(kR)}{I_1(kR)} - \frac{1}{kR}\right] \\ &- \frac{2k^3}{\sigma}\left(\frac{1}{R^2} - k^2\right) + (k^2+k_v^2)\frac{k}{\sigma}\left(\frac{1}{R^2} - k^2\right) - (k^2+k_v^2)\sigma\frac{I_0(kR)}{I_1(kR)} = 0.\end{aligned} \tag{21.2.63}$$

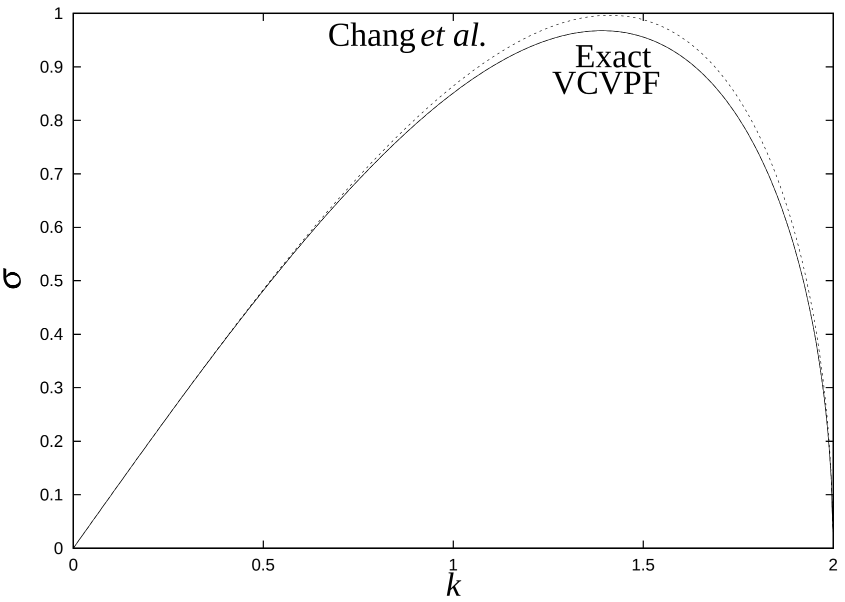

Fig. 21.23. The growth rate σ as a function of k computed using (21.2.60) given by Chang *et al.*, (21.2.38) given by our VCVPF method, and (21.2.17) given by the exact solution. The fluid is water with $\rho = 1000$ kg/m^3, $\mu = 0.001$ kg/(m s), $\gamma = 0.0728$ N/m. The diameter of the liquid cylinder is assumed to be 0.01 m and the Reynolds number is $J = 7.28 \times 10^5$.

After expanding the Bessel functions as power series of k, we obtain

$$\hat{\lambda}_1 \left(1 + \frac{k^2}{32}\right) \sigma^3 + \left(1 + \frac{k^2}{32} + 3k^2 \frac{\hat{\lambda}_2}{\sqrt{J}}\right) \sigma^2 + \left[\frac{3k^2}{\sqrt{J}} - \frac{k^2 \hat{\lambda}_1}{4}(4 - k^2)\right] \sigma - \frac{k^2}{4}(4 - k^2) + O(k^4) = 0. \quad (21.2.64)$$

The dispersion relation (21.2.64) given by the exact solution is different from both (21.2.60) given by Chang *et al.* and (21.2.62) given by our VCVPF method; the first order differences are $O(k^2)$ in both cases. The differences between (21.2.64) and (21.2.60) are two $k^2/32$ terms in the coefficients of σ^3 and σ^2; the differences between (21.2.64) and (21.2.62) are two $k^2/24$ terms in the coefficients of σ^2 and σ.

The limit of a Newtonian fluid can be obtained by letting $\hat{\lambda}_1 = \hat{\lambda}_2 = 0$. Then the dispersion relations (21.2.60), (21.2.62) and (21.2.64) reduce to, respectively

$$\sigma^2 + \frac{3k^2}{\sqrt{J}}\sigma - \frac{k^2}{4}(4 - k^2) = 0 \quad \text{for} \quad \text{Chang } et\ al. \ ; \qquad (21.2.65)$$

$$\left(1 + \frac{k^2}{32}\right) \sigma^2 + \frac{3k^2}{\sqrt{J}} \left(1 + \frac{k^2}{24}\right) \sigma - \frac{k^2}{4}(4 - k^2) + O(k^4) = 0 \quad \text{for} \quad \text{VCVPF}; \qquad (21.2.66)$$

$$\left(1 + \frac{k^2}{32}\right) \sigma^2 + \frac{3k^2}{\sqrt{J}}\sigma - \frac{k^2}{4}(4 - k^2) + O(k^4) = 0 \quad \text{for} \quad \text{the exact solution.} \qquad (21.2.67)$$

The first order differences among the dispersion relations (21.2.65), (21.2.66) and (21.2.67) are $O(k^2)$. The difference between (21.2.65) and (21.2.67) is a $k^2/32$ term in the coefficient of σ^2; the difference between (21.2.66) and (21.2.67) is a $k^2/24$ term in the coefficient of σ.

In Figs. 21.23 to 21.27, we plot the growth rate σ as a function of k computed using (21.2.60) given by Chang *et al.*, (21.2.38) given by our VCVPF method, and (21.2.17) given by the exact solution. Both Newtonian fluids and viscoelastic fluids are compared. The limit of Newtonian fluids is achieved by setting $\hat{\lambda}_1$ and $\hat{\lambda}_2$ to be zero in (21.2.60), (21.2.38) and (21.2.17). There is almost no difference between the three curves when k is close to zero, and small differences can be seen when k is close to 2. The dispersion relation of Chang *et al.* is in better agreement with the exact solution when the Reynolds number J is small (Figs. 21.24 – 21.27), whereas our VCVPF is in better agreement with the exact solution when J is large (Fig. 21.23).

In this work, linear stability analysis of the capillary instability of a viscoelastic thread is carried out under the assumption that the flow is irrotational. The non-zero irrotational shear stress at the surface of the liquid

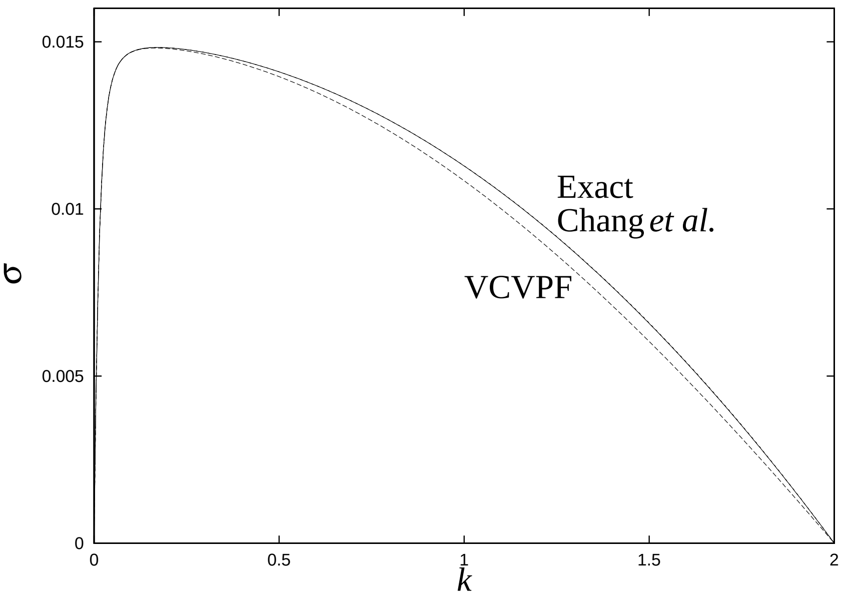

Fig. 21.24. The growth rate σ as a function of k computed using (21.2.60) given by Chang *et al.*, (21.2.38) given by our VCVPF method, and (21.2.17) given by the exact solution. The fluid is a Newtonian fluid SO10000 oil with $\rho = 969$ kg/m^3, $\mu = 10$ kg/(m s), $\gamma = 0.021$ N/m. The Reynolds number is $J = 2.04 \times 10^{-3}$.

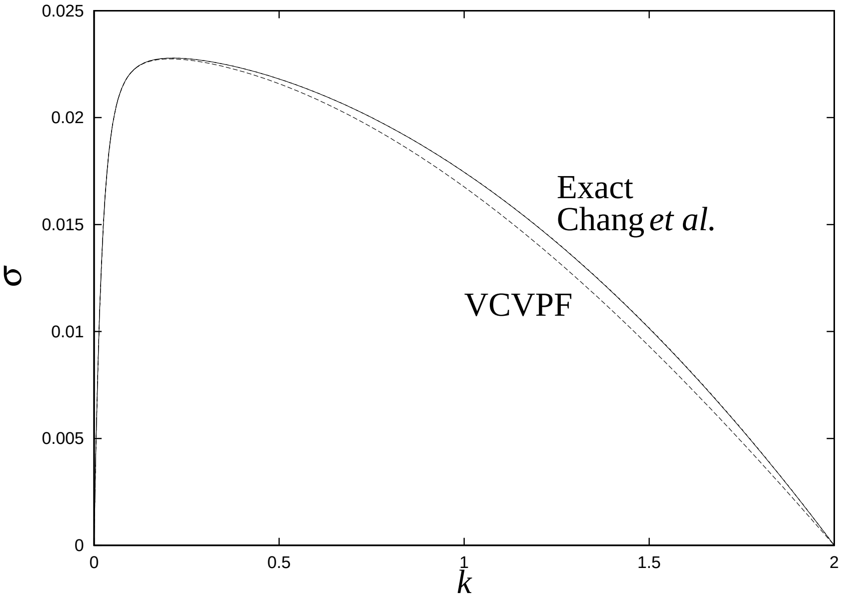

Fig. 21.25. The growth rate σ as a function of k computed using (21.2.60) given by Chang *et al.*, (21.2.38) given by our VCVPF method, and (21.2.17) given by the exact solution. The fluid is 2% PAA with $J = 4.834 \times 10^{-3}$, $\hat{\lambda}_1 = 0.263$, $\hat{\lambda}_2 = 0$.

thread does not agree with the zero-shear-stress condition. We derive a pressure contribution in addition to the irrotational pressure. This additional pressure contribution depends on the viscoelastic parameters and cancels out the power due to the uncompensated irrotational shear stress in the energy equation. We include the additional pressure contribution, the irrotational pressure and the extra stress evaluated using the irrotational flow in the normal stress balance at the surface, then a dispersion relation is obtained. We call this approach as the viscoelastic correction of the viscoelastic potential flow (VCVPF). The comparison of the growth rate and the stream function show that the VCVPF solution is an excellent approximation to the exact solution. The dispersion relation given by VCVPF is also compared to that obtained by Chang *et al.* (1999) using a long wave approximation. The differences between the two dispersion relations are negligible when the wave number k is small and both dispersion relations are in remarkably good agreement with the exact solution.

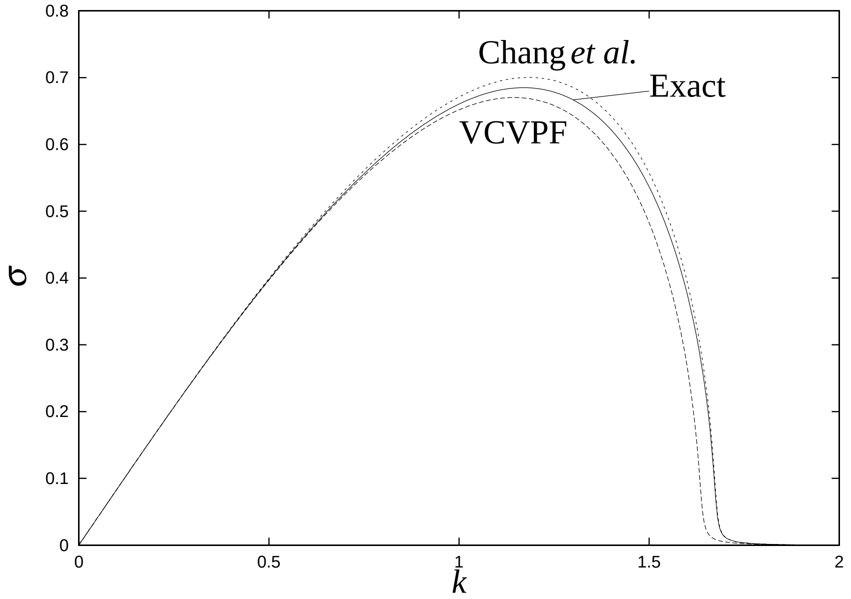

Fig. 21.26. The growth rate σ as a function of k computed using (21.2.60) given by Chang *et al.*, (21.2.38) given by our VCVPF method, and (21.2.17) given by the exact solution. The fluid is a viscoelastic fluid with $J = 10^{-4}$, $\hat{\lambda}_1 = 1000$, $\hat{\lambda}_2 = 0$.

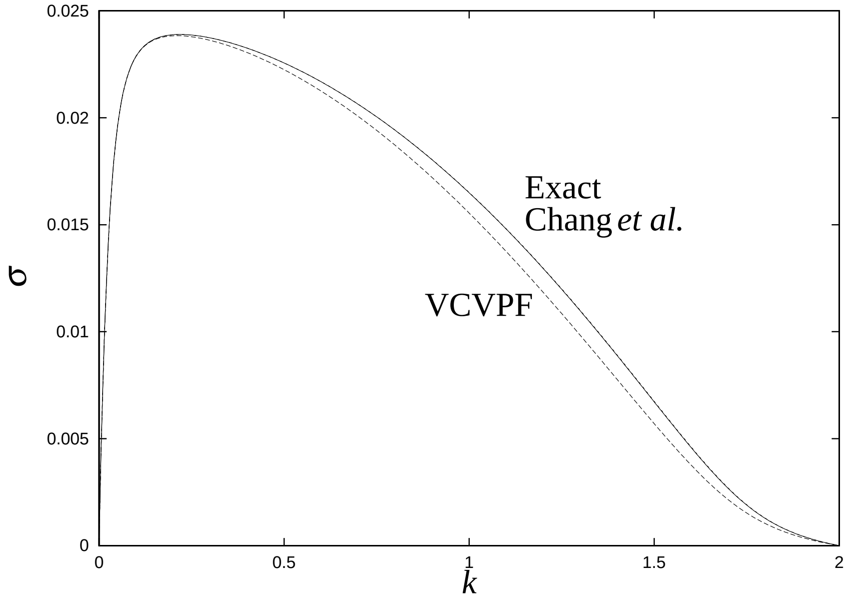

Fig. 21.27. The growth rate σ as a function of k computed using (21.2.60) given by Chang *et al.*, (21.2.38) given by our VCVPF method, and (21.2.17) given by the exact solution. The fluid is a viscoelastic fluid with $J = 10^{-4}$, $\hat{\lambda}_1 = 1000$, $\hat{\lambda}_2 = 100$.

21.3 Steady motion of a deforming gas bubble in a viscous potential flow

Miksis, Vanden-Broeck and Keller (MVK, 1982) computed the shape of an axisymmetric rising bubble, or a falling drop, in an incompressible fluid assuming that the flow in the liquid is irrotational but viscous. The boundary condition for the normal stress including surface tension is satisfied but as in other problems of VPF, the tangential stress is neglected. The shape function is obtained from the gravitational potential evaluated on the free surface; two shape functions are computed, one on the top and one on the bottom of the bubble. The shape is single valued on each function The potential function is obtained from the values of the potential on the free surface, using a Green's function approach following ideas introduced by Longuet-Higgins and Cokelet

1976, Vanden-Broeck and Keller 1980 and Miksis, Vanden-Broeck and Keller 1982. The system of differential and integral equations are solved in a frame in which the bubble is stationary and the velocity at infinity is U which is calculated by a drag balance in two ways. The first calculation is like that of Moore 1959 in which the drag comes from the normal irrotational viscous stress leading to $32/R$. This direct method should not be used because of the additional contribution due to the irrotational viscous pressure.

This pressure is not easy to calculate in general, but the correct drag leading to $48/R$ can be obtained, and was obtained by MVK in a second calculation using the dissipation method.

The solution of the system of governing equations was obtained as a power series in the Weber number and R^{-1} and is therefore restricted to low Weber numbers (large surface tension) and high Reynolds numbers (small viscosity).

22

Numerical methods for irrotational flows of viscous fluid

Problems of potential flow in irregular domains bounded by rigid solids and satisfying perhaps conditions at infinity require numerical methods. Computers and software are now so powerful that it can be easier to compute a solution than to find the exact one in a reference book. There are many techniques which may be used to solve Laplaces equation with prescribed boundary conditions. These techniques are readably available even in "search" on the web.

The numerical simulation of the deformation of interfaces between two immiscible fluids or in gas-liquid flows is currently an active topic of research and many options are available for researchers. Level set methods associated with the names of S. Osher. R. Fedkiw and J. Sethian, volume of fluid methods associated with the name of S. Zaleski and front tracking methods associated with the name of G. Trygvasson, are high among the most popular methods. Readers can find references in the comprehensive reviews by Yeung (1982), Tsai and Yue (1996) and Scardovelli and Zaleski (1999) or in "search" on Google.

22.1 Perturbation methods

The problem of numerical simulation of the shape of free surfaces in potential flows of inviscid fluids has been considered by various authors. Perturbation methods for nonlinear irrotational waves on an inviscid fluid were introduced by Stokes 1847. He expanded the solution in powers of the amplitude. Many authors have worked with these series and proofs of convergence and non-convergence have been considered (Schwartz, 1975). A mapping method for the perturbation series was presented by Joseph 1973. Yoo 1973 computed many terms. The mapping method was devised to justify an apparent problem of Stokes method in which boundary conditions at $z = \eta$ are enforced on the unperturbed surface at $z = 0$

The problem of computer aided studies and analytical continuation of the perturbation series has been considered by L.Schwartz 1975. The main contribution of this paper is summation protocol base Padé approximations which in many cases improve convergence.

Stokes' waves cannot be permanently maintained in the presence of viscosity. This fact places certain limits on the utility of the perturbation methods.

22.2 Boundary integral methods for inviscid potential flow

A major objective in the solution of interfacial flow problems is a highly accurate description of the interface. Therefore, boundary integral techniques are a fitting choice for the analysis, since they seek solutions of integral equations involving information only on the interface. This feature reduces the dimensionality of the problem by one. Thus, when an approximate solution is sought, a fine mesh can be afforded on the interface especially in regions with high curvature, without having to discretize the neighboring domain. This attribute is particularly important for an unbounded domain, in which case appropriate boundary conditions at infinity can be satisfied automatically by the governing integral equations. A survey of the literature on free-surface or interfacial flows indicates that boundary integral methods have been applied mostly to problems in two-dimensions or three-dimensions with axial symmetry since domain discretization simply takes place over a curve in the plane for these cases.

The application of the boundary integral method relies on the existence of a 'fundamental solution' for the partial differential equation on hand. In particular, this solution is known for the Laplace's equation. Therefore, BEM becomes a useful tool for incompressible potential flow problems since the velocity potential is harmonic. BEM formulations have also been developed for Stokes flow (Pozrikidis 1992).

In general, boundary integral methods can be grouped into two major categories, namely, the indirect and the direct formulations (Banerjee and Butterfield 1981; Brebbia, Telles and Wrobel 1984). In the indirect formulation an integral equation is written in terms of the density distribution over the boundary of a unit singular solution of the partial differential equation of interest. Numerical techniques are then applied to compute this density profile which may have no explicit physical connotation. Once the density function over the boundary has been determined, the physical variables of the problem inside the domain can be obtained by integration. On the other hand, the direct formulation poses integral equations on the boundaries in terms of the physical parameters of interest. By enforcing the boundary conditions, one can solve for the unknown field on the boundary first and then at particular locations on the interior. For instance, the normal derivative of the potential at the boundary can be computed in the Dirichlet problem or the potential over the boundary in the Neumann problem. Also, mixed boundary conditions can be easily handled.

For most of the problems of interest in science and engineering, finding a solution of the boundary integral equations is only possible in an approximate manner, using numerical techniques. A widely used approach is the boundary element method (BEM). In general terms, this method sets marker points or nodes on the boundary. A number of segments or 'elements' connecting the nodes are used to approximate this boundary. In two dimensions, these elements may be straight segments or, if greater accuracy is desired, of higher order, including circular, parabolic or cubic representations. In three dimensions, triangular or quadrilateral elements may be chosen. Regarding the fields functions taken to the boundary (e.g., the potential and its normal derivative), they are approximated with a truncated polynomial over each element. For instance, the simplest choice is to hold the function constant on the element. To improve accuracy, the linear expansion or higher-order approximations may be used. The coefficients of the expansion correspond to the values of the function at particular locations on the element, which may be those of the nodes. Next, the integrals on the boundary integral equation are split into integrals evaluated over each element and the local expansions for the field functions are substituted. Then, the discretized equation is satisfied at a set of collocation points on the boundary. This process gives rise to a set of algebraic equations that may be solved for the vector of unknowns. Detailed descriptions on the implementation of BEM can be found in monographs on the subject, such as those by Brebbia et al. (1984), Pozrikidis (1992) and Wrobel (2002), among others. A fairly rigorous mathematical treatment of boundary integral equations and their numerical solution is given by Jaswon and Symm (1977).

Examples of the applications of boundary integral methods to problems involving free-surface flows are abundant. For instance, the inviscid analysis of steady motion of free surfaces is carried out by Byatt-Smith and Longuet-Higgins (1976) for a steep solitary wave, by Miksis, Vanden-Broeck and Keller (1981) to study the deformation of an axisymmetric bubble in a uniform flow using a direct formulation and by Meiron and Saffman (1983) for interfacial gravity waves applying the indirect formulation.

The accurate description of the unsteady motion of free surfaces or fluid-fluid interfaces bounding regions of inviscid irrotational flow can be performed using boundary integral techniques. An approach that arises from the indirect double-layer potential formulation is the generalized vortex method. This method was presented and developed by Baker, Meiron and Orszag (1980, 1982, 1984) in a series of publications. They obtained an integral equation for the Lagrangian time derivative of the dipole density distribution over the boundary. Solving for this time derivative allows updating the dipole density which is used to march the interface forward in time. Baker et al. (1980) used the vortex method to simulate the Rayleigh-Taylor instability in its classical form while Verdon et al. (1982) considered the acceleration of a thin fluid layer. Baker et al. (1982) applied the method to the breaking of surface waves and interacting triads of surface and interfacial waves. Lundgren and

Mansour (1988, 1991) studied the oscillations of an inviscid axisymmetric drop in a dynamically inactive fluid (e.g., vacuum) and the motion of toroidal gas bubbles in an inviscid liquid, respectively, with a modified version of the generalized vortex method. Mansour and Lundgren 1990 also applied this approach to model satellite formation in capillary jet breakup. The vortex method based upon the indirect approach has been used to study the dynamic breakup of an inviscid liquid bridge by Chen and Steen 1997 and capillary pinch-off of an inviscid drop surrounded by an ambient inviscid fluid by Leppinen and Lister (2003).

The direct formulation of the boundary integral method for inviscid fluids has been used by Longuet-Higgins and Cokelet (1976) to study the deformation of steep surface waves and by Keller and Miksis (1983) to model a breaking sheet of liquid and the flow near the intersection of a solid boundary with the free surface of a liquid. The direct approach is applied to problems of capillary pinch off by Day, Hinch and Lister (1998) and Rodriguez-Rodriguez et al (2006). Several papers by Oguz and Prosperetti (1989, 1990, 1993) on the effect of surface tension in the contact of liquid surfaces, bubble entrainment by the impact of drops on liquid surfaces and dynamics of bubble growth with detachment from a needle, respectively, use the direct formulation of boundary integral methods. Machane and Canot (1997) present applications of BEM for various two-dimensional and axisymmetric free-surface problems.

22.3 Boundary integral methods for viscous potential flow

BEM has been extended to accommodate the effects of viscosity in a purely irrotational flow by Georgescu, Achard and Canot (2002) to study a gas bubble bursting at a free surface and by Canot et al (2003) in their numerical simulation of the buoyancy-driven bouncing of a 2-D bubble at a horizontal wall using the direct formulation. Their interesting approach will be discussed in Chapter 18.4. Another kind of viscous potential flow analysis of the deformation of a rising 3-D bubble was given by Miksis, Vanden-Broeck and Keller 1982. They converted their problem into a system of integro-differential equations which they solved under the conditions of small Weber numbers and large Reynolds numbers.

Lundgren and Mansour (1988) also included the effect of a small viscosity by decomposing the velocity field into the sum of an irrotational and a rotational velocity, in which the former is expressed as the gradient of a potential and the latter is written as the curl of a vector potential. Substitution of this decomposition into the incompressible Navier-Stokes equations and applying order-of-magnitude arguments under the assumption of a thin vortical layer at the free surface of the drop yields a new set of differential equations for the potentials. These equations carry weak viscous effects and are coupled with the boundary integral formulation for potential flow based on the vortex method.

Weak viscous effects emanating from boundary layers in which vorticity does not vanish are associated with the quasipotential methodology discussed in §14.1.7.

The BEM calculations of Georgescu et al 2002 and Canot et al 2003 neglect vorticity but the viscous effects in the purely irrotational flow are not restricted to small viscosity.

22.4 Boundary integral methods for effects of viscosity and surface tension on steep surface waves

Longuet-Higgins and Cokelet 1976 (hereafter LHC) wrote a seminal paper in which they computed the shape of steep surface waves on an inviscid liquid (called water) using the direct formulation of BEM; surface tension and viscosity were neglected. The problem considered by LHC is briefly described in the caption to Fig. 22.1.

Our goal here is to extend the methods used by LHC to include the effects of viscosity and surface tension. The presentation of LHC is very efficient. We are going to follow their analysis but with surface tension included. The analysis of LHC is based on the direct formulation of BEM which in turn is an application of Green's third

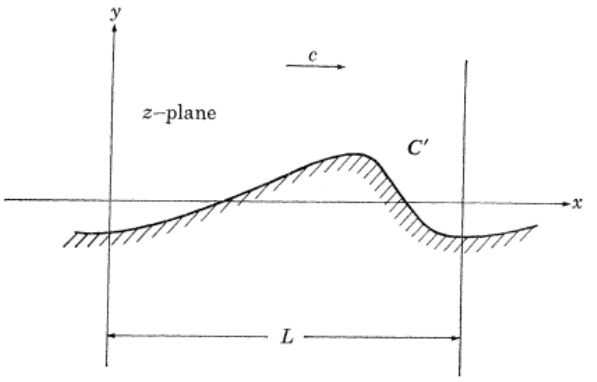

Fig. 22.1. Periodic progressive wave with period $L = 2\pi/k$ and speed c. The velocity is given by a harmonic potential, with a zero horizontal average $\overline{\nabla\phi} = 0$ which as $y \to -\infty$, at great depths. The unsteady wave is produced by initially applying an asymmetric distribution of pressure to a symmetric progressive wave. It is striking that they were able to compute the shape of breaking surface waves (Fig. 22.2).

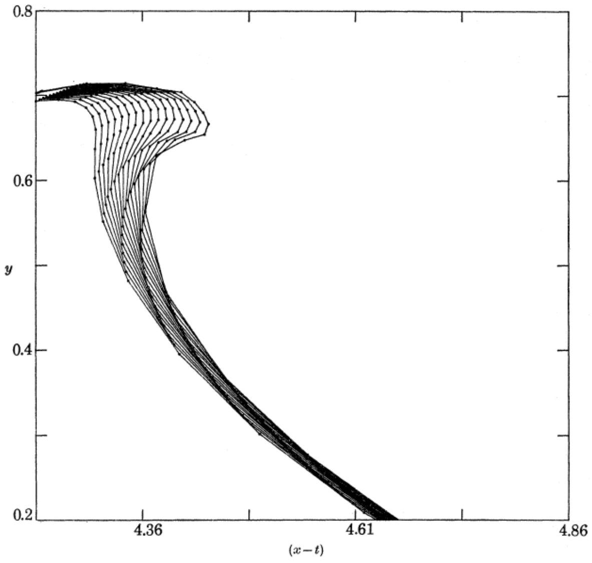

Fig. 22.2. (Figure 8 of Longuet-Higgins and Cokelet 1976) Close-up of the wave crest at successive times.

identity. A simple derivation of Green's third identity in 3D can be found on pages 55-56 in Milne Thomson 1959. The 2D result, needed here, follows along the same lines and can be found in many books.

Let $\Omega(t)$ be the plane 2D region of flow and $S(t)$ is the plane curve, with outward normal $\boldsymbol{n}$, defining the boundary of $\Omega(t)$; $\nabla^2\phi = 0$ on $\Omega(t)$ and $S(t)$. Let

$$\left.\begin{aligned} \boldsymbol{x}_0 &= \boldsymbol{e}_x x_0 + \boldsymbol{e}_y y_0 \ \in \Omega(t), \\ \boldsymbol{x} &= \boldsymbol{e}_x x + \boldsymbol{e}_y y \ \in S(t). \end{aligned}\right\} \tag{22.4.1}$$

Green's third identity is

$$\left.\begin{aligned} \alpha(\boldsymbol{x}_0)\phi(\boldsymbol{x}_0) &= \int_{S(t)} \left[\frac{\partial\phi(\boldsymbol{x})}{\partial n} G(\boldsymbol{x}_0, \boldsymbol{x}) - \phi(\boldsymbol{x}) \frac{\partial G(\boldsymbol{x}_0, \boldsymbol{x})}{\partial n}\right] \mathrm{d}S, \\ G(\boldsymbol{x}_0, \boldsymbol{x}) &= \log \frac{1}{|\boldsymbol{x}_0 - \boldsymbol{x}|}, \quad \alpha(\boldsymbol{x}_0) = 2\pi. \end{aligned}\right\} \tag{22.4.2}$$

If $\boldsymbol{x}_0$ is taken to the boundary, in the limit, then $\alpha(\boldsymbol{x}_0)\phi(\boldsymbol{x}_0) = \pi\phi(\boldsymbol{x}_0)$ with $\boldsymbol{x}_0 \in S(t)$, $\alpha = \pi$ instead of 2π on the left side of (22.4.2).

The flow is assumed to be purely irrotational $\boldsymbol{u} = \nabla\phi$, $\nabla^2\phi = 0$. The problem is solved in dimensionless form; the length scale is L, the time scale is L/U where $U=\sqrt{gL}$. The evolution of dynamics is governed by the normal stress balance

$$\frac{\partial\phi}{\partial t}=-p_s-y-\frac{1}{2}\left|\nabla\phi\right|^2-\frac{2}{Re}\frac{\partial^2\phi}{\partial n^2}-\frac{\kappa}{We} \tag{22.4.3}$$

where $p_s=\left(p_a-p_\infty\right)/\rho U^2$, p_a is air pressure, p_∞ is the pressure in the water at great depths where there is no motion, $Re=UL/\nu$ is the Reynolds number, $We=\rho LU^2/\gamma$ is the Weber number and $\kappa=1/r$ is curvature where r is the radius of the circle with the same tangent and curvature as the scaled boundary curve $\tilde{C}(t)$ corresponding to $\delta(t)$. The arc length $\tilde{C}(t)$ is dimensionless and designated by S, independent of t. The terms associated with Re and We were not considered by LHC.

The procedure folowed by LHC is Lagrangian, the free surface and ϕ are updated following particles of $\tilde{C}(t)$. Since

$$\frac{\mathrm{d}\phi}{\mathrm{d}t}=\frac{\partial\phi}{\partial t}+\left|\nabla\phi\right|^2 \tag{22.4.4}$$

we have

$$\frac{\mathrm{d}\phi}{\mathrm{d}t}=-p_s-y+\frac{1}{2}\left|\nabla\phi\right|^2-\frac{2}{Re}\frac{\partial^2\phi}{\partial n^2}-\frac{\kappa}{We} \tag{22.4.5}$$

and

$$\frac{\mathrm{d}x}{\mathrm{d}t}=\frac{\partial\phi}{\partial x},\quad\frac{\mathrm{d}y}{\mathrm{d}t}=\frac{\partial\phi}{\partial y} \tag{22.4.6}$$

on the free surface $y=y_s(x,t)$, where $x\in\tilde{C}(t)$ is periodic with period 2π. The free surface $\tilde{C}(t)$ is mapped into a closed contour $C(t)$

$$r\mathrm{e}^{\mathrm{i}\theta}=\zeta=\mathrm{e}^{-\mathrm{i}z},\quad z=x+\mathrm{i}y \tag{22.4.7}$$

where ζ is a new complex variable, analytic and single-valued everywhere inside the contour C which corresponds to the fluid surface, (r,θ) are polar coordinates in the ζ-plane, and

$$r=\mathrm{e}^y,\quad y=\ln r,\quad\theta=-x,\quad x=-\theta. \tag{22.4.8}$$

All points at infinite depth in the (x,y) plane are into the origin O in the ζ-plane.

$$\chi=\phi+\mathrm{i}\psi \tag{22.4.9}$$

is the complex potential in the z-plane and

$$\frac{\mathrm{d}\chi}{\mathrm{d}z}=u-\mathrm{i}v,\quad\left|\frac{\mathrm{d}\chi}{\mathrm{d}z}\right|^2=u^2+v^2 \tag{22.4.10}$$

is the complex velocity. At the free surface

$$\begin{aligned}\frac{\mathrm{d}r}{\mathrm{d}t}&=\mathrm{e}^y\frac{\mathrm{d}y}{\mathrm{d}t}=r\frac{\partial\phi}{\partial y}=r^2\frac{\partial\psi}{\partial r},\\\frac{\mathrm{d}\theta}{\mathrm{d}t}&=-\frac{\mathrm{d}x}{\mathrm{d}t}=-\frac{\partial\phi}{\partial x}=\frac{\partial\psi}{\partial\theta},\end{aligned} \tag{22.4.11}$$

$$\frac{\mathrm{d}\phi}{\mathrm{d}t}=-p_s-\ln r+\frac{1}{2}\left[\left(r\frac{\partial\phi}{\partial r}\right)^2+\left(\frac{\partial\phi}{\partial\theta}\right)^2\right]-\frac{2}{Re}\frac{\partial^2\phi}{\partial n^2}-\frac{\kappa}{We} \tag{22.4.12}$$

LHC solve a Dirichlet problem for ϕ. They say that

Suppose that at some initial instant $t=t_0$ we are given the velocity potential ϕ throughout the fluid, and hence the value of ϕ and its derivatives both inside and on the contour $C(t_0)$. Let (r,θ) denote the (Lagrangian) coordinates of a particle on $C(t_0)$. Then equations (22.4.11) will determine the position of the same particle a short time $\mathrm{d}t$ later. Similarly, (22.4.12) will determine the value of $\phi(t_0+\mathrm{d}t)$ on the new contour $C(t_0+\mathrm{d}t)$. By considering adjacent particles, and differentiating along the surface we can then obtain the *tangential* component of velocity $\partial\phi/\partial s$. But this does not immediately determine the normal component $\partial\phi/\partial n$, which is also needed for the step afterwards.

The problem of determining the normal component of velocity at the boundary is equivalent to the *Dirichlet problem* of finding the normal gradient of a function ϕ whose values are given on a closed contour C, and which is harmonic ($\nabla^2\phi = 0$) everywhere inside C. We may formulate the problem as an integral equation as follows.

Let (s, n) be tangential and normal coordinates at a typical point P on the boundary (see figure 22.3), and let (R, α) be the polar coordinates of P with respect to an arbitrary point $Q(r_0, \theta_0)$ in the interior. Let

$$G = \frac{1}{2\pi} \ln R \tag{22.4.13}$$

so $\nabla^2 S = 0$. Then, by Green's theorem we have

$$\phi(r_0, \theta_0) = \int_C \left[\phi \frac{\partial G}{\partial n} - \frac{\partial \phi}{\partial n} G\right] \mathrm{d}s = \frac{1}{2\pi} \int_C \left[\phi \frac{\partial \alpha}{\partial s} - \frac{\partial \phi}{\partial n} \ln R\right] \mathrm{d}s. \tag{22.4.14}$$

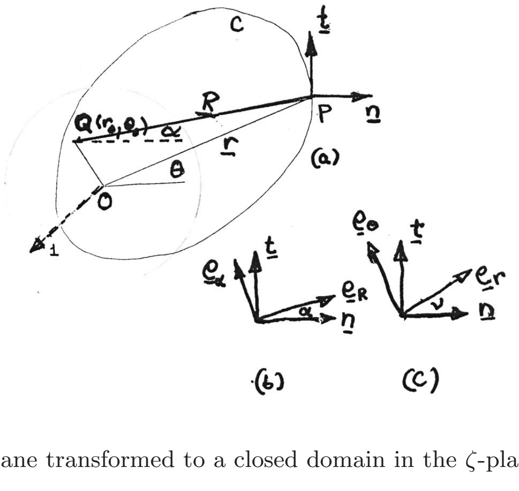

Fig. 22.3. One wavelenth in the z-plane transformed to a closed domain in the ζ-plane by (22.4.5). Parameters relating boundary points P to field points Q.

where, using Fig. 22.3 (a) and (b), we have

$$\begin{aligned}\frac{\partial G}{\partial n} &= \boldsymbol{n}\cdot\nabla G = \frac{1}{2\pi}\frac{n_i}{R}\frac{\partial R}{\partial x_i} = \frac{n_i R_i}{2\pi R^2} = \frac{\boldsymbol{n}\cdot\boldsymbol{e}_R}{2\pi R} = \frac{\boldsymbol{t}\cdot\boldsymbol{e}_\alpha}{2\pi R}\\ &= \frac{1}{2\pi R}\left(\boldsymbol{e}_R\frac{\partial R}{\partial s} + \boldsymbol{e}_\alpha R\frac{\partial \alpha}{\partial s}\right)\cdot\boldsymbol{e}_\alpha = \frac{1}{2\pi}\frac{\partial \alpha}{\partial s}.\end{aligned} \tag{22.4.15}$$

In the limit of $Q(r_0,\theta_0)$ approaching C, we find

$$\int_C \phi \mathrm{d}\alpha = \pi\phi_0 + \mathrm{P}\int_C \phi\mathrm{d}\alpha, \tag{22.4.16}$$

where the principal value integral is denoted by P and C is assumed to be smooth at Q. Using (22.4.16), expression (22.4.14) can be rearranged to obtain the boundary integral relation

$$\int_C \frac{\partial \phi}{\partial n}\ln R\mathrm{d}s = \mathrm{P}\int_C \phi\mathrm{d}\alpha - \pi\phi_0. \tag{22.4.17}$$

In this expression, R and α are determined by the curve C and the values of ϕ are given on C in the Dirichlet problem. Therefore, (22.4.17)) is an integral equation for $\partial\phi/\partial n$ with a logarithmic singularity.

It remains to express the time-derivatives of r, θ and ϕ in terms of the tangential and normal derivatives of ϕ.

First, we show that

$$\left.\begin{aligned}\frac{\partial \phi}{\partial r} &= \sin\nu\frac{\partial \phi}{\partial s} + \cos\nu\frac{\partial \phi}{\partial n},\\ \frac{1}{r}\frac{\partial \phi}{\partial \theta} &= \cos\nu\frac{\partial \phi}{\partial s} - \sin\nu\frac{\partial \phi}{\partial n}.\end{aligned}\right\} \tag{22.4.18}$$

This follows from

$$\nabla\phi = \boldsymbol{e}_r\frac{\partial \phi}{\partial r} + \frac{\boldsymbol{e}_\theta}{r}\frac{\partial \phi}{\partial \theta} = \boldsymbol{t}\frac{\partial \phi}{\partial s} + \boldsymbol{n}\frac{\partial \phi}{\partial n} \tag{22.4.19}$$

using Fig. 22.3 (c). Noting next that

$$\boldsymbol{t} = \frac{\partial \boldsymbol{r}}{\partial s} = \boldsymbol{e}_r\frac{\partial r}{\partial s} + \boldsymbol{e}_\theta r\frac{\partial \theta}{\partial s} = \boldsymbol{e}_r\sin\nu + \boldsymbol{e}_\theta\cos\nu, \tag{22.4.20}$$

we find that

$$\left.\begin{aligned}\sin\nu &= \frac{\partial r}{\partial s},\\ \cos\nu &= r\frac{\partial \theta}{\partial s}.\end{aligned}\right\} \tag{22.4.21}$$

Hence

$$\frac{\mathrm{d}r}{\mathrm{d}t} = r\frac{\partial \phi}{\partial r} = r^2\frac{\partial r}{\partial s}\frac{\partial \phi}{\partial s} + r^3\frac{\partial \theta}{\partial s}\frac{\partial \phi}{\partial n}, \tag{22.4.22}$$

$$\frac{\mathrm{d}\theta}{\mathrm{d}t} = \frac{\partial \phi}{\partial \theta} = r^2\frac{\partial \theta}{\partial s}\frac{\partial \phi}{\partial s} - r\frac{\partial r}{\partial s}\frac{\partial \phi}{\partial n}, \tag{22.4.23}$$

$$\frac{\mathrm{d}\phi}{\mathrm{d}t} = -p_s - \ln r + \frac{1}{2}r^2\left[\left(\frac{\partial \phi}{\partial s}\right)^2 + \left(\frac{\partial \phi}{\partial n}\right)^2\right] - \frac{2}{Re}\frac{\partial^2 \phi}{\partial n^2} - \frac{\kappa}{We}. \tag{22.4.24}$$

LHC did not compute viscous or surface tension terms. The viscous term can be reduced to a computable form in which $\partial^2\phi/\partial n^2$ is replaced with computable terms

$$\frac{\partial^2 \phi}{\partial n^2} = -\kappa\frac{\partial \phi}{\partial n} - \frac{\partial^2 \phi}{\partial s^2} \tag{22.4.25}$$

using Laplace's equation in (r,s) coordinates.

It remains then to compute the curvature $\kappa = 1/r$. This is very easy to do numerically from the three point algorithm of neighboring points on s. To compute a computable formula for κ we first note that

$$\dot{\boldsymbol{e}}_r = \boldsymbol{e}_\theta \frac{\partial \theta}{\partial s}, \quad \dot{\boldsymbol{e}}_\theta = -\boldsymbol{e}_r \frac{\partial \theta}{\partial s}, \tag{22.4.26}$$

$$\frac{\mathrm{d}\boldsymbol{t}}{\mathrm{d}s} = \dot{\boldsymbol{e}}_r \frac{\partial r}{\partial s} + \dot{\boldsymbol{e}}_\theta r \frac{\partial \theta}{\partial s} + \boldsymbol{e}_r \frac{\partial^2 r}{\partial s^2} + \boldsymbol{e}_\theta \left[\frac{\partial r}{\partial s} \frac{\partial \theta}{\partial s} + r \frac{\partial^2 \theta}{\partial s^2} \right] \tag{22.4.27}$$

$$= \boldsymbol{e}_r \left[\frac{\partial^2 r}{\partial s^2} - r \left(\frac{\partial \theta}{\partial s} \right)^2 \right] + \boldsymbol{e}_\theta \left[2 \frac{\partial r}{\partial s} \frac{\partial \theta}{\partial s} + r \frac{\partial^2 \theta}{\partial s^2} \right]. \tag{22.4.28}$$

We have

$$\kappa = \boldsymbol{n} \cdot \frac{\mathrm{d}\boldsymbol{t}}{\mathrm{d}s} = -\left(\frac{\partial r}{\partial s} \right)^2 \frac{\partial \theta}{\partial s} + r \frac{\partial \theta}{\partial s} \frac{\partial^2 r}{\partial s^2} - r \frac{\partial r}{\partial s} \frac{\partial^2 \theta}{\partial s^2} - \frac{\partial \theta}{\partial s} \tag{22.4.29}$$

where we have used (see Fig. 22.3(c))

$$\boldsymbol{n} \cdot \boldsymbol{e}_r = \cos \nu = r \frac{\partial \theta}{\partial s}, \quad \boldsymbol{n} \cdot \boldsymbol{e}_\theta = -\sin \nu = -\frac{\partial r}{\partial s} \tag{22.4.30}$$

and

$$1 = \boldsymbol{t} \cdot \boldsymbol{t} = \left(\frac{\partial r}{\partial s} \right)^2 + \left(r \frac{\partial \theta}{\partial s} \right)^2. \tag{22.4.31}$$

Equations (22.4.22-22.4.25) and (22.4.29) together with initial conditions, are a basis for computing the effects of viscosity and surface tension on the steep waves computed by LHC. This calculation will be carried out in the futute.

Appendix 1

Equations of motion and strain rates for rotational and irrotational flow in cartesian, cylindrical and spherical coordinates

A1.1 Cartesian coordinates

In Cartesian coordinates $(\xi_1, \xi_2, \xi_3) = (x, y, z)$ with unit vectors $\boldsymbol{e}_x$, $\boldsymbol{e}_y$, $\boldsymbol{e}_z$, equations for $\boldsymbol{u} = (u_1, u_2, u_3) = (u_x, u_y, u_z)$ are given as follows,

$$\boldsymbol{n} \cdot \nabla \boldsymbol{u} = \boldsymbol{e}_x \left(\boldsymbol{n} \cdot \nabla\right) u_x + \boldsymbol{e}_y \left(\boldsymbol{n} \cdot \nabla\right) u_y + \boldsymbol{e}_z \left(\boldsymbol{n} \cdot \nabla\right) u_z \tag{A1.1.1}$$

$$\nabla \cdot \boldsymbol{u} = \frac{\partial u_x}{\partial x} + \frac{\partial u_y}{\partial y} + \frac{\partial u_z}{\partial z}, \tag{A1.1.2}$$

$$\begin{aligned} \nabla \times \boldsymbol{u} &= \begin{vmatrix} \boldsymbol{e}_x & \boldsymbol{e}_y & \boldsymbol{e}_z \\ \dfrac{\partial}{\partial x} & \dfrac{\partial}{\partial y} & \dfrac{\partial}{\partial z} \\ u_x & u_y & u_z \end{vmatrix} \\ &= \left(\frac{\partial u_z}{\partial y} - \frac{\partial u_y}{\partial z}\right) \boldsymbol{e}_x + \left(\frac{\partial u_x}{\partial z} - \frac{\partial u_z}{\partial x}\right) \boldsymbol{e}_y + \left(\frac{\partial u_y}{\partial x} - \frac{\partial u_x}{\partial y}\right) \boldsymbol{e}_z. \end{aligned} \tag{A1.1.3}$$

$$\nabla^2 \boldsymbol{u} = \boldsymbol{e}_x \nabla^2 u_x + \boldsymbol{e}_y \nabla^2 u_y + \boldsymbol{e}_z \nabla^2 u_z = \boldsymbol{e}_x \Delta u_x + \boldsymbol{e}_y \Delta u_y + \boldsymbol{e}_z \Delta u_z \tag{A1.1.4}$$

with

$$\nabla^2 = \Delta = \frac{\partial^2}{\partial x^2} + \frac{\partial^2}{\partial y^2} + \frac{\partial^2}{\partial z^2}. \tag{A1.1.5}$$

$$T_{ij} = -p\delta_{ij} + S_{ij}, \quad S_{ij} = 2\mu e_{ij} \tag{A1.1.6}$$

$$L_{ij} = \frac{\partial u_i}{\partial x_j}, \quad L_{ij} = \frac{1}{2}\left(\frac{\partial u_i}{\partial x_j} + \frac{\partial u_j}{\partial x_i}\right) + \frac{1}{2}\left(\frac{\partial u_i}{\partial x_j} - \frac{\partial u_j}{\partial x_i}\right) = e_{ij} + \Omega_{ij} \tag{A1.1.7}$$

$$e_{ij} = \frac{1}{2}\left(L_{ij} + L_{ji}\right), \quad e_{ij} = e_{ji}, \quad \Omega_{ij} = \left(\frac{1}{2} L_{ij} - L_{ji}\right), \quad \Omega_{ij} = -\Omega_{ji} \tag{A1.1.8}$$

$$\begin{gathered} e_{xx} = \frac{\partial u_x}{\partial x}, \quad e_{yy} = \frac{\partial u_y}{\partial y}, \quad e_{zz} = \frac{\partial u_z}{\partial z}, \\ e_{xy} = \frac{1}{2}\left(\frac{\partial u_x}{\partial y} + \frac{\partial u_y}{\partial x}\right), \quad e_{yz} = \frac{1}{2}\left(\frac{\partial u_y}{\partial z} + \frac{\partial u_z}{\partial y}\right), \quad e_{zx} = \frac{1}{2}\left(\frac{\partial u_z}{\partial x} + \frac{\partial u_x}{\partial z}\right), \end{gathered} \tag{A1.1.9}$$

$$\frac{\partial u_x}{\partial t} + \boldsymbol{u} \cdot \nabla u_x = -\frac{1}{\rho}\frac{\partial p}{\partial x} + \nu \Delta u_x, \tag{A1.1.10}$$

$$\frac{\partial u_y}{\partial t} + \boldsymbol{u} \cdot \nabla u_y = -\frac{1}{\rho}\frac{\partial p}{\partial y} + \nu \Delta u_y, \tag{A1.1.11}$$

$$\frac{\partial u_z}{\partial t} + \boldsymbol{u} \cdot \nabla u_z = -\frac{1}{\rho}\frac{\partial p}{\partial z} + \nu \Delta u_z, \tag{A1.1.12}$$

For $\boldsymbol{u} = \nabla\phi$, equations for ϕ are given as follows

$$\nabla\phi = \boldsymbol{e}_x \frac{\partial\phi}{\partial x} + \boldsymbol{e}_y \frac{\partial\phi}{\partial y} + \boldsymbol{e}_z \frac{\partial\phi}{\partial z}, \tag{A1.1.13}$$

$$\nabla^2\phi = \Delta\phi = \frac{\partial^2\phi}{\partial x^2} + \frac{\partial^2\phi}{\partial y^2} + \frac{\partial^2\phi}{\partial z^2} \tag{A1.1.14}$$

$$e_{ij} = \frac{1}{2}\left(L_{ij} + L_{ji}\right) = \frac{\partial^2\phi}{\partial x_i \partial x_j}, \quad e_{ij} = e_{ji}, \tag{A1.1.15}$$

$$\begin{aligned} e_{xx} = \frac{\partial^2\phi}{\partial x^2}, \quad e_{yy} = \frac{\partial^2\phi}{\partial y^2}, \quad e_{zz} = \frac{\partial^2\phi}{\partial z^2}, \\ e_{xy} = \frac{\partial^2\phi}{\partial x \partial y}, \quad e_{yz} = \frac{\partial^2\phi}{\partial y \partial z}, \quad e_{zx} = \frac{\partial^2\phi}{\partial z \partial x}. \end{aligned} \tag{A1.1.16}$$

$$\frac{\partial\phi}{\partial t} + \frac{1}{2}\left|\nabla\phi\right|^2 + \frac{p}{\rho} = \frac{\partial\phi}{\partial t} + \frac{1}{2}\left[\left(\frac{\partial\phi}{\partial x}\right)^2 + \left(\frac{\partial\phi}{\partial y}\right)^2 + \left(\frac{\partial\phi}{\partial z}\right)^2\right] + \frac{p}{\rho} = f(t) \tag{A1.1.17}$$

A1.2 Cylindrical coordinates

In cylindrical coordinates $(\xi_1, \xi_2, \xi_3) = (r, \theta, z)$ with unit vectors $\boldsymbol{e}_r$, $\boldsymbol{e}_\theta$, $\boldsymbol{e}_z$, equations for $\boldsymbol{u} = (u_1, u_2, u_3) = (u_r, u_\theta, u_z)$ are given as follows,

$$\frac{\partial \boldsymbol{e}_r}{\partial\theta} = \boldsymbol{e}_\theta, \quad \frac{\partial \boldsymbol{e}_\theta}{\partial\theta} = -\boldsymbol{e}_r, \quad \frac{\partial \boldsymbol{e}_\theta}{\partial\theta} = 0, \tag{A1.2.1}$$

$$\begin{aligned} \boldsymbol{n}\cdot\nabla\boldsymbol{u} \quad = \quad & \boldsymbol{e}_r\left[\left(\boldsymbol{n}\cdot\nabla\right)u_r - \frac{n_\theta}{r}u_\theta\right] + \boldsymbol{e}_\theta\left[\left(\boldsymbol{n}\cdot\nabla\right)u_\theta + \frac{n_\theta}{r}u_r\right] \\ & + \boldsymbol{e}_\varphi\left(\boldsymbol{n}\cdot\nabla\right)u_\varphi \end{aligned} \tag{A1.2.2}$$

$$\nabla\cdot\boldsymbol{u} = \frac{1}{r}\frac{\partial}{\partial r}\left(r u_r\right) + \frac{1}{r}\frac{\partial u_\theta}{\partial\theta} + \frac{\partial u_z}{\partial z}, \tag{A1.2.3}$$

$$\nabla\times\boldsymbol{u} = \boldsymbol{e}_r\left[\frac{1}{r}\frac{\partial u_z}{\partial\theta} - \frac{\partial u_\theta}{\partial z}\right] + \boldsymbol{e}_\theta\left[\frac{\partial u_r}{\partial z} - \frac{\partial u_z}{\partial r}\right] + \boldsymbol{e}_z\left[\frac{1}{r}\frac{\partial\left(r u_\theta\right)}{\partial r} - \frac{1}{r}\frac{\partial u_r}{\partial\theta}\right] \tag{A1.2.4}$$

$$\nabla^2\boldsymbol{u} = \boldsymbol{e}_r\left[\Delta u_r - \frac{u_r}{r^2} - \frac{2}{r^2}\frac{\partial u_\theta}{\partial\theta}\right] + \boldsymbol{e}_\theta\left[\Delta u_\theta + \frac{2}{r^2}\frac{\partial u_r}{\partial\theta} - \frac{u_\theta}{r^2}\right] + \boldsymbol{e}_z\Delta u_z \tag{A1.2.5}$$

with

$$\nabla^2 = \Delta = \frac{\partial^2}{\partial r^2} + \frac{1}{r}\frac{\partial}{\partial r} + \frac{1}{r^2}\frac{\partial^2}{\partial\theta^2} + \frac{\partial^2}{\partial z^2}. \tag{A1.2.6}$$

$$T_{ij} = -p\delta_{ij} + 2\mu e_{ij} \tag{A1.2.7}$$

$$e_{rr} = \frac{\partial u_r}{\partial r}, \quad e_{\theta\theta} = \frac{1}{r}\frac{\partial u_\theta}{\partial\theta} + \frac{u_r}{r}, \quad e_{zz} = \frac{\partial u_z}{\partial z}, \tag{A1.2.8}$$

$$e_{r\theta} = \frac{r}{2}\frac{\partial}{\partial r}\left(\frac{u_\theta}{r}\right) + \frac{1}{2r}\frac{\partial u_r}{\partial\theta}, \quad e_{\theta z} = \frac{1}{2r}\frac{\partial u_z}{\partial\theta} + \frac{1}{2}\frac{\partial u_\theta}{\partial z}, \quad e_{zr} = \frac{1}{2}\frac{\partial u_r}{\partial z} + \frac{1}{2}\frac{\partial u_z}{\partial r} \tag{A1.2.9}$$

$$\frac{\partial u_r}{\partial t} + \boldsymbol{u}\cdot\nabla u_r - \frac{u_\theta^2}{r} = -\frac{1}{\rho}\frac{\partial p}{\partial r} + \nu\left[\Delta u_r - \frac{u_r}{r^2} - \frac{2}{r^2}\frac{\partial u_\theta}{\partial\theta}\right], \tag{A1.2.10}$$

$$\frac{\partial u_\theta}{\partial t} + \boldsymbol{u}\cdot\nabla u_\theta + \frac{u_r u_\theta}{r} = -\frac{1}{\rho r}\frac{\partial p}{\partial\theta} + \nu\left[\Delta u_\theta + \frac{2}{r^2}\frac{\partial u_r}{\partial\theta} - \frac{u_\theta}{r^2}\right], \tag{A1.2.11}$$

$$\frac{\partial u_z}{\partial t} + \boldsymbol{u}\cdot\nabla u_z = -\frac{1}{\rho}\frac{\partial p}{\partial z} + \nu\Delta u_z. \tag{A1.2.12}$$

For $\boldsymbol{u} = \nabla\phi$, equations for ϕ are given as follows,

$$\nabla\phi = \boldsymbol{e}_r \frac{\partial \phi}{\partial r} + \frac{\boldsymbol{e}_\theta}{r} \frac{\partial \phi}{\partial \theta} + \boldsymbol{e}_z \frac{\partial \phi}{\partial z} \tag{A1.2.13}$$

$$\nabla^2 \phi = \Delta\phi = \frac{1}{r} \frac{\partial}{\partial r} \left(r \frac{\partial \phi}{\partial r} \right) + \frac{1}{r^2} \frac{\partial \phi}{\partial \theta} + \frac{\partial^2 \phi}{\partial z^2} \tag{A1.2.14}$$

$$e_{rr} = \frac{\partial^2 \phi}{\partial r^2}, \quad e_{\theta\theta} = \frac{1}{r^2} \frac{\partial^2 \phi}{\partial \theta^2} + \frac{1}{r} \frac{\partial \phi}{\partial r}, \quad e_{zz} = \frac{\partial^2 \phi}{\partial z^2}, \tag{A1.2.15}$$

$$e_{r\theta} = \frac{1}{r} \frac{\partial^2 \phi}{\partial r \partial \theta} - \frac{1}{r^2} \frac{\partial \phi}{\partial \theta}, \quad e_{\theta z} = \frac{1}{r} \frac{\partial^2 \phi}{\partial z \partial \theta}, \quad e_{zr} = \frac{\partial^2 \phi}{\partial z \partial r} \tag{A1.2.16}$$

$$\frac{\partial \phi}{\partial t} + \frac{1}{2} |\nabla\phi|^2 + \frac{p}{\rho} = \frac{\partial \phi}{\partial t} + \frac{1}{2} \left[\left(\frac{\partial \phi}{\partial r} \right)^2 + \left(\frac{1}{r} \frac{\partial \phi}{\partial \theta} \right)^2 + \left(\frac{\partial \phi}{\partial z} \right)^2 \right] + \frac{p}{\rho} = f(t) \tag{A1.2.17}$$

A1.3 Polar Spherical coordinates

In polar spherical coordinates $(\xi_1, \xi_2, \xi_3) = (r, \theta, \varphi)$ with unit vectors $\boldsymbol{e}_r$, $\boldsymbol{e}_\theta$, $\boldsymbol{e}_\varphi$, equations for $\boldsymbol{u} = (u_1, u_2, u_3) = (u_r, u_\theta, u_\varphi)$ are given as follows,

$$\frac{\partial \boldsymbol{e}_r}{\partial r} = 0, \quad \frac{\partial \boldsymbol{e}_r}{\partial \theta} = \boldsymbol{e}_\theta, \quad \frac{\partial \boldsymbol{e}_r}{\partial \varphi} = \boldsymbol{e}_\varphi \sin\theta, \tag{A1.3.1}$$

$$\frac{\partial \boldsymbol{e}_\theta}{\partial r} = 0, \quad \frac{\partial \boldsymbol{e}_\theta}{\partial \theta} = -\boldsymbol{e}_r, \quad \frac{\partial \boldsymbol{e}_\theta}{\partial \varphi} = \boldsymbol{e}_\varphi \cos\theta, \tag{A1.3.2}$$

$$\frac{\partial \boldsymbol{e}_\varphi}{\partial r} = 0, \quad \frac{\partial \boldsymbol{e}_\varphi}{\partial \theta} = 0, \quad \frac{\partial \boldsymbol{e}_\varphi}{\partial \varphi} = -\boldsymbol{e}_r \sin\theta - \boldsymbol{e}_\theta \cos\theta \tag{A1.3.3}$$

$$\begin{aligned} \boldsymbol{n} \cdot \nabla \boldsymbol{u} \;=\; & \boldsymbol{e}_r \left[(\boldsymbol{n} \cdot \nabla) u_r - \frac{n_\theta}{r} u_\theta - \frac{n_\varphi}{r} u_\varphi \right] + \boldsymbol{e}_\theta \left[(\boldsymbol{n} \cdot \nabla) u_\theta + \frac{n_\theta}{r} u_r - \frac{n_\varphi}{r} u_\varphi \cot\theta \right] \\ & + \boldsymbol{e}_\varphi \left[(\boldsymbol{n} \cdot \nabla) u_\varphi + \frac{n_\varphi}{r} u_r + \frac{n_\varphi}{r} u_\theta \cot\theta \right] \end{aligned} \tag{A1.3.4}$$

$$\nabla \cdot \boldsymbol{u} = \frac{1}{r^2} \frac{\partial}{\partial r} \left(r^2 u_r \right) + \frac{1}{r \sin\theta} \frac{\partial}{\partial \theta} \left(u_\theta \sin\theta \right) + \frac{1}{r \sin\theta} \frac{\partial u_\varphi}{\partial \varphi}, \tag{A1.3.5}$$

$$\begin{aligned} \nabla \times \boldsymbol{u} \;=\; & \boldsymbol{e}_r \frac{1}{r \sin\theta} \left[\frac{\partial}{\partial \theta} (\sin\theta u_\varphi) - \frac{\partial u_\theta}{\partial \varphi} \right] - \frac{1}{r \sin\theta} \boldsymbol{e}_\theta \left[\sin\theta \frac{\partial (r u_\varphi)}{\partial r} - \frac{\partial u_r}{\partial \varphi} \right] \\ & + \frac{1}{r} \boldsymbol{e}_\varphi \left[\frac{\partial (r u_\theta)}{\partial r} - \frac{\partial u_r}{\partial \theta} \right] \end{aligned} \tag{A1.3.6}$$

$$\begin{aligned} \nabla^2 \boldsymbol{u} \;=\; & \boldsymbol{e}_r \left[\Delta u_r - 2\frac{u_r}{r^2} - \frac{2}{r^2} \frac{\partial u_\theta}{\partial \theta} - 2\frac{u_\theta}{r^2} \cot\theta - \frac{2}{r^2 \sin\theta} \frac{\partial u_\varphi}{\partial \varphi} \right] \\ & + \boldsymbol{e}_\theta \left[\Delta u_\theta + \frac{2}{r^2} \frac{\partial u_r}{\partial \theta} - \frac{u_\theta}{r^2 \sin^2\theta} - \frac{2\cos\theta}{r^2 \sin^2\theta} \frac{\partial u_\varphi}{\partial \varphi} \right] \\ & + \boldsymbol{e}_\varphi \left[\Delta u_\varphi + \frac{2}{r^2 \sin\theta} \frac{\partial u_r}{\partial \varphi} + \frac{2\cos\theta}{r^2 \sin^2\theta} \frac{\partial u_\theta}{\partial \varphi} - \frac{u_\varphi}{r^2 \sin^2\theta} \right] \end{aligned} \tag{A1.3.7}$$

with

$$\nabla^2 = \Delta = \frac{\partial^2}{\partial r^2} + \frac{2}{r} \frac{\partial}{\partial r} + \frac{1}{r^2} \frac{\partial^2}{\partial \theta^2} + \frac{1}{r^2} \cot\theta \frac{\partial}{\partial \theta} + \frac{1}{r^2 \sin^2\theta} \frac{\partial^2}{\partial \varphi^2}. \tag{A1.3.8}$$

$$T_{ij} = -p\delta_{ij} + 2\mu e_{ij} \tag{A1.3.9}$$

$$e_{rr} = \frac{\partial u_r}{\partial r}, \quad e_{\theta\theta} = \frac{1}{r}\frac{\partial u_\theta}{\partial \theta} + \frac{u_r}{r}, \quad e_{\varphi\varphi} = \frac{1}{r\sin\theta}\frac{\partial u_\varphi}{\partial \varphi} + \frac{u_r}{r} + \frac{u_\theta}{r}\cot\theta, \tag{A1.3.10}$$

$$e_{r\theta} = \frac{r}{2}\frac{\partial}{\partial r}\left(\frac{u_\theta}{r}\right) + \frac{1}{2r}\frac{\partial u_r}{\partial \theta}, \quad e_{\theta\varphi} = \frac{\sin\theta}{2r}\frac{\partial}{\partial \theta}\left(\frac{u_\varphi}{\sin\theta}\right) + \frac{1}{2r\sin\theta}\frac{\partial u_\theta}{\partial \varphi}, \quad e_{\varphi r} = \frac{1}{2r\sin\theta}\frac{\partial u_r}{\partial \varphi} + \frac{r}{2}\frac{\partial}{\partial r}\left(\frac{u_\varphi}{r}\right)$$

$$\begin{aligned}
\frac{\partial u_r}{\partial t} + \boldsymbol{u}\cdot\nabla u_r - \frac{u_\theta^2}{r} - \frac{u_\varphi^2}{r} &= -\frac{1}{\rho}\frac{\partial p}{\partial r} \\
&\quad + \nu\left[\Delta u_r - 2\frac{u_r}{r^2} - \frac{2}{r^2}\frac{\partial u_\theta}{\partial \theta} - 2\frac{u_\theta}{r^2}\cot\theta - \frac{2}{r^2\sin\theta}\frac{\partial u_\varphi}{\partial \varphi}\right], \qquad \text{(A1.3.11)} \\
\frac{\partial u_\theta}{\partial t} + \boldsymbol{u}\cdot\nabla u_\theta + \frac{u_r u_\theta}{r} - \frac{u_\varphi^2}{r}\cot\theta &= -\frac{1}{\rho r}\frac{\partial p}{\partial \theta} \\
&\quad + \nu\left[\Delta u_\theta + \frac{2}{r^2}\frac{\partial u_r}{\partial \theta} - \frac{u_\theta}{r^2\sin^2\theta} - \frac{2\cos\theta}{r^2\sin^2\theta}\frac{\partial u_\varphi}{\partial \varphi}\right], \qquad \text{(A1.3.12)} \\
\frac{\partial u_\varphi}{\partial t} + \boldsymbol{u}\cdot\nabla u_\varphi + \frac{u_\varphi u_r}{r} + \frac{u_\theta u_\varphi}{r}\cot\theta &= -\frac{1}{\rho r\sin\theta}\frac{\partial p}{\partial \varphi} \\
&\quad + \nu\left[\Delta u_\varphi + \frac{2}{r^2\sin\theta}\frac{\partial u_r}{\partial \varphi} + \frac{2\cos\theta}{r^2\sin^2\theta}\frac{\partial u_\theta}{\partial \varphi} - \frac{u_\varphi}{r^2\sin^2\theta}\right] \qquad \text{(A1.3.13)}
\end{aligned}$$

For $\boldsymbol{u} = \nabla\phi$, equations for ϕ are given as follows

$$\nabla\phi = \boldsymbol{e}_r\frac{\partial \phi}{\partial r} + \frac{\boldsymbol{e}_\theta}{r}\frac{\partial \phi}{\partial \theta} + \frac{\boldsymbol{e}_\varphi}{r\sin\theta}\frac{\partial \phi}{\partial \varphi} \tag{A1.3.14}$$

$$\nabla^2\phi = \Delta\phi = \frac{1}{r^2}\frac{\partial}{\partial r}\left(r^2\frac{\partial \phi}{\partial r}\right) + \frac{1}{r^2\sin\theta}\frac{\partial}{\partial \theta}\left(\sin\theta\frac{\partial \phi}{\partial \theta}\right) + \frac{1}{r^2\sin^2\theta}\frac{\partial^2 \phi}{\partial \varphi^2} \tag{A1.3.15}$$

$$e_{rr} = \frac{\partial^2 \phi}{\partial r^2}, \quad e_{\theta\theta} = \frac{1}{r^2}\frac{\partial^2 \phi}{\partial \theta^2} + \frac{1}{r}\frac{\partial \phi}{\partial r}, \quad e_{\varphi\varphi} = \frac{1}{r^2\sin^2\theta}\frac{\partial^2 \phi}{\partial \varphi^2} + \frac{1}{r}\frac{\partial \phi}{\partial r} + \frac{1}{r^2}\frac{\partial \phi}{\partial \theta}\cot\theta, \tag{A1.3.16}$$

$$e_{r\theta} = \frac{1}{r}\frac{\partial^2 \phi}{\partial r\partial \theta} - \frac{1}{r^2}\frac{\partial \phi}{\partial \theta}, \quad e_{\theta\varphi} = \frac{1}{r^2\sin\theta}\left(\frac{\partial^2 \phi}{\partial \theta\partial \varphi} - \cot\theta\frac{\partial \phi}{\partial \varphi}\right), \quad e_{\varphi r} = \frac{1}{r\sin\theta}\left(\frac{\partial^2 \phi}{\partial r\partial \varphi} - \frac{1}{r}\frac{\partial \phi}{\partial \varphi}\right)$$

$$\frac{\partial \phi}{\partial t} + \frac{1}{2}\left|\nabla\phi\right|^2 + \frac{p}{\rho} = \frac{\partial \phi}{\partial t} + \frac{1}{2}\left[\left(\frac{\partial \phi}{\partial r}\right)^2 + \left(\frac{1}{r}\frac{\partial \phi}{\partial \theta}\right)^2 + \left(\frac{1}{r\sin\theta}\frac{\partial \phi}{\partial \varphi}\right)^2\right] + \frac{p}{\rho} = f(t) \tag{A1.3.17}$$

Appendix 2
Tests of BibTeX

Environment of LaTeX $2_\varepsilon$and BibTeX is given by documentclass=“book.cls”, usepackage=“natbib”, and bibliographystyle=“cu

We can find that “cupbook.bst” works well.

As in the other bst styles, the folowing four cases cannot be processed well:

```
@Article{Dyke62,
  author = {M. Van Dyke},
  title = {Higher approximations in boundary-layer theory. {P}art 1. {G}eneral analysis},
  year = {1962},
  journal = {J. Fluid Mech.},
  volume = {14},
  pages = {161--177}
}

@Article{Dyke69,
  author = {M. Van Dyke},
  title = {Higher-order boundary-layer theory},
  year = {1969},
  journal = {Annu. Rev. Fluid Mech.},
  volume = {1},
  pages = {265--292}
}

@inproceedings{KuhnBrennen93,
author={Y. Kuhn-de-Chizelle and C. E. Brennen},
year={1993},
title={Comparison of observed and calculated shapes of travellingcavitation bubbles},
booktitle={Proc. IUTAM Symp. on Bubble Dynamics and Interface Phenomena, Birmingham, UK.},
volume={},
pages={207--217}
}

@Article{KuhnCeccioBrennen95,
author={Y. Kuhn-de-Chizelle and S. L. Ceccio and C. E. Brennen},
year={1995},
title={Observation and scaling of travelling bubble cavitation},
journal={J. Fluid Mech.},
volume={293},
pages={99--126}
}
```

A2.1 Sample citation (1)

Ackeret (1952),

Aitken and Wilson (1993),

Andritsos and Hanratty (1987),

Andritsos et al. (1989),

Apfel (1970),

Arakeri and Acosta (1973),

Archer et al. (1997),

Ashmore et al. (2005),

Bair and Winer (1990),

Bair and Winer (1992),

Barnea (1991),

Barnea and Taitel (1993),

Barr (1926),

Batchelor (1967),

Batchelor (1987),

Batchelor and Gill (1962),

Benjamin and Feir (1967),

Benjamin and Ursell (1954),

Bergwerk (1959),

Bers (1975),

Bhaga and Weber (1981),

Billet (1985),

Bi and Zhao (2001),

Bird et al. (1987),

Blake and Gibson (1987),

Boulton-Stone et al. (1996),

Brabston and Keller (1975),

Brennen (1995),

Bretherton (1961),

Brenner et al. (1997),

Briggs (1950),

Briggs (1964),

Brodkey (1967),

Brown (1965),

Canot et al. (2003),

Cerda and Tirapegui (1998),

Chandrasekhar (1961),

Chang and Russel (1965),

Chang et al. (1999),

Charru and Hinch (2000),

Chaves et al. (1995),

Chawla (1975),

Chen and Li (1999),

Chen and Israelachvili (1991),

Chen (1974),

Chen et al. (2002),

Christiansen and Hixson (1957),

Crowley et al. (1992),

Crum (1982),

Currie (1974),

Davies (1950),

Davies and Taylor (1950),

Dias and Kharif (1999),

Dizés (1997),

Dollet et al. (2004),

Drazin and Reid (1981),

Dumitrescue (1943),

Dunne and Cassen (1954),

Dunne and Cassen (1956),

Dyke (1962),

Dyke (1969),

Ece et al. (1984),

Edwards and Fauve (1993),

Eggers (1997),

Eggers (1993),

Engel (1958),

Entov (1978),

Faeth (1996),

Farrell (2003),

Fisher (1948),

Fluent Inc. Lebanon, NH. (2003),

Foteinopoulou et al. (2004),

Franc and Michel (1985),

Francis (1951),

Funada and Joseph (2001),

Funada and Joseph (2002),

Funada and Joseph (2003),

Funada et al. (2004),

Funada et al. (2004),

Funada et al. (2005),

Funada et al. (2006),

Funada et al. (2005),

Funada et al. (2005),

Galdi et al. (2002),

Gibson (1913),

Glauert (1957),

Goldin et al. (1969),

Goldstein (1960),

Goren and Gottlieb (1982),

Grace and Harrison (1967),

Grace et al. (1978),

Haberman and Morton (1953),

Hamel (1917),

Hamel (1941),

Hanson and Domich (1956),

Hanson et al. (1963),

Harper and Moore (1968),

Harper (1972),

Harrison (1908),

Harvey et al. (1944),

Harvey et al. (944b),

Harvey et al. (1947),

Hattori (1935),

Hesla et al. (1993),

Hicks (1884),

Hiemenz (1911),

Hirahara and Kawahashi (1992),

Howarth (1953),

Hsiang and Faeth (1992),

Hu et al. (1990),

Huang et al. (1997),

Huerre (2000),

Huerre and Monkewitz (1985),

Hwang et al. (1996),

Johnson and Patel (1999),

Joseph (1976),

Joseph (1990),

Joseph and Saut (1990),

Joseph and Renardy (1991),

Joseph (1992),

Joseph (992b),

Joseph et al. (1993),

Joseph and Liao (1994b),

Joseph and Liao (1994a),

Joseph (1995),

Joseph (1996),

Joseph and Feng (1996),

Joseph et al. (1996),

Joseph (1998),

Joseph et al. (1999),

Joseph (2000),

Joseph et al. (2002),

Joseph (2003b),

Joseph (2003a),

Joseph and Wang (2004),

Joseph (2006b),

Joseph (2006b),

Kang and Leal (1988a),

Kang and Leal (1988b),

Kang et al. (1999),

Keller et al. (1973),

Keller and Miksis (1983),

Kitscha and Kocamustafaogullari (1989),

Knapp et al. (1970),

Knapp (1958),

Knapp et al. (2003),

Kordyban and Ranov (1970),

Kottke et al. (2003),

Kottke et al. (2005),

Krzeczkowski (1980),

de Chizelle and Brennen (1993),

Kuhl et al. (1994),

de Chizelle et al. (1995),

Kumar and Tuckerman (1994),

Kumar (2000),

Lagerstrom and Cole (1955),

Lamb (1932),

Landau and Lifshitz (1987),

Lane (1951),

Laoonual et al. (2001),

Leib and Goldstein (1986b),

Leib and Goldstein (1986a),

Levich (1949),

Li and Kelly (1992),

Lighthill (1963),

Lin (2003),

Lin and Hanratty (1986),

Lin and Lian (1989),

Liu (1995),

Liu and Brennen (1998),

Liu and Joseph (1993),

Liu et al. (1995),

Liu and Reitz (1997),

Lundgren and Mansour (1988),

Magnaudet et al. (1995),

Maslen (1963),

Magnaudet and Eames (2000),

Matta and Tytus (1982),

Matta et al. (1983),

Mata et al. (2002),

McKinley and Tripathi (2000),

Michele et al. (1977),

Middleman (1965),

Miksis et al. (1982),

Miles and Henderson (1990),

Miller and Scriven (1968),

Milne-Thomson (1968),

Mishima and Ishii (1980),

Mittal and Kumar (2003),

Moore (1957),

Moore (1959),

Moore (1963),

Nayfeh and Saric (1973),

Ortiz et al. (2004),

Padrino and Joseph (2006b),

Padrino et al. (2005),

Pan et al. (2001),

Panton (1984),

Papageriou (1995),

Park et al. (1995),

Pedley (1968),

Peregrine et al. (1990),

Pereira et al. (2001),

Perlin and Schultz (2000),

Petit and Noetinger (1988),

Pilch and Erdman (1987),

Plateau (1873),

Plesset (1949),

Plesset (1969),

Plesset and Prosperetti (1977),

Poritsky (1951),

Pouliquen et al. (1994),

Prandtl and Tietjens (1934),

Pretsch (1938),

Prosperetti (1976),

Prosperetti (1980),

Ranger and Nicholls (1969),

Pruppacher et al. (1970),

Rayleigh (1878),

Rayleigh (1879),

Rayleigh (1890),

Rayleigh (1892),

Rayleigh (1917),

Reinecke and McKay (1969),

Reinecke and Waldman (1970),

Reinecke and Waldman (1975),

Romberg (1967),

Roos and Willmarth (1971),

Rothert et al. (2001),

Ryskin and Leal (1984),

Schetz et al. (1980),

Schlichting (1960),

Schmid and Henningson (2001),

Scirocco et al. (2003),

Segur et al. (2005),

Sherman and Schetz (1971),

Simpkins and Bales (1972),

Singhal et al. (2002),

Sirakov et al. (2005),

Soteriou et al. (1995),

Spiegelberg et al. (1994b),

Stokes (1851),

Stokes (1880),

Stone (1994),

Strasberg (1959),

Tait (1890),

Taitel and Dukler (1976),

Taneda (1956),

Taylor (1949),

Taylor (1950),

Taylor and Acrivos (1964),

Theofanous et al. (2003),

Tomboulides (1993),

Tomotika (1935),

Varga et al. (2003),

Vaynblat et al. (2001),

Viana et al. (2003),

Viana et al. (2005),

Waldman et al. (1972),

Wallis (1969),

Wallis and Dobson (1973),

Walters and Davidson (1963),

Wang et al. (2004),

Wang and Joseph (2003),

Wang et al. (2005a),

Wang et al. (2005b),

Wang et al. (2005c),

Wang and Joseph (2006a),

Wang and Joseph (2006b),

Wang and Joseph (2006c),

Wang and Joseph (2006d),

Weber (1931),

Wegener and Parlange (1973),

White and Beardmore (1962),

White (2006),

Wierzba and Takayama (1988),

Wierzba (1990),

Wilcox et al. (1961),

Winer and Bair (1987),

Wu et al. (1987),

Yang (1992),

Yang and Leal (1991),

Young (1989),

Yoshida and Takayama (1990),

Zhou and Lin (1992),

Zierep (1984),

A2.2 addition on July 8

Baker et al. (1980),

Baker et al. (1982),

Baker et al. (1984),

Byatt-Smith and Longuet-Higgins (1976),

Chen and Steen (1997),

Day et al. (1998),

Longuet-Higgins and Cokelet (1976),

Meiron and Saffman (1983),

Miksis et al. (1981),

Oguz and Prosperetti (1989),

Oguz and Prosperetti (1993),

Oguz and Prosperetti (1990),

Pullin (1982),

Rodriguez-Rodriguez et al. (2006),

Verdon et al. (1982),

Wrobel (1993),

Davila and Vassilicos (2003),

Chen et al. (2006),

Vassilicos et al. (2005),

Yoo (1973),

Banerjee and Butterfield (1981),

Brebbia et al. (1984),

Georgescu et al. (2002),

Kellogg (1929),

Machane and Canot (1997),

Pozrikidis (1992),

Scardovelli and Zaleski (1999),

Tsai and Yue (1996),

Truesdell (1953),

Yeung (1982),

Padrino and Joseph (2006a),

A2.3 addition on August 4

Joseph (1973),

Joseph et al. (1992),

Schwartz (1974),

Sangani (1991),

Sangani and Didwania (1993),

Longuet-Higgins (1992),

Longuet-Higgins (1997),

Ruvinsky and Freidman (1985a),

Ruvinsky and Freidman (1985b),

Ruvinsky and Freidman (1987),

Ruvinsky et al. (1991),

Pedley (1967),

Ponstein (1959),

Lundgren and Mansour (1991),

Birkhoff (1954),

Binnie (1953),

Plesset (1954),

Spivak et al. (2002),

Lundgren and Joseph (2006),

Yariv and 2003 (2003),

Yariv and Brenner (2004),

Chorin (1973),

Chorin (1978),

Wrobel (2002),

Jaswon and Symm (1977),

Larson (1988),

A2.4 addition on August 10

Ciliberto and Gollub (1985),

Douady and Fauve (1988),

Feng and Sethna (1989),

Gu and Sethna (1987),

Miles (1967),

Miles (1984),

Ockendon and Ockendon (1973),

Rayleigh (1877),

Rayleigh (1883a),

Rayleigh (1883b),

Simonelli and Gollub (1989),

Higuera and Knobloch (2006),

Higuera et al. (2005),

Vega et al. (2001),

Jeffery (1915),

Homann (1936),

Kojo and Ueno (2006),

Taylor (1923),

Dabiri et al. (2006),

Funada et al. (2006),

Loiseleux et al. (1998),

Ashgriz and Mashayek (1995),

Shi et al. (1994),

Spiegelberg et al. (1994a),

Joseph (2006c),

References

Ackeret J. (1952). Über exakte lösungen der Stokes-Navier-Gleichungen inkompressibler Flüssigkeiten bei veränderten Grenzbedingungen. Z. Angew. Math. Phys. **3**, 259–271.

Aitken L. S., Wilson S. D. R. (1993). Rayleigh-Taylor instability in elastic liquids. J. Non-Newtonian Fluid Mech. **49**, 13–22.

Andritsos N., Hanratty T. J. (1987). Interfacial instabilities for horizontal gas-liquid flows in pipelines. Int. J. Multiphase Flow **13**, 583–603.

Andritsos N., Williams L., Hanratty T. J. (1989). Effect of liquid viscosity on the stratified-slug transition in horizontal pipe flow. Int. J. Multiphase Flow **15**, 877–892.

Apfel R. E. (1970). The role of impurities in cavitation-threshold determination. J. Acoust. Soc. Am. **48**, 1179–1186.

Arakeri V. H., Acosta A. J. (1973). Viscous effects in the inception of cavitation on axisymmetric bodies. J. Fluids Eng. **95**, 519–527.

Archer L. A., Ternet D., Larson R. G. (1997). 'Fracture' phenomena in shearing flow of viscous liquids. Rheol. Acta. **36**, 579–584.

Ashgriz N., Mashayek F. (1995). Temporal analysis of capillary jet breakup. J. Fluid Mech. **291**, 163–190.

Ashmore J., del Pino C., Mullin T. (2005). Cavitation in a lubrication flow between a moving sphere and a boundary. Phys. Rev. Lett. **94**, 124501.

Bair S., Winer W. O. (1990). The high shear stress rheology of liquid lubricants at pressure of 2 to 200 MPa. J. Tribol. **114**, 246–253.

Bair S., Winer W. O. (1992). The high pressure high shear stress rheology of liquid lubricants. J. Tribol. **114**, 1–13.

Baker G. R., Meiron D. I., Orszag S. A. (1980). Vortex simulations of the Rayleigh-Taylor instability. Phys. Fluids **23**, 1485–1490.

Baker G. R., Meiron D. I., Orszag S. A. (1982). Generalized vortex methods for free-surface flow problems. J. Fluid Mech. **123**, 477–501.

Baker G. R., Meiron D. I., Orszag S. A. (1984). Boundary integral methods for axisymmetric and three-dimensional Reyleigh-Taylor instability problems. Physica **12 D**, 19–31.

Banerjee P. K., Butterfield R. (1981). Boundary Element Methods in Engineering Science. McGraw-Hill, Inc.

Barnea D. (1991). On the effect of viscosity on stability of stratified gas-liquid flow — application to flow pattern transition at various pipe inclinations. Chem. Engng. Sci. **46**, 2123–2131.

Barnea D., Taitel Y. (1993). Kelvin-Helmholtz stability criteria for stratified flow: viscous versus non-viscous (inviscid) approaches. Int. J. Multiphase Flow **19**, 639–649.

Barr G. (1926). The air bubble viscometer. Phil. Mag. **Series 7**, 395.

Batchelor G. K. (1967). An Introduction to Fluid Dynamics. Cambridge University Press.

Batchelor G. K. (1987). The stability of a large gas bubble rising through liquid. J. Fluid Mech **184**, 399–422.

Batchelor G. K., Gill A. E. (1962). Analysis of the stability of axisymmetric jets. J. Fluid Mech. **14**, 529–551.

Benjamin T. B., Feir J. E. (1967). The disintegration of wave trains on deep water. Part 1. Theory. J. Fluid Mech. **27**, 417–430.

Benjamin T. B., Ursell F. (1954). The stability of the plane free surface of a liquid in vertical periodic motion. Proc. R. Soc. Lond. **A 225**, 505–515.

Bergwerk W. (1959). Flow patterns in diesel nozzle spray holes. Proc. Instn. Mech. Engrs. **173**, 655–660.

Bers A. (1975). Linear waves and instabilities. In Physique des Plasmas, C. DeWitt and J. Peyraud, eds. New York: Gordon and Breach, 117–213.

Bhaga T., Weber M. (1981). Bubbles in viscous liquids: shapes, wakes and velocities. J. Fluid Mech. **105**, 61–85.

Bi Q. C., Zhao T. S. (2001). Taylor bubbles in miniaturized circular and noncircular channels. Int. J. Multiphase Flow **27**, 561–570.

Billet M. L. (1985). Cavitation nuclei measurements-A review. ASME Cavitation and Multiphase Flow Forum-1985 **23**, 31–38.

Binnie A. M. (1953). The stability of the surface os a cavitation bubble. Proc. Camb. Phil. Soc. **49**, 151–155.

Bird R., Armstrong R., Hassager O. (1987). Dynamics of Polymeric Liquids. John Wiley & Sons, New York.

Birkhoff G. (1954). Note on Taylor instability. Quart. Appl. Math. **12**, 306–309.

Blake J. R., Gibson D. C. (1987). Cavitation bubbles near boundaries. Annu. Rev. Fluid Mech. **19**, 99–123.

Boulton-Stone J. M., Robinson P. B., Blake J. R. (1996). A note on the axisymmetric interaction of pairs of rising, deforming gas bubbles. Intl J. Multiphase Flow **22**, 122–123.

Brabston D. C., Keller H. B. (1975). Viscous flows past spherical gas bubbles. J. Fluid Mech **69**, 179–189.

Brebbia C. A., Telles J. C. F., Wrobel L. C. (1984). Boundary Element Techniques: Theory and Applications in Engineering. Springer-Verlag.

Brennen C. E. (1995). Cavitation and bubble dynamics. Oxford University Press.

Brenner M. P., Eggers J., Joseph K., Nagel S. R., Shi X. D. (1997). Breakdown of scaling in droplet fission at high Reynolds number. Phys. Fluids **9**, 1573–1590.

Bretherton F. P. (1961). The motion of long bubbles in tubes. J. Fluid Mech. **10**, 166–188.

Briggs L. J. (1950). Limiting negative pressure of water. J. Appl. Phys. **21**, 721–722.

Briggs R. J. (1964). Electron-stream interaction with plasmas. Cambridge: MIT Press. Research Monograph No. 29.

Brodkey R. S. (1967). The Phenomena of Fluid Motions. Addison Wesley, Reading, MA.

Brown R. A. S. (1965). The mechanics of large gas bubbles in tubes. Can. J. Chem Engng. **2**, 217–223.

Byatt-Smith J. G. B., Longuet-Higgins M. S. (1976). On the speed and profile of steep solitary waves. Proc. Roy. Soc. Lond. **A 350**, 175–189.

Canot E., Davoust L., Hammoumi M. E., Lachkar D. (2003). Numerical simulation of the buoyancy-driven bouncing of a 2-D bubble at a horizontal wall. Theort. Comput. Fluid Dynamics **17**, 51–72.

Cerda E. A., Tirapegui E. L. (1998). Faraday's instability in viscous fluid. J. Fluid Mech. **368**, 195–228.

Chandrasekhar S. (1961). Hydrodynamic and Hydromagnetic Stability. Oxford University Press.

Chang H. C., Demekhin E. A., Kalaidin E. (1999). Interated stretching of viscoelastic jets. Phys. Fluids **11**, 1717–1737.

Chang I. D., Russel P. E. (1965). Stabiity of a liquid layer adjacent to a high-speed gas stream. Phys. Fluids **8**, 1018–1026.

Charru F., Hinch E. J. (2000). "Phase diagram" of interfacial instabilities in a two-layer Couette flow and mechanism of the long-wave instability. J. Fluid Mech. **414**, 195–223.

Chaves H., Knapp M., Kubitzek A., Obermeier F., Schneider T. (1995). Experimental study of cavitation in the nozzle hole of diesel injectors using transparent nozzles. Tech. Rep. 950290, SAE Technical Paper.

Chawla T. C. (1975). The Kelvin-Helmholtz instability of the gas-liquid interface of a sonic gas jet submerged in a liquid. J. Fluid Mech. **67**, 513–537.

Chen A. U., Notz P. K., Basaran O. A. (2002). Computational and experimental analysis of pinch-off and scaling. Phys. Rev. Lett. **88**, 1745011–1745014.

Chen J. L. S. (1974). Growth of the boundary layer on a spherical gas bubble. Trans. ASME. J. Appl. Mech. **41**, 873–878.

Chen L., Goto S., Vassilicos J. C. (2006). Turbulent clustering of stagnation points and inertial particles. J. Fluid Mech. **553**, 143–154.

Chen T., Li X. (1999). Liquid jet atomization in a compressible gas stream. J. Propulsion and Power **15**, 369–376.

Chen Y., Israelachvili J. (1991). New mechanism of cavitation damage. Science **252**, 1157–1160.

Chen Y. J., Steen P. H. (1997). Dynamics of inviscid capillary breakup: collapse and pinchoff of a film bridge. J. Fluid Mech. **341**, 245–267.

Chorin A. J. (1973). Numerical study of slightly viscous flow. J. Fluid Mech. **57**, 785–796.

Chorin A. J. (1978). Vortex sheet approximation of boundary layers. J. Comput. Phys. **27**, 428–442.

Christiansen R. M., Hixson A. N. (1957). Breakup of a liquid jet in a denser liquid. Ind. Eng. Chem. **49**, 1017.

Ciliberto S., Gollub J. P. (1985). Chaotic mode competition in parametrically forced surface waves. J. Fluid Mech. **158**, 381–398.

Crowley C. J., Wallis G. B., Barry J. J. (1992). Validation of a one-dimensional wave model for the stratified-to-slug flow regime transition, with consequences for wave growth and slug frequency. Int. J. Multiphase Flow **18**, 249–271.

Crum L. A. (1982). Nucleation and stabilization of microbubbles in liquids. Appl. Sci. Res. **38**, 101–115.

Currie I. G. (1974). Fundamental mechanics of fluids, 1 edn. McGraw-Hill, Inc.

Dabiri S., Sirignano W. A., Joseph D. D. (2006). Two-dimensional viscous aperture flow: Navier-Stokes and viscous-potential-flow solutions. in preparation.

Davies R. M. (1950). The mechanics of large bubbles rising through liquids in tubes. Proc. R. Soc. Lond. **A 200**, 375–390.

Davies R. M., Taylor G. I. (1950). The mechanics of large bubbles rising thorough liquids in tubes. Proc. R. Soc. Lond. **A 200**, 375–390.

Davila J., Vassilicos J. C. (2003). Richardson's pair diffusion and the stagnation point structure of turbulence. Phys. Rev. Lett. **91**, 1–4. Article no.144501.

Day R. F., Hinch E. J., Lister J. R. (1998). Self-similar capillary pinchoff of an inviscid fluid. Phys. Rev. Lett. **80**, 704–707.

de Chizelle Y. K., Brennen C. E. (1993). Comparison of observed and calculated shapes of travellingcavitation bubbles. In Proc. IUTAM Symp. on Bubble Dynamics and Interface Phenomena, Birmingham, UK. 207–217.

de Chizelle Y. K., Ceccio S. L., Brennen C. E. (1995). Observation and scaling of travelling bubble cavitation. J. Fluid Mech. **293**, 99–126.

Dias F., Kharif C. (1999). Nonlinear gravity and capillary-gravity waves. Annu. Rev. Fluid Mech. **31**, 301–346.

Dizés S. L. (1997). Global modes in falling capillary jets. Eur. J. Mech. B/Fluids **16**, 761–778.

Dollet B., Aubouy M., Graner F. (2004). Inverse lift in a flowing foam. Submitted..

Douady S., Fauve S. (1988). Pattern selection in Faraday instability. Europhys. Lett. **6**, 221–226.

Drazin P. G., Reid W. H. (1981). Hydrodynamic Stability. Cambridge University Press.

Dumitrescue D. T. (1943). Stromung and Einer Luftbluse in Senkrechten rohr. Z. Angew. Match. Mech. **23**, 139–149.

Dunne B., Cassen B. (1954). Some phenomena associated with supersonic liquid jets. J. Appl. Phys. **25**, 569–572.

Dunne B., Cassen B. (1956). Velocity discontinuity instability of a liquid jet. J. Appl. Phys **27**, 577–582.

Dyke M. V. (1962). Higher approximations in boundary-layer theory. Part 1. General analysis. J. Fluid Mech. **14**, 161–177.

Dyke M. V. (1969). Higher-order boundary-layer theory. Annu. Rev. Fluid Mech. **1**, 265–292.

Ece M. C., Walker A. D. J., Doligalski L. T. (1984). The boundary layer on an impulsively started rotating and translating cylinder. Phys. Fluids. **27(5)**, 1077–1089.

Edwards W. S., Fauve S. (1993). Parametrically excited quasicrystalline surface waves. Phys. Rev. E **47**, R788–R791.

Eggers J. (1993). Universal pinching of 3D axisymmetric free-surface flow. Phys. Rev. E. **71**, 3458–3460.

Eggers J. (1997). Nonlinear dynamics and breakup of free-surface flows. Rev. Mod. Phys. **69**, 865–930.

Engel O. G. (1958). Fragmentation of waterdrops in the zone behind an air shock. J. Res. Nat'l. Bur. Stand **60**, 245–280.

Entov V. M. (1978). On the stability of capillary jets of elastoviscous fluids. J. Engineering Physics & Thermophysics **34**, 243.

Faeth G. M. (1996). Spray combustion phenomena. In Twenty-sixth symposium on combustion. The Combustion Institute, 1593–1611.

Farrell K. J. (2003). Eulerian/Lagrangian analysis for the prediction of cavitation inception. J. Fluids Eng. **125**, 46–52.

Feng Z. C., Sethna P. R. (1989). Symmetry breaking bifurcations in resonant surface waves. J. Fluid Mech. **199**, 495–518.

Fisher J. C. (1948). The fracture of liquids. J. Appl. Phys. **19**, 1062–1067.

Fluent Inc. Lebanon, NH. (2003). Fluent 6. 1. User's Guide. Fluent Inc. Lebanon, NH.

Foteinopoulou K., Mavrantzas V. G., Tsamopoulos J. (2004). Numerical simulation of bubble growth in Newtonian and viscoelastic filaments undergoing stretching. J. Non-Newtonian Fluid Mech. **122**, 177–200.

Franc J. P., Michel J. M. (1985). Attached cavitation and the boundary layer; experimental investigation and numerical treatment. J. Fluid Mech. **154**, 63–90.

Francis J. R. D. (1951). The aerodynamic drag of a free water surface. Proc. Roy. Soc. **A 206**, 387–406.

Funada T., Joseph D. D. (2001). Viscous potential flow analysis of Kelvin-Helmholtz instability in a channel. J. Fluid Mech. **445**, 263–283.

Funada T., Joseph D. D. (2002). Viscous potential flow analysis of capillary instability. Int. J. Multiphase Flow **28**, 1459–1478.

Funada T., Joseph D. D. (2003). Viscoelastic potential flow analysis of capillary instability. J. Non-Newtonian Fluid Mech. **111**, 87–105.

Funada T., Joseph D. D., Maehara T., Yamashita S. (2004). Ellipsoidal model of the rise of a Taylor bubble in a round tube. Int. J. Multiphase Flow **31**, 473–491.

Funada T., Joseph D. D., Saitoh M., Yamashita S. (2006). Liquid jet into a high Mach number air stream. Int. J. Multiphase Flow **32**, 20–50.

Funada T., Joseph D. D., Yamashita S. (2004). Stability of a liquid jet into incompressible gases and liquids. Int. J. Multiphase Flow **30**, 1279–1310.

Funada T., Padrino J. C., Joseph D. D. (2006). Viscous potential flow of the Kelvin-Helmholtz instability of a cylindrical jet of one fluid into the same fluid. in preparation.

Funada T., Saitoh M., Wang J., Joseph D. D. (2005). Stability of a liquid jet into incompressible gases and liquids: Part 2. Effects of the irrotational viscous pressure. Int. J. Multiphase Flow **31**, 1134–1154.

Funada T., Wang J., Joseph D. D. (2005). Viscous potential flow analysis of stress induced cavitation in an aperture flow. Atomization and Sprays. accepted.

Funada T., Wang J., Joseph D. D., Tashiro N. (2005). Irrotational Faraday waves on a viscous fluid. J. Fluid Mech.. submitted.

Galdi P. G., Pokomy M., Vaidya A., Joseph D. D., Feng J. (2002). Orientation of symmetric bodies falling in a second-order liquid at non-zero Reynolds number. Math. Models Methods Appl. Sci. **12(11)**, 1653–1690.

Georgescu S. C., Achard J. L., Canot E. (2002). Jet drops ejection in bursting gas bubbles processes. Eur. J. Mech. B/Fluids **21**, 265–280.

Gibson A. H. (1913). Long air bubbles in a vertical tube. Phil. Mag. **Series 6**, 952.

Glauert M. B. (1957). The flow past a rapidly rotating circular cylinder. Proc. R. Soc. Lond. **A 242**, 108–115.

Goldin M., Yerushalmi J., Pfeffer R., Shinnar R. (1969). Breakup of a laminar capillary jet of a viscoelastic fluid. J. Fluid Mech. **38**, 689–711.

Goldstein S. (1960). Lectures on Fluid Mechanics. Interscience Publishers.

Goren S. L., Gottlieb M. (1982). Surface-tension-driven breakup of viscoelstic liquid threads. J. Fluid Mech. **120**, 245–266.

Grace J. R., Harrison D. (1967). The influence of bubble shape on the rise velocities of large bubbles. Chem. Eng. Sci. **22**, 1337–1347.

Grace J. R., Wairegi T., Brophy J. (1978). Break-up of drops and bubbles in stagnant media. Can. J. Chem. Engng. **65**, 3–8.

Gu X. M., Sethna P. R. (1987). Resonant surface waves and chaotic phenomena. J. Fluid Mech. **183**, 543–565.

Haberman W. L., Morton R. K. (1953). An experimental investigation of the drag and shape of air bubbles rising in various liquids. Tech. rep., US (Navy) David W. Taylor Model Basin Rep. 802.

Hamel G. (1917). Spiralförmige Bewgungen zäher Flüssigkeiten. Jahresbericht der Deutschen Mathematikar-Vereinigung **25**, 34–60.

Hamel G. (1941). Über die potentialströmungen zäher flüssigkeiten. Z. Angew. Math. Mech. **21**, 129–139.

Hanson A. R., Domich E. G. (1956). The effect of viscosity on the breakup of droplets by air blasts–a shock tube study. Research Report No. 130, Dept. of Aerospace Engineering, Univ. of Minnesota, Minneapolis, MN.

Hanson A. R., Domich E. G., Adams H. S. (1963). Shock tube investigation of the breakup of drops by air blasts. Phys. Fluids **6**, 1070–1080.

Harper J. F. (1972). The motion of bubbles and drops through liquids. Adv. Appl. Mech. **12**, 59–129.

Harper J. F., Moore D. W. (1968). The motion of a spherical liquid drop at high Reynolds number. J. Fluid Mech. **32**, 367–391.

Harrison W. J. (1908). The influence of viscosity on the stability of superposed fluids. Proc. London Math. Soc. **6**, 396–405.

Harvey E. N., Barnes D. K., McElroy W. D., Whiteley A. H., Pease D. C., Cooper K. W. (1944). Bubble formation in animals, I. Physical factors. J. Cell. Comp. Physiol. **44**, 1–22.

Harvey E. N., McElroy W. D., Whiteley A. H. (1947). On cavity formation in water. J. Appl. Phys. **18**, 162–172.

Harvey E. N., Whiteley A. H., McElroy W. D., Pease D. C., Barnes D. K. (1944b). Bubble formation in animals, II. Gas nuvlei and their distribution in blood and tissues. J. Cell. Comp. Physiol. **44**, 23–34.

Hattori S. (1935). On motion of cylindrical bubble in tube and its application to measurement of surface tension of liquid. Rep. Aeronaut. Res. Inst. Tokyo Imp. Univ. **115**.

Hesla T., Huang A., Joseph D. D. (1993). A note on the net force and moment on a drop due to surfaces forces. J. Colloid Interface Sci. **158**, 255–257.

Hicks W. M. (1884). On the steady motion and small vibrations of a hollow vortex. Phil. Trans. Roy. Soc. Lond. **175**, 161–195.

Hiemenz K. (1911). Die Grenzschicht an einem in den gleichförmigen Flüssigkeitsstrom eingetauchten geraden Kreiszylinder. Göttingen Dissertation; and Dingler's Polytech. J. **326**, 321.

Higuera M., Knobloch E. (2006). Nearly inviscid Faraday waves in slightly rectangular containers. Prog. Theor. Phys. Supp. **161**, 53–67.

Higuera M., Knobloch E., Vega J. M. (2005). Dynamics of nearly inviscid Faraday waves in almost circular containers. Physica D **201**, 83–120.

Hirahara H., Kawahashi M. (1992). Experimental investigation of viscous effects upon a breakup of droplets in high-speed air flow. Exp. in Fluids **13**, 423–428.

Homann F. (1936). Der Einfluss grosser Zähigkeit bei der Strömmung um den Zylinder und um die Kugel. Z. Angew. Math. Mech. **16**, 153–164.

Howarth L. (1953). Modern developments in fluid dynamics: high speed flow. Oxford: Clarendon Press.

Hsiang L. P., Faeth G. M. (1992). Near-limit drop deformation and secondary breakup. Int. J. Multiphase Flow **18**, 635–652.

Hu H. H., Riccius O., Chen K. P., Arney M., Joseph D. D. (1990). Climbing constant, second-order correction of Trouton's viscosity, wave speed and delayed die swell for M1. J. Non-Newt. Fluid. Mech. **35**, 287–307.

Huang P. Y., Hu H. H., Joseph D. D. (1997). Direct simulation of the sedimentation of elliptic particles in Oldroyd-B fluids. J. Fluid Mech. **362**, 297–325.

Huerre P. (2000). Open shear flow instabilities. Cambridge University Press.

Huerre P., Monkewitz P. A. (1985). Absolute and convective instabilities in free shear layers. J. Fluid Mech. **159**, 151–168.

Hwang S. S., Liu Z., Reitz R. D. (1996). Breakup mechanisms and drag coefficients of highspeed vaporizing liquid drops. Atomization and Sprays **6**, 353–376.

Jaswon M. A., Symm G. T. (1977). Integral Equation Methods in Potential Theory and Elastostatics. Academic Press INC.

Jeffery G. B. (1915). The two-dimensional steady motion of a viscous fluid. Phil. Mag. **6**, 455–465.

Johnson T. A., Patel V. C. (1999). Flow past a sphere up to a Reynolds number of 300. J. Fluid Mech. **378**, 19–70.

Joseph D. D. (1973). Domain perturbations: The higher order theory of infinitesimal water waves. ARMA **51(4)**, 295–303.

Joseph D. D. (1976). Stability of Fluid Motions, I and II. Vol. 27 and 28. Springer Tracs in Natural Philosophy.

Joseph D. D. (1990). Fluid Dynamics of Viscoelastic Liquids. Vol. 84. Springer-Verlag. Applied Mathematical Sciences.

Joseph D. D. (1992). Bernoulli equation and the competition of elastic and inertial pressures in the potential flow of a second-order fluid. J. Non-Newtonian Fluid Mech. **42**, 385–389.

Joseph D. D. (1992b). Understanding cusped interfaces. J. Non-Newt. Fluid Mech. **44**, 127–148.

Joseph D. D. (1995). Cavitation in a flowing liqud. Phy. Rev. E **51**, 1649–1650.

Joseph D. D. (1996). Flow induced microstructure in Newtonian and viscoelastic fluids. In Proc. 5 th World Congress of Chem. Eng., Particle Technology Track, San Diego. July 14-18. Vol. 6. AICHE, 3–16.

Joseph D. D. (1998). Cavitation and the state of stress in a flowing liquid. J. Fluid Mech. **366**, 367–378.

Joseph D. D. (2000). Interrogations of direct numerical simulation of solid-liquid flow. available at http://www.efluids.com/efluids/books/joseph.htm: www.efluids.com.

Joseph D. D. (2003a). Rise velocity of a spherical cap bubble. J. Fluid Mech. **488**, 213–223.

Joseph D. D. (2003b). Viscous potential flow. J. Fluid Mech. **479**, 191–197.

Joseph D. D. (2006a). (Helmholtz decomposition) to: An addendum to the paper "Potential flow of viscous fluids: historical notes". Int. J. Multiphase Flow **32**, 285–310.

Joseph D. D. (2006b). Potential flow of viscous fluids: Historical notes. Int. J. Multiphase Flow **32**, 285–310.

Joseph D. D. (2006c). Helmholtz decomposition coupling rotational to irrotational flow of a viscous fluid. Proceedings of the National Academy of Sciences **PNAS published September 18, 2006, 10.1073/pnas.0605792103 (Applied Mathematics)**, 14272–14277. http://www.pnas.org/papbyrecent.shtml.

Joseph D. D., Beavers G. S., Funada T. (2002). Rayleigh-Taylor instability of viscoelastic drops at high Weber numbers. J. Fluid Mech. **453**, 109–132.

Joseph D. D., Belanger J., Beavers G. S. (1999). Breakup of a liquid drop suddenly exposed to a high-speed airstream. Int. J. Multiphase Flow **25**, 1263 –1303.

Joseph D. D., Feng J. (1996). A note on the forces that move particles in a second-order fluid. J. Non-Newt. Fluid. Mech. **64**, 299–302.

Joseph D. D., Huang A., Candler G. V. (1996). Vaporization of a liquid drop suddenly exposed to a high-speed airstream. J. Fluid Mech. **318**, 223–239.

Joseph D. D., Liao T. Y. (1994a). Potential flow of viscous and viscoelastic fluids. J. Fluid Mech. **265**, 1–23.

Joseph D. D., Liao T. Y. (1994b). Viscous and viscoelastic potential flow. In Trends and Perspectives in Applied Mathematics, Applied Mathematical Sciences, L. Sirovich, ed. Springer-Verlag, Chapter 5, 109–154. Also in Army HPCRC preprint 93-010., 100, 1-54.

Joseph D. D., Liao T. Y., Hu H. H. (1993). Drag and moment in viscous potential flow. Eur. J. Mech. B/Fluids **12**, 97–106.

Joseph D. D., Liao T. Y., Saut J. C. (1992). Kelvin-helmholtz mechanism for side branching in the displacement of light with heavy fluid under gravity. Rur. J. Mech. B/Fluids **11**, 253–264.

Joseph D. D., Renardy Y. Y. (1991). Fundamentals of two-fluid dynamics. Springer-Verlag.

Joseph D. D., Saut J. C. (1990). Short-wave instabilities and ill-posed initial-value problems. Theroetical Comput. Fluid Dynamics **1**, 191–227.

Joseph D. D., Wang J. (2004). The dissipation approximation and viscous potential flow. J. Fluid Mech. **505**, 365–377.

Kang I. S., Leal L. G. (1988a). The drag coefficient for a spherical bubble in a uniform streaming flow. Phys. Fluids **31**, 233–237.

Kang I. S., Leal L. G. (1988b). Small-amplitude perturbations of shape for a nearly spherical bubble in an inviscid straining flow (steady shapes and oscillatory motion). J. Fluid Mech. **187**, 231–266.

Kang S., Choi H., Lee S. (1999). Laminar flow past a rotating circular cylinder. Phys. Fluids **11**, 3312–3321.

Keller J. B., Miksis M. J. (1983). Surface tension driven flows. SIAM J. Appl. Math. **43**, 268–277.

Keller J. B., Rubinow S. I., Tu Y. O. (1973). Spatial instability of a jet. Phys. Fluids **16**, 2052–2055.

Kellogg O. D. (1929). Foundations of Potential Theory. Springer-Verlag.

Kitscha J., Kocamustafaogullari G. (1989). Breakup criteria for fluid particles. Int. J. Multiphase Flow **15**, 573–588.

Knapp R. T. (1958). Cavitation and nuclei. Trans. ASME **80**, 1315–1324.

Knapp R. T., Daily J. W., Hammit F. G. (1970). Cavitation. McGraw-Hill, Inc.

Knapp R. T., Kottke P. A., Bair S., Winer W. O. (2003). The measurement of viscosity of liquids under tension. J. Tribol. **125**, 260–266.

Kojo T., Ueno I. (2006). Bubble behavior under ultrasonic vibration - nonlinear oscillation and multiple bubble interaction. Space Utiliz Res. **22**, 67–69.

Kordyban E. S., Ranov T. (1970). Mechanism of slug formation in horizontal two-phase flow. Trans. ASME J. Basic Engng. **92**, 857–864.

Kottke P. A., Bair S., Winer W. O. (2003). The measurement of viscosity of liquids under tension. J. Tribol. **125**, 260–266.

Kottke P. A., Bair S., Winer W. O. (2005). Cavitation in creeping shear flows. AIChE J. **51**, 2150–2170.

Krzeczkowski S. A. (1980). Measurement of liquid droplet disintegration mechanisms. Int. J. Multiphase Flow **6**, 227–239.

Kuhl T., Ruths M., Chen Y., Israelachvili J. (1994). Direct visualization of cavitation and damage in ultrathin liquid films. J. Heart Valve Disease **3**, 117–127.

Kumar K., Tuckerman L. S. (1994). Parametric instability of the interface between two fluids. J. Fluid Mech. **279**, 49–68.

Kumar S. (2000). Mechanisms for the faraday instability in viscous liquids. Phys. Rev. E **62**, 1416–419.

Lagerstrom A. P., Cole D. J. (1955). Examples illustrating expansion procedures for the Navier-Stokes equations. J. Rat. Mech. **4**, 817–882.

Lamb H. (1932). Hydrodynamics, 6 edn. Cambridge University Press (Reprinted by Dover 1945).

Landau L. D., Lifshitz E. M. (1987). Fluid Mechanics, 2 edn. Butterworth-Heinemann.

Lane W. R. (1951). Shatter of drops in stream of air. Ind. Engng Chem. **43**, 1312–1317.

Laoonual Y., Yule A. J., Walmsley S. J. (2001). Internal fluid flow and spray visualization for a large scale valve covered orifice (VCO) injector nozzle. ILASS-Europe 2001.

Larson R. G. (1988). Constitutive Equations for Polymer Melts and Solutions. Butterworths Series in Chemical Engineering.

Leib S. J., Goldstein M. E. (1986a). Convective and absolute instability of a viscous liquid jet. Phys. Fluids **29**, 952–954.

Leib S. J., Goldstein M. E. (1986b). The generation of capillary instability on a liquid jet. J. Fluid Mech. **168**, 479–500.

Levich V. G. (1949). The motion of bubbles at high Reynolds numbers. Zh. Eksp. Teor. Fiz. **19**, 18. see also in Physiochemical Hydrodynamics (English transl. By Scripta Technica), p. 436f. Prentice-Hall, 1962.

Li H. S., Kelly R. E. (1992). The instability of a liquid jet in a compressible airstream. Phys. Fluids **A 4**, 2162–2168.

Lighthill M. J. (1963). Introduction. boundary layer theory. In Laminar Boundary Layers, L. Rosenhead, ed. Oxford University Press, Chapter II, 56–58.

Lin P. Y., Hanratty T. J. (1986). Prediction of the initiation of slugs with linear stability theory. Int. J. Multiphase Flow **12**, 79–98.

Lin S. P. (2003). Breakup of Liquid Sheets and Jets. Cambridge University Press.

Lin S. P., Lian Z. W. (1989). Absolute instability in a gas. Phys. Fluids **A 1**, 490–493.

Liu J. Y., Joseph D. D. (1993). Sedimentation of particles in polymer solutions. J. Fluid Mech. **255**, 565–595.

Liu J. Y., Liao Y. T., Joseph D. D. (1995). A two-dimensional cusp at the trailing edge of an air bubble rising in a viscoelastic liquid. J. Fluid Mech. **304**, 321–342.

Liu Y. J. (1995). Particle motions in non-Newtonian fluids. Ph.D. thesis, University of Minnesota.

Liu Z., Brennen C. E. (1998). Cavitation nuclei population and event rates. J. Fluids Eng. **120**, 728–737.

Liu Z., Reitz R. D. (1997). An analysis of the distortion and breakup mechanisms of highspeed liquid drops. Int. J. Multiphase Flow **23**, 631–650.

Loiseleux T., Chomaz J. M., Huerre P. (1998). The effect of swirl on jets and wakes: Linear instability of the Rankine vortex with axial flow. Physics of Fluids **10**, 1120–1134.

Longuet-Higgins M. S. (1992). Theory of weakly damped Stokes waves: a new formulation and its physical interpretation. J. Fluid Mech. **235**, 319 – 324.

Longuet-Higgins M. S. (1997). Viscous dissipation in steep capillary–gravity waves. J. Fluid Mech. **344**, 271 – 289.

Longuet-Higgins M. S., Cokelet E. D. (1976). The deformation of steep surface waves on water. I. A numerical method of computation. Proc. R. Soc. Lond. **A 350**, 1–26.

Lundgren T. S., Joseph D. D. (2006). Symmetric model of capillary collapse and rupture. unpublished.

Lundgren T. S., Mansour N. N. (1988). Oscillations of drops in zero gravity with weak viscous effects. J. Fluid Mech. **194**, 479–510.

Lundgren T. S., Mansour N. N. (1991). Vortex ring bubbles. J. Fluid Mech. **224**, 177–196.

Machane R., Canot E. (1997). High-order schemes in boundary element methods for transient non-linear free surface problems. *Int. J. Numer. Methods Fluids* **24**, 1049–1072.

Magnaudet J., Eames I. (2000). The motion of high-Reynolds-number bubbles in inhomogeneous flows. *Annu. Rev. Fluid Mech.* **32**, 659–708.

Magnaudet J., Rivero M., Fabre J. (1995). Accelerated flows past a rigid sphere or a spherical bubble. Part 1. Steady straining flow. *J. Fluid Mech.* **284**, 97–135.

Maslen H. S. (1963). Second-order effects in laminar boundary layers. *AIAA J.* **1**, 33–40.

Mata C., Pereyra E., Trallero J. L., Joseph D. D. (2002). Stability of stratified gas-liquid flows. *Int. J. Multiphase Flow* **28**, 1249–1268.

Matta J. E., Tytus R. P. (1982). Viscoelastic breakup in a high velocity airstream. *J. Appl. Polymer Science* **27**, 397–405.

Matta J. E., Tytus R. P., Harris J. (1983). Aerodynamic atomization of polymeric solutions. *Chem Eng. Commun.* **19**, 191–204.

McKinley G. H., Tripathi A. (2000). How to extract the Newtonian viscosity from capillary breakup measurements in a filament rheometer. *J. Rheol.* **44**, 653–671.

Meiron D. I., Saffman P. G. (1983). Overhanging interfacial gravity waves of large amplitude. *J. Fluid Mech.* **129**, 213–218.

Michele J., Pazold R., Donis R. (1977). Alignment and aggregation effects in suspensions of spheres in non-Newtonian media. *Rheol. Acta.* **16**, 317–321.

Middleman S. (1965). Stability of a viscoelastic jet. *Chem. Eng. Sci.* **20**, 1937.

Miksis M., Broeck J. M. V., Keller J. B. (1981). Axisymmetric bubble or drop in a uniform flow. *J. Fluid Mech.* **108**, 89–100.

Miksis M., Vanden-Broeck J. M., Keller J. B. (1982). Rising bubbles. *J. Fluid Mech.* **123**, 31–41.

Miles J. W. (1967). Surface-wave damping in closed basins. *Proc. R. Soc. London* **A 297**, 459–475.

Miles J. W. (1984). Nonlinear Faraday resonance. *J. Fluid Mech.* **146**, 285–302.

Miles J. W., Henderson D. M. (1990). Parametrically forced surface waves. *Annu. Rev. Fluid Mech.* **22**, 143–165.

Miller C. A., Scriven L. E. (1968). The oscillations of a droplet immersed in another fluid. *J. Fluid Mech.* **32**, 417–435.

Milne-Thomson L. M. (1968). *Theoretical Hydrodynamics*, fifth edn. Macmillan & Co. Ltd.

Mishima K., Ishii M. (1980). Theoretical prediction of onset of horizontal slug flow. *Trans. ASME J. Fluids Engng.* **102**, 441–445.

Mittal S., Kumar B. (2003). Flow past a rotating cylinder. *J. Fluids Mech.* **476**, 303–334.

Moore D. W. (1959). The rise of a gas bubble in a viscous liquid. *J. Fluid Mech.* **6**, 113–130.

Moore D. W. (1963). The boundary layer on a spherical gas bubble. *J. Fluid Mech.* **16**, 161–176.

Moore W. D. (1957). The flow past a rapidly rotating circular cylinder in a uniform stream. *J. Fluid Mech.* **2**, 541–550.

Nayfeh A. H., Saric W. S. (1973). Nonlinear stability of a liquid film adjacent to a supersonic stream. *J. Fluid Mech.* **58**, 39–51.

Ockendon J. R., Ockendon H. (1973). Resonant surface waves. *J. Fluid Mech.* **59**, 397–413.

Oguz H., Prosperetti A. (1989). Surface-tension effects in the contact of liquid surfaces. *J. Fluid Mech.* **203**, 149–171.

Oguz H., Prosperetti A. (1990). Bubble entrainment by the impact of drops on liquid surfaces. *J. Fluid Mech.* **219**, 143–179.

Oguz H., Prosperetti A. (1993). Dynamics of bubble growth and detachment from a needle. *J. Fluid Mech.* **257**, 111–145.

Ortiz C., Joseph D. D., Beavers G. S. (2004). Acceleration of a liquid drop suddenly exposed to a high speed air stream. *Int. J. Multiphase Flow* **30**, 217–224.

Padrino J. C., Joseph D. D. (2006a). Correction of Lamb's dissipation calculation for the effects of viscosity on the wave speed of capillary-gravity waves. In preparation.

Padrino J. C., Joseph D. D. (2006b). Numerical study of the steady state uniform flow past a rotating cylinder. *J. Fluid Mech.* **557**, 191–223.

Padrino J. C., Joseph D. D., Funada T., Wang J., Sirignano W. A. (2005). Stress induced cavitation for the streaming motion of a viscous liquid past a sphere. *J. Fluid Mech.*. submitted.

Pan T. W., Joseph D. D., Glowinski R. (2001). Modelling Rayleigh-Taylor instability of a sedimenting suspension of several thousand circular particles in a direct numerical simulation. *J. Fluid Mech.* **434**, 23–37.

Panton L. R. (1984). *Incompressible flow*. Wiley-Interscience.

Papageriou D. T. (1995). On the breakup of viscous liquid threads. *Phys. Fluids* **7**, 1529–1544.

Park W. C., Klausner J. F., Mei R. (1995). Unsteady forces on spherical bubbles. *Exp. Fluids* **19**, 167–172.

Pedley T. J. (1967). The stability of rotating flows with a cylindrical free surface. *J. Fluid Mech.* **30**, 127–147.

Pedley T. J. (1968). The toroidal bubble. *J. Fluid Mech.* **32**, 97–112.

Peregrine D. H., Shoker G., Symon A. (1990). The bifurcation of liquid bridges. *J. Fluid Mech.* **212**, 25–39.

Pereira A., McGrath G., Joseph D. D. (2001). Flow and stress induced cavitation in a journal bearing with axial throughput. *J. Tribol.* **123**, 742–754.

Perlin M., Schultz W. W. (2000). Capillary effects on surface waves. *Annu. Rev. Fluid Mech.* **32**, 241–274.

Petit L., Noetinger B. (1988). Shear-induced structure in macroscopic dispersions. *Rheol. Acta.* **27**, 437–441.

Pilch M., Erdman C. (1987). Use of break-up time data and velocity history data to predict the maximum size of stable fragments for acceleration-induced break-up of a liquid drop. *Int. J. Multiphase Flow* **13**, 741–757.

Plateau. (1873). *Statique expérimentale et Théorique des Liquides*. Gauthier-Villars.

Plesset M. (1949). The dynamics of cavitation bubbles. *ASME J. Appl. Mech.* **16**, 228–231.

Plesset M. (1969). Tensile strength of liquids. Tech. rep., Office of Naval Res. Rep.

Plesset M. S. (1954). On the stability of fluid flows with spherical symmetry. *J. Appl. Phys.* **25(1)**, 96–98.

Plesset M. S., Prosperetti A. (1977). Bubble dynamics and cavitation. *Annu. Rev. Fluid Mech.* **9**, 145–185.

Ponstein J. (1959). Instability of rotating cylindrical jets. *Appl. sci. Res.* **A 8**, 425–456.

Poritsky M. (1951). The collapse on growth of a spherical bubble on cavity in a viscous fluid. In *Proceedings of the first U.S. National Congress of Applied Mechanics held at the Illinois Institute of Technology*. ASME, 813–821.

Pouliquen O., Chomaz J. M., Huerre P. (1994). Propagating Holmboe waves at the interface between two immiscible fluids. J. Fluid Mech. **226**, 277–302.

Pozrikidis C. (1992). Boundary Integral and Singularity Methods for Linearized Viscous Flow. Cambridge University Press.

Prandtl L., Tietjens G. O. (1934). Applied Hydro-and Aero-mechanics. New York: McGraw-Hill.

Pretsch J. (1938). Zur theoretischen berechnung des profilwiderstandes. Jahrb. d. dt. Luftfahrtforschung **I, 61.Engl. transl.**, NACA TM 1009.

Prosperetti A. (1976). Viscous effects on small-amplitude surface waves. Phys. Fluids **19**, 195–203.

Prosperetti A. (1980). Normal-mode analysis for the oscillations of a viscous liquid drop in an immiscible liquid. J. Méc **19**, 149.

Pruppacher H. R., Clair B. P. L., Hamiliec A. E. (1970). Some relations between drag and flow pattern of viscous flow past a sphere and a cylinder at low and intermediate Reynolds numbers. J. Fluid Mech. **44**, 781–790.

Pullin D. I. (1982). Numerical studies of surface-tension effects in nonlinear Kelvin-Helmholtz and Rayleigh-Taylor instability. J. Fluid Mech. **119**, 507–532.

Ranger A. A., Nicholls J. A. (1969). Aerodynamic shattering of liquid drops. AIAA J. **7**, 285–290.

Rayleigh L. (1877). The Theory of Sound. London: Macmillan.

Rayleigh L. (1878). On the instability of jets. Proc. Lond. Math. Soc. **10**, 4–13.

Rayleigh L. (1879). On the capillary phenomena of jets. Proc. Roy. Soc. London **A 29**, 71.

Rayleigh L. (1883a). On maintained vibrations. Philos. Mag. **15**, 229–235. Reprinted, 1900, in Scientific Papers, 2: 188-93. Cambridge: Univ. Press.

Rayleigh L. (1883b). On the crispations of fluid resting upon a vibrating support. Philos. Mag. **16**, 50–58. Reprinted, 1900, in Scientific Papers, 2: 212-19. Cambridge: Univ. Press.

Rayleigh L. (1890). On the theory of surface forces. Phil. Mag. **Sci. 5, 30 (185)**, 285–298.

Rayleigh L. (1892). On the instability of a cylinder of viscous liquid under capillary force. Phil. Mag. **34**, 145.

Rayleigh L. (1917). On the pressure developed in a liquid during the collapse of a spherical cavity. Phil. Mag. **34**, 94–98.

Reinecke W. G., McKay W. L. (1969). Experiments on water drop breakup behind Mach 3 to 12 shocks. Tech. rep., AVTD-0172-69-RR, AVCO Corp.

Reinecke W. G., Waldman G. D. (1970). A study of drop breakup behind strong shocks with applications to flight. Tech. rep., SAMSO-TR-70-142, Avco Systems Division.

Reinecke W. G., Waldman G. D. (1975). Shock layer shattering of cloud drops in reentry flight. AIAA Paper **75–152**.

Rodriguez-Rodriguez J., Gordillo J. M., Martinez-Bazan C. (2006). Breakup time and morphology of drops and bubbles in a high-Reynolds-number flow. J. Fluid Mech. **548**, 69–86.

Romberg G. (1967). Über die Dissipation in dichtebeständiger Strömung. Z. f. angew. Math. u. Mech. **47**, 155–162.

Roos F. W., Willmarth W. W. (1971). Some experimental results on sphere and disk drag. AIAA J. **9**, 285–291.

Rothert A., Richter R., Rehberg I. (2001). Transition from symmetric to asymmetric scaling function before drop pinch-off. Phy. Rev Lett. **87**, 084501–1–4.

Ruvinsky K. D., Feldstein F. I., Freidman G. I. (1991). Numerical simulations of the quasi-stationary stage of ripple excitation by steep capillary-gravity waves. J. Fluid Mech. **230**, 339 – 353.

Ruvinsky K. D., Freidman G. I. (1985a). Improvement of the first Stokes method for the investigation of finite-amplitude potential gravity-capillary waves. In 9th All Union Symp on Diffraction and Propagation Waves. Vol. 2. 22–25. Theses of Reports.

Ruvinsky K. D., Freidman G. I. (1985b). Ripple generation on gravity-capillary wave crests and its influence on wave propagation. Tech. rep., Inst. Appl. Acad. Sci. USSR Gorky. Preprint 132.

Ruvinsky K. D., Freidman G. I. (1987). The fine structure of strong gravity-capillary waves. In Nonlinear waves: Structures and Bifurcations, A. V. Gaponov-Grekhov and M. I. Rabinovich, eds. Moscow: Nauka, 304–326.

Ryskin G., Leal L. G. (1984). Numerical solution of free-boundary problems in fluid mechanics. Part 1: the finite-difference technique. J. Fluid Mech. **148**, 19–35.

Sangani A. S. (1991). A pairwise interaction theory for determining the linear acoustic properties of dilute bubbly liquids. J. Fluid Mech. **232**, 221 – 284.

Sangani A. S., Didwania A. K. (1993). Dynamic simulations of flows of bubbly liquids at large reynolds numbers. J. Fluid Mech. **250**, 307 – 337.

Scardovelli R., Zaleski S. (1999). Direct numerical simulation of free-surface and interfacial flow. Annu. Rev. Fluid Mech. **31**, 567–603.

Schetz J. A., Kush E. A., Joshi P. B. (1980). Wave phenomena in liquid jet breakup in a supersonic crossflow. AIAA J. **18**, 774–778.

Schlichting H. (1960). Boundary layer theory, translated by J. Kestin, 4th edn. McGraw-Hill.

Schmid P., Henningson D. S. (2001). Stability and Transition in Shear Flows. Springer-Verlag.

Schwartz L. W. (1974). Computer extension and analytic continuation of Stokes' expansion for gravity waves. J. Fluid Mech. **62**, 553 – 578.

Scirocco R., Pellens L., UriguenIbexarra J. I., Vermant J. (2003). Shear flow experiments on particle filled polymers. http://ftp.esrf.fr/pub/UserReports/27721_A.pdf.

Segur H., Henderson D., Carter J. et al. (2005). Stabilizing the Benjamin-Feir instability. J. Fluid Mech. **539**, 229–271.

Sherman A., Schetz J. A. (1971). Breakup of liquid sheets and jets in a supersonic gas stream. AIAA J. **9**, 666–673.

Shi X. D., Brenner M. P., Nagel S. R. (1994). A cascade of structure in a drop falling from a faucet. Science **265**, 219–222.

Simonelli F., Gollub J. P. (1989). Surface wave mode interactions: effects of symmetry and degeneracy. J. Fluid Mech. **199**, 471–94.

Simpkins P. G., Bales E. L. (1972). Water-drop response to sudden accelerations. J. Fluid Mech. **55**, 629–639.

Singhal A. K., Athavale M. M., Li H., Jiang Y. (2002). Mathematical basis and validation of the full cavitation model. J. Fluids Eng. **124**, 617–624.

Sirakov B. T., Greitzer E. M., Tan C. S. (2005). A note on irrotational viscous flow. Phys. Fluids **17**, 108102.

Soteriou C., Andrews R., Smith M. (1995). Direct injection diesel sprays and the effect of cavitation and hydraulic flip on atomization. Tech. Rep. 950080, SAE Technical Paper.

Spiegelberg S. H., Gaudet S., McKinley G. H. (1994a). The extensional rheology of non-newtonian materials. In NASA. Lewis Research Center, Second Microgravity Fluid Physics Conference, 311–317 (SEE N95–14522 03–34).

Spiegelberg S. H., Gaudet S., McKinley G. H. (1994b). In extensional deformation of non-Newtonian materials: Liquid bridge studies. In 2nd Microgravity Fluid Physics Conference. Vol. CP-3276 (U.S. Govt. Printing office 1994-553-454). 311.

Spivak B., Vanden-Broeck J. M., Miloh T. (2002). Free-surface wave damping due to viscosity and surfactants. European Journal of Mechanics - B/Fluids **21**, 207–224.

Stokes G. G. (1851). On the effect of the internal friction of fluids on the motion of pendulums. Trans. Cambr. Phil. Soc. **IX**, 8–106. (read on Dec. 9, 1850) Mathematical and physical papers, **3**, 1–141.

Stokes G. G. (1880). Considerations relative to the greatest height of oscillatory irrotational waves which can be propagated without change of form. Mathematical and physical papers **I**, 225–228.

Stone H. A. (1994). Dynamics of drop deformation and breakup in viscous fluids. Annu. Rev. Fluid Mech. **26**, 65–102.

Strasberg M. (1959). Onset of ultrasonic cavitation in tap water. J. Acoust. Soc. Am. **31**, 163–176.

Tait. (1890). Note on ripples in a viscous liquid. Proc. Roy. Soc. Edin. **xvii. 110**, 322–337. Scientific Papers, Cambridge, 1898 –1900, ii. 313.

Taitel Y., Dukler A. E. (1976). A model for predicting flow regime transitions in horizontal and near horizontal gas-liquid flow. AIChE J. **22**, 47–55.

Taneda S. (1956). Experimental investigation of the wake behind a sphere at low Reynolds numbers. J. Phys. Soc. Japan **11**, 1104–1108.

Taylor G. I. (1923). On the decay of vortices in a viscous fluid. Phil. Mag. **XLVI**, 671–674.

Taylor G. I. (1949). The shape and acceleration of a drop in a high-speed air stream. for Advisory Council on Scientific Research and Technical Development, Ministry of Supply, AC 10647/Phys. C69. also in The Scientific Papers of G.I. Taylor 3, (ed. G.K. Batchelor), University Press, Cambridge (1993).

Taylor G. I. (1950). The instability of liquid surfaces when accelerated in a direction perpendicular to their planes I. Proc. Roy. Soc. **A 201**, 192–196. also in The Scientific Papers of G.I. Taylor, 3 (ed. G.K. Batchelor), University Press, Cambridge (1993).

Taylor T. D., Acrivos A. (1964). On the deformation and drag of a falling viscous drop at low Reynolds number. J. Fluid Mech. **18**, 466–476.

Theofanous T. G., Li G. J., Dinh T. N. (2003). Aerobreakup in rarefied supersonic gas flows. In Proceedings of FEDSM03. Vol. 4-th.

Tomboulides A. G. (1993). Phd thesis. Ph.D. thesis, Princeton University.

Tomotika S. (1935). On the instability of a cylindrical thread of a viscous liquid surrounded by another viscous fluid. Proc. Roy. Soc. London **A 150**, 322–337.

Truesdell C. (1953). The Kinematics of Vorticity. Indiana University Press.

Tsai W., Yue D. K. P. (1996). Computation of non-linear free-surface flows. Annu. Rev. Fluid. Mech. **28**, 249–278.

Varga C. M., Lasheras J. C., Hopfinger E. J. (2003). Initial breakup of a small-diameter liquid jet by a high-speed gas stream. J. Fluid Mech. **497**, 405–434.

Vassilicos J. C., Chen L., Goto S., Osborne D. R. (2005). Persistent stagnation points and turbulent clustering of inertial particles. In Proceedings of Turbulent and Shear Flow Phenomena.

Vaynblat D., Lister J. R., Witelski T. P. (2001). Symmetry and self-similarity in rupture and pinchoff: a geometric bifurcation. Eur. J. Appl. Math. **12**, 209–232.

Vega J. M., Knobloch E., Martel C. (2001). Nearly inviscid Faraday waves in annular containers of moderately large aspect ratio. Physica D-Nonlinear phenomena **154**, 313–336.

Verdon C. P., McCory R. L., Morse R. L., Baker G. R., Meiron D. I., Orszag S. A. (1982). Nonlinear effects of multifrequency hydrodynamic instabilities on ablatively accelerated thin shells. Phys. Fluids **25**, 1653–1674.

Viana F., Funada T., Joseph D. D., Tashiro N., Sonoda Y. (2005). Potential flow of a second-order fluid over a tri-axial ellipsoid. J. App. Math. **Issue 4**, 341–364.

Viana F., Pardo R., Yańez R., Trallero J., Joseph D. (2003). Universal correlation for the rise velocity of Taylor bubbles in round pipes. J. Fluid Mech. **494**, 379–398.

Waldman G. D., Reinecke W. G., Glenn D. (1972). Raindrop breakup in the shock layer of a high-speed vehicle. AIAA J. **10**, 1200–1204.

Wallis G. B. (1969). One dimensional two-phase flow. McGraw-Hill.

Wallis G. B., Dobson J. E. (1973). The onset of slugging in horizontal stratified air-water flow. Int. J. Multiphase Flow **1**, 173–193.

Walters J. K., Davidson J. F. (1963). The initial motion of a gas bubble formed in an inviscid liquid. II. J. Fluid Mech. **17**, 321–336.

Wang J., Bai R., Lewandowski C., Galdi P. G., Joseph D. D. (2004). Sedimentation of cylindrical particles in a viscoelastic liquid: shape-tilting. China Particuology **2(1)**, 13–18.

Wang J., Joseph D. D. (2003). Potential flow of a second order fluid over a sphere or an ellipse. J. Fluid Mech. **511**, 201–215.

Wang J., Joseph D. D. (2006a). Boundary layer analysis for effects of viscosity of the irrotational flow on the flow induced by a rapidly rotating cylinder in a uniform stream. J. Fluid Mech. **557**, 167–190.

Wang J., Joseph D. D. (2006b). The lift, drag and torque on an airfoil in foam modeled by the potential flow of a second-order fluid. submitted.

Wang J., Joseph D. D. (2006c). Pressure corrections for the effects of viscosity on the irrotational flow outside Prandtl's boundary layer. J. Fluid. Mech. **557**, 145–165.

Wang J., Joseph D. D. (2006d). Purely irrotational theories of the effect of the viscosity on the decay of free gravity waves. J. Fluid Mech. **559**, 461–472. (http://www.aem.umn.edu/people/faculty/joseph/ViscousPotentialFlow).

Wang J., Joseph D. D., Funada T. (2005a). Pressure corrections for potential flow analysis of capillary instability of viscous fluids. J. Fluid Mech. **522**, 383–394.

Wang J., Joseph D. D., Funada T. (2005b). Purely irrotational theories of the effects of viscosity and viscoelastacity on capillary instability of a liquid cylinder. J. Non-Newtonian Fluid Mech. **129**, 106–116.

Wang J., Joseph D. D., Funada T. (2005c). Viscous contributions to the pressure for potential flow analysis of capillary instability of two viscous fluids. Phys. Fluids **17**, 052105a.

Weber C. (1931). Zum Zerfall eines Flüssigkeitsstrahles. Ztschr. f. angew, Math. Mech. **11**, 136.

Wegener P. P., Parlange J. Y. (1973). Spherical-cap bubbles. Annu. Rev. Fluid Mech. **5**, 79–100.

White E. T., Beardmore R. H. (1962). The velocity of rise of single cylindrical air bubbles through liquids contained in vertical tubes. Chem. Engng. Sci. **17**, 351–361.

White F. K. (2006). Viscous fluid flow, 3 edn. McGraw-Hill.

Wierzba A. (1990). Deformation and breakup of liquid drops in a gas stream at nearly critical Weber numbers. Experiments in Fluids **9**, 59–64.

Wierzba A., Takayama K. (1988). Experimental investigation of the aerodynamic breakup of liquid drops. AIAA J. **26**, 1329–1335.

Wilcox J. D., June R. K., Braun H. A., Kelly R. C. (1961). The retardation of drop breakup in high-velocity airstreams by polymeric modifiers. J. App. Polymer Sci. **13**, 1–6.

Winer W. O., Bair S. (1987). The influence of ambient pressure on the apparent shear thinning of liquid lubricants-an overlooked phenomena. In Proceedings of the Institution of Mechanical Engineers-Tribology 50 Years. 395–398.

Wrobel L. C. (1993). Numerical solution of axisymmetric cavity flows using the boundary element method. Int. J. Numer. Methods Fluids **16**, 845–854.

Wrobel L. C. (2002). The Boundary Element Method. Volume 1 - Applications in Thermo-Fluids and Acoustics. John Wiley & Sons, Ltd.

Wu H. L., Pots B. F. M., Hollenberg J. F., Meerhoff R. (1987). Flow pattern transitions in two-phase gas/condensate flow at high pressure in an 8-inch horizontal pipe. In 3rd International Conference on Multiphase Flow. Vol. A2. 13–21.

Yang H. Q. (1992). Asymmetric instability of a liquid jet. Phys. Fluids **A 4**, 681–689.

Yang S., Leal G. L. (1991). A note on memory-integral contributions to the force on an accelerating spherical drop at low Reynolds number. Phys. Fluids **A 3**, 1822–1823.

Yariv E., 2003 H. B. (2003). Near-contact electrophoretic motion of a sphere parallel to a planar wall. J. Fluid Mech. **484**, 85–111.

Yariv E., Brenner H. (2004). The electrophoretic mobility of a closely fitting sphere in a cylindrical pore. SIAM Appl. Math. **64**, 423–441.

Yeung R. W. (1982). Numerical methods in free-surface flows. Annu. Rev. Fluid Mech. **14**, 395–442.

Yoo J. (1973). Master thesis, Aerospace Engineering and Mechanics, University of Minnesota.

Yoshida T., Takayama K. (1990). Interaction of liquid droplets with planar shock waves. Trans ASME, J. Fluids Engng **112**, 481–486.

Young F. R. (1989). Cavitation. McGraw-Hill, Inc.

Zhou Z. W., Lin S. P. (1992). Absolute and convective instability of a compressible jet. Phys. Fluids **A4**, 277–282.

Zierep J. (1984). Viscous potential flow. Arch. Mech. **36**, 127–133.

List of Illustrations

1.1 Axisymmetric flow over a sphere of radius a. The flow depends on the radius r and the polar angle θ. 5

3.1 Interface S between two fluids. 10

4.1 (after Taylor 1923) Streamlines for system of eddies dying down under the action of viscosity. The streamlines are iso-vorticity lines; the vorticity vanishes on the border of the cells. 21

4.2 Steady two-dimensional flow toward a 'stagnation point' at a rigid boundary. 22

4.3 Hamel sink flow. (a) flow channel, (b) irrotational sink flow, (c) sink flow with rotational boundary layer. 23

4.4 Hamel source flow.(a) irrotational source flow (b) asymmetric rotational flow, (c) symmetric rotational flow. 23

7.1 Spherical cap bubble. The rising bubble is viewed in a frame in which the bubble is stationary. The origin of z increasing is at the stagnation point $\hat{s}$. The surface of the cap is given by $z = -h(r, \theta) = -(R - r(\theta)\cos\theta)$. The cap is strictly spherical if $r(\theta) = R$ is constant. 31

7.2 (After Viana et al. 2002). Rise velocity Fr vs. $Log\Re_G$ for different Eötvös numbers for all published experiments on the rise velocity of Taylor bubbles in round pipes. The rise velocity is independent of $E\ddot{o}$ when $E\ddot{o} > 40$. //Note that this figure is ./8/fig3-3.eps. The title of the x axis needs to be fixed (Log R_G). // 34

7.3 (After figure 7 in Bhaga & Weber 1981.) $\bar{C}_D$ $(= 4g\bar{d}/U^2)$ vs. $\bar{R}_e$ $(= U\bar{d}/\nu)$. Taylor & Acrivos 1964 (- - -); $\bar{C}_D$ given by (7.2.2) (—); $M = 1.64 \times 10^{-3}$ (●). 35

7.4 Comparison of the empirical drag law (7.2.2) with the theoretical drag law (7.2.6) scaled by the factor 0.445 required to match the data in figure 7.3 with the experiments of Davies & Taylor (1950) at large R_e. 36

8.1 F_r predicted from (8.1.3) vs. experimental data ($E_o > 6$). 38

8.2 Drainage at the wall of a rising Taylor bubble. If U is added to this system the wall moves and the bubble is stationary. 39

8.3 (After Brown 1965). The profile of the cap of Taylor bubbles. The nose region is spherical with a radius r_0. For all the fluids, $r_0/R_c = 0.75$. The viscosities of water, varsol, marcol, and primol apparently are 0.977, 0.942, 19.42 and 142.3 mPa s respectively. 40

8.4 Photographs (unpublished, courtesy of F.Viana & R.Pardo) of Taylor bubbles rising in concentric annular space of 76.2 mm inside diameter pipe and different rod diameter (ID) filled with different viscous liquids: a) Water (1 mPa s, 997 kg/m^3), ID=12.7 mm; b) Water, ID=25.4 mm; c) Water, ID=38.1 mm; d) Silicone oil (1300 mPa s, 970 kg/m^3), ID=12.7 mm; e) Silicone oil (1300 mPa s, 970 kg/m^3), ID=25.4 mm. The gas bubbles do not wrap all the way around the inner cylinder; a channel is opened for liquid drainage. 41

8.5 An ellipsoid bubble moving with a uniform velocity U in the z direction of Cartesian coordinates (x, y, z). An ovary ellipsoid is depicted in the left-hand side and a planetary ellipsoid is in the right-hand side, which are of the major semiaxis a, the minor semiaxis b, the aspect ratio $e = c/a$, $c^2 = a^2 - b^2$, and in a liquid (water) of density ρ, viscosity μ, with the surface tension σ at the surface given by $\xi = \xi_0$ and under the acceleration due to gravity g. 41

8.6 Photographs of Taylor bubbles rising through 76.2 mm inside diameter pipe filled with different viscosity liquids. This figure is quoted from Viana *et al.* (2003). 48

8.7 $\log F_r$ versus $\log R_G$ for 12 values of E_o. The lines - - -, – – –, ——— are plots of (8.2.33) with $e(E_o)$ selected for best fit as described in table 8.1. 50

8.8 $\log E_o$ versus $\log e$; ☐ denotes the data given in table 8.1. The solid curve denotes the border $F_r = 0$ given by (8.2.37), above which one positive solution of F_r may exist and below which there arise two negative sollutions or complex solutions which are meaningless. The dashed line is for $E_o = 4$. The dotted line denotes $\log e = 0.0865513 \log E_o - 0.356762$ for which $e_o = E_o^{0.0866}/0.357$. 51

8.9 Comparison of Brown's 1965 measurements of the shape of a large Taylor bubble rising in a round tube with an ovary ellipsoid (denoted by the dashed line) with $e = c/a = 0.6$, $b = a\sqrt{1-e^2} = 0.8a$, $a = 1.10$. Ovary ellipsoids with smaller e are more spherical. 51

8.10 $e(E_o, R_G)$ versus $\log E_o$ for various values of R_G. The curves ——— are obtained by the simultaneous equations (8.1.3) and (8.2.33). The solution of (8.4.1) and (8.4.2) is shown as - - - - -; all the solutions (8.1.3) and (8.2.33) coincide with - - - - - when $R_G > 10^4$. 52

9.1 RT instability: (a) the liquid in the containers at rest is stable under gravity (Rayleigh 1890) but if the container is turned upside down as in (c) the liquid falls out. The liquid at rest in container can be destabilized by downward acceleration of the liquid $a > g$ away from gas as in (b) and in the upside down case the liquid can be prevented from falling out by accelerating downward with $\dot{V} > g$ as in (d). If we open up the container and accelerates the liquid downward with $\dot{V} > g$, the top surface which accelerates away from the gas is unstable but the bottom surface which accelerates into the gas is stabilized as in (e), with the opposite effect when the acceleration is reversed as in (f). 54

9.2 Growth rate curve. 58

9.3 Time-displacement graph giving the acceleration of drops from the experiment of JBB 1999. 59

9.4 n (sec^{-1}) vs. k (cm^{-1}) for viscous potential flow; shock Mach number = 2. 60

9.5 n (sec^{-1}) vs. k (cm^{-1}) for viscous potential flow; shock Mach number = 3. 61

9.6 Rayleigh-Taylor Waves in Water. The tick marks on the photographs locate wave troughs. 61

9.7 Rayleigh-Taylor Waves in Silicone Oil (0.1 kg/msec). The tick marks on the photographs locate wave troughs. 62

9.8 Rayleigh-Taylor waves in glycerine. The tick marks on the photographs locate wave troughs. 63

9.9 (JBF, figure 14) (a) Rayleigh-Taylor waves in 2% aqueous polyox in the flow behind a Mach 2.9 shockwave. Time (in μs) after passage of shock: (i) 30, (ii) 35, (iii) 40, (iv) 45. (b) Movie frames corresponding to the contrast-enhanced images of (a). 64

9.10 Stages in the breakup of a water drop (diameter = 2.6 mm) in the flow behind a Mach 2 shock wave. Air velocity = 432 m/s; dynamic pressure = 158.0 kPa; Weber No. = 11,700. Time (μs): (a) 0, (b) 45, (c) 70, (d) 135, (e) 170, (f) 290. 65

9.11 Stages in the breakup of a water drop (diameter = 2.5 mm) in the flow behind a Mach 3 shock wave. Air velocity = 764 m/s; dynamic pressure = 606.4 kPa; Weber No. = 43,330. Time (μs): (a) 0, (b) 15, (c) 30, (d) 40, (e) 95, (f) 135. 65

9.12 Stages in the breakup of a drop of glycerine (diameter = 2.4 mm) in the flow behind a Mach 3 shock wave. Air velocity = 758 m/s; dynamic pressure = 554.0 kPa; Weber No. = 42,220. Time (μs): (a) 0, (b) 35, (c) 50, (d) 70, (e) 90, (f) 125, (g) 150, (h) 185. 66

9.13 Snapshots of the sedimentation of 5040 (a; b, W =8 cm) and 7560 (c, W = 12 cm) disks of diameter 14/192 cm in two dimensions. The initial lattice is square. 67

9.14 Snapshots of the sedimentation of 4800 (a; b) and 6400 (c; d) disks in two dimensions (W = 8 cm). The diameter of disks in (a), (b) and (c) is 10/192 cm and the diameter of disks in (d) is 16/192 cm. The initial lattice is rectangular. 68

10.1 A cylinder with radius a near the wall $x = 0$. 69

10.2 The absolute values of the coefficients for the force $|C_x|$ and $|C_y|$ as functions of the ratio b/a. The Reynolds number is taken as 1 when computing C_y. 71

10.3 The lift coefficient C_x as a function of the ratio b/a. The five curves correspond to five values of the parameter $2\pi\kappa/(aV)$: -1, -0.5, 0, 1 and 2. 74

10.4 The drag coefficient C_y as a function of the ratio b/a. The five curves correspond to five values of the parameter $2\pi\kappa/(aV)$: -1, -0.5, 0, 1 and 2. The Reynolds number is taken as 1 here. 75

10.5 The lift coefficient C_x as a function of $2\pi\kappa/(aV)$. The two curves are for b/a =1.5 and 2, respectively. 75

10.6 The drag coefficient C_y as a function of $2\pi\kappa/(aV)$. The two curves are for b/a =1.5 and 2, respectively. The Reynolds number is taken as 1 here. 76

11.1 The speed of the fluid above is greater. The pressure is greater at crests (a) than at troughs (b). The upper part of the interface is carried by upper fluid causing the interface to overturn. 77

11.2 A KH instability rendered visible by clouds over Mount Duval in Australia. 78

11.3 Neutral curves and growth rate curves when surface tension $\gamma \neq 0$. (a) Flow is stable for short and long waves. (b) Flow is stable for short waves but not long waves. 80

11.4 Neutral curves and growth rate curves when $\gamma = 0$. (a) $\mu > 0$. The flow is unstable as $k \to 0$ but not Hadamard unstable. (b) $\mu = 0$, the flow is Hadamard unstable $\sigma_R \to \infty$ with k. 80

11.5 Kelvin Helmholtz instability due to a discontinuity of velocity of air above liquid in a rectangular channel. The no-slip condition is not enforced in viscous potential flow so that the two dimensional solution satisfies the side-wall boundary conditions. 81

11.6 Neutral curves for air and water ($\hat{\mu} = 0.018$, see table 11.1 and figure 11.8); $\alpha = \hat{h}_a$ is the gas fraction. As in the usual manner, the disturbances will grow above the neutral, but decay below it. For α larger than about 0.2, there arises the critical velocity V_c below which all the disturbances will decay. 87

11.7 Neutral curves for inviscid fluids ($\hat{\mu} = \hat{\rho} = 0.0012$) for different gas fractions $\alpha = \hat{h}_a$. This neutral curve arose for the special case $\hat{\mu} = \hat{\rho} = 0.0012 = \mu_a/\mu_l$ with $\mu_a = 0.00018$ poise; hence $\mu_l = 0.15$ poise. Surprisingly it is identical to the case $\mu_a = \mu_l = 0$ (see table 11.2 and figure 11.8). The neutral curves for viscous fluids with $\mu_l > 15$ cp are essentially the same as these (c.f. table 11.2 and 11.3). 88

11.8 Critical velocity V vs. $\hat{\mu}$ for $\alpha = 0.5$. The critical velocity is the minimum value on the neutral curve. The vertical line is $\hat{\mu} = \hat{\rho} = 0.0012$ and the horizontal line at $V = 635.9$ cm/sec is the critical value for inviscid fluids. The vertical dashed line at $\hat{\mu} = 0.018$ is for air and water. Typical values for a high viscosity liquid are given in table 11.3 below. 89

11.9 The real part of growth rate σ_R sec^{-1} vs. k cm^{-1} for $\hat{\mu} = 0.018$ (water, $\mu_l = 1$ cp), $V = 1500$ cm/sec. The graphs are top to bottom $\alpha = 0.2,\ 0.5,\ 0.8$. The curves of σ_R sec^{-1} along the line of $V =$1500 cm/sec in figure 11.6, are drawn here for respective values of α. Instability may arise for all the disturbances of wavenumbers below the cut-off wavenumber k_C. The maximum growth rate σ_{Rm} and the corresponding wavenumber $k_m = 2\pi/\lambda_m$ for $V = 1500$ and 900 cm/sec are listed with wave velocity $\tilde{C}_{Rm}$ in table 11.4 below. 90

11.10 j^* vs. α is for marginal stability of air and water in a frame in which the water velocity is zero. The heavy line through □ = air-water, our result with $\gamma = 60$ dynes/cm from table 11.1; ◇ = inviscid fluid from table 11.2. $j^* = \alpha^{3/2}$ is the long wave criterion for an inviscid fluid put forward by Wallis & Dobson (1973). $j^* = 0.5\alpha^{3/2}$ was proposed by them as best fit to the experiments $f1.1$ through $f1.9$ described in their paper. The shaded region is from experiments by Kordyban & Ranov (1970). Also shown are experimental data in rectangular conduits $j * vs.1 - h/H = \alpha$ and in round pipes $j * vs.1 - h/D = \alpha$ (Lin & Hanratty 1986, figure 4). 93

11.11 (After Andritsos & Hanratty 1987.) The borders between smooth stratified flow and disturbed flow are observed in experiment. The water-air data is well below the cluster of high viscosity data that is bunched together. 94

11.12 Local liquid velocity U_L versus local gas velocity U_G for PDVSA-Intevep data from 0.508 m i.d. flow loop with air and 0.404 Pa s lube oil. The identified flow patterns are SS (open circles), SW (open squares). Straftified to non-stratified flow transition theories after different authors are compared; TD: stars, BT: +, FJ: broken line, Funada and Joseph multiplied by α (2001) FJ $\times\alpha$ heavy line. Constant void fraction α lines are indicated. Notice that the curves FJ and FJ $\times\alpha$ sharply drop around U_B5 m/s, separating SS data from SW data. 96

11.13 Nonlinear effects. The Taitel-Dukler 1976 correction (multiply by α). 97

11.14 (Varga *et al.* 2003) Schematic of the development of the liquid jet breakup process. 97

11.15 (Varga *et al.* 2003) Sketch of the gas and liquid streamlines in the liquid tongue formation process. 98

11.16 (Varga *et al.* 2003) Instantaneous flow image with identified Rayleigh-Taylor wavelengths, $D_l =$0.32 mm, $We =$37, $\lambda_{\text{measured}} = 200\mu$m. (cf. figures 9.6-9.8) 98

11.17 (Varga *et al.* 2003) Instantaneous flow image with identified Rayleigh-Taylor wavelengths, $D_l =$0.32 mm, $We =$47, $\lambda_{\text{measured}} = 185\mu$m. (cf. Figs. 9.6-9.8) 98

13.1 (Matsumoto *et al.* 1999 ADD TO REFERENCE LIST) Photograph of a toroidal gas bubble in water. 109

13.2 Evolution of the ring radius a and velocity U with time t, according to Pedley. The data for Pedley's solution for U are extracted from figure 3 in Pedley (1968). —□— inviscid solution for a, —◇— Pedley's viscous solution for a, —△— inviscid solution for U, —×— Pedley's viscous solution for U. FIGURE CROPPED NEED NEW FIGURE 110

13.3 Meridional section of the toroidal bubble. 111

13.4 Evolution of the ring radius a with time. The dash-dotted line represents the inviscid solution obtained by putting $\nu = 0$ in (13.5.16). The solid line represents the viscous solution of (13.5.16) with the initial conditions (13.5.19) and (13.5.20). The symbol □ represents the viscous solution of (13.5.21) with the initial condition (13.5.19). 115

13.5 Evolution of the rise velocity U computed from (13.5.5) with time. The dash-dotted line represents the inviscid solution obtained by putting $\nu = 0$ in (13.5.16). The solid line represents the viscous solution of (13.5.16) with the initial conditions (13.5.19) and (13.5.20). The symbol □ represents the viscous solution of (13.5.21) with the initial condition (13.5.19). 115

13.6 The height of rise $h - h_0$ against the ring radius a. The dash-dotted line represents the inviscid solution obtained by putting $\nu = 0$ in (13.5.16). The solid line represents the viscous solution of (13.5.16) with the initial conditions (13.5.19) and (13.5.20). The symbol $\Box$ represents the viscous solution of (13.5.21) with the initial condition (13.5.19). 116

13.7 The ratio between the ring expansion velocity $\dot{a}$ and the rise velocity U obtained from the solution of (13.5.16). 116

13.8 Growth rate $\hat{\sigma}$ as a function of the wavenumber $\hat{k}$ for a cylindrical bubble with circulation $\hat{\Gamma}^2$. Instability takes place for the results shown. Four values of the parameter J are selected. The definition of the dimensionless quantities $\hat{\sigma}$, $\hat{k}$ and $\hat{\Gamma}$ is given in (13.5.45) and $J = \rho\gamma a/\mu^2$. 119

13.9 The path of the cylinder at different Reynolds numbers. —: $R_e \to \infty$; —: R_e=100; —: R_e=20. 122

14.1 Decay rate $-\mathrm{Re}(n)$ vs. wave number k for water, $\nu = 10^{-6}$ m^2/s. $\mathrm{Re}(n)$ is computed for the exact solution from (14.1.32), for VPF from (14.1.36) and for VCVPF from (14.1.41). When $k < k_c$, the decay rate $-2\nu k^2$ for VCVPF is in good agreement with the exact solution, whereas the decay rate $-\nu k^2$ for VPF is only half of the exact solution. When $k > k_c$, n has two real solutions in each theory. In this figure, we plot the decay rate n_1 corresponding to (14.1.34), (14.1.39) and (14.1.44). The exact solution can be approximated by $-g/(2\nu k)$; the decay rate $-g/(2\nu k)$ for VPF is in agreement with the exact solution, whereas the decay rate $-g/(4\nu k)$ for VCVPF is only half of the exact solution. 130

14.2 Decay rate $-\mathrm{Re}(n)$ vs. wave number k for water, $\nu = 10^{-6}$ m^2/s. $\mathrm{Re}(n)$ is computed for the exact solution from (14.1.32), for VPF from (14.1.36) and for VCVPF from (14.1.41). When $k > k_c$, n has two real solutions in each theory. In this figure, we plot the decay rate n_2 corresponding to (14.1.35), (14.1.40) and (14.1.45). The decay rate for the exact solution can be approximated by $-0.91\nu k^2$; the decay rate $\approx -2\nu k^2$ for VPF is closer to the exact solution than the decay rate $\approx -4\nu k^2$ for VCVPF. 131

14.3 $\mathrm{Im}(n)$, i.e. the wave-velocity multiplied by k, vs. wave number k for water, ν=10^{-6}m^2/s. $\mathrm{Im}(n)$ is computed for the exact solution from (14.1.32), for VPF from (14.1.36) and for VCVPF from (14.1.41). When $k < k_c$, the three theories give almost the same wave-velocity. When $k > k_c$, all the three theories give zero imaginary part of n. 131

14.4 Decay rate $-\mathrm{Re}(n)$ vs. wave number k for glycerin, $\nu = 6.21 \times 10^{-4}$m^2/s. $\mathrm{Re}(n)$ is computed for the exact solution from (14.1.32), for VPF from (14.1.36) and for VCVPF from (14.1.41). When $k < k_c$, the decay rate $-2\nu k^2$ for VCVPF is in good agreement with the exact solution, whereas the decay rate $-\nu k^2$ for VPF is only half of the exact solution. When $k > k_c$, n has two real solutions in each theory. In this figure, we plot the decay rate n_1 corresponding to (14.1.34), (14.1.39) and (14.1.44). The decay rate for the exact solution can be approximated by $-g/(2\nu k)$; the decay rate $-g/(2\nu k)$ for VPF is in agreement with the exact solution, whereas the decay rate $-g/(4\nu k)$ for VCVPF is only half of the exact solution. 132

14.5 Decay rate $-\mathrm{Re}(n)$ vs. wave number k for SO10000 oil, $\nu = 1.03 \times 10^{-2}$ m^2/s. $\mathrm{Re}(n)$ is computed for the exact solution from (14.1.32), for VPF from (14.1.36) and for VCVPF from (14.1.41). When $k < k_c$, the decay rate $-2\nu k^2$ for VCVPF is in good agreement with the exact solution, whereas the decay rate $-\nu k^2$ for VPF is only half of the exact solution. When $k > k_c$, n has two real solutions in each theory. In this figure, we plot the decay rate n_1 corresponding to (14.1.34), (14.1.39) and (14.1.44). The decay rate for the exact solution can be approximated by $-g/(2\nu k)$; the decay rate $-g/(2\nu k)$ for VPF is in agreement with the exact solution, whereas the decay rate $-g/(4\nu k)$ for VCVPF is only half of the exact solution. 132

14.6 Decay rate $-\mathrm{Re}(n)$ vs. wave number k for ν=10 m^2/s. Re(n) is computed for the exact solution from (14.1.32), for VPF from (14.1.36) and for VCVPF from (14.1.41). When $k < k_c$, the decay rate $-2\nu k^2$ for VCVPF is in good agreement with the exact solution, whereas the decay rate $-\nu k^2$ for VPF is only half of the exact solution. When $k > k_c$, n has two real solutions in each theory. In this figure, we plot the decay rate n_1 corresponding to (14.1.34), (14.1.39) and (14.1.44). The decay rate for the exact solution can be approximated by $-g/(2\nu k)$; the decay rate $-g/(2\nu k)$ for VPF is in agreement with the exact solution, whereas the decay rate $-g/(4\nu k)$ for VCVPF is only half of the exact solution. 133

14.7 Critical Reynolds number J_c as a function of the mode number ℓ for a *drop* and a *bubble*. At a given ℓ, for $J > J_c$ progressive decaying waves (oscillations) are predicted (i.e. the eigenvalues $\hat{\sigma}$ are complex), whereas for $J \leq J_c$ monotonically decaying waves are obtained (i.e. the eigenvalues $\hat{\sigma}$ are real). The results are presented for VPF, VCVPF and the exact solution. Notice that the exact solution does not provide a crossover value, since the imaginary part is never identically zero. 146

14.8 Decay rate and wave frequency for the fundamental mode $\ell = 2$ as function of the Reynolds number J for a *drop* from the exact solution, VPF, VCVPF and IPF. The decay rate predicted by IPF is identically zero for all ℓ. 147

14.9 Decay rate and wave frequency for the fundamental mode $\ell = 2$ as function of the Reynolds number J for a *bubble* from the exact solution, VPF, VCVPF and IPF. The decay rate predicted by IPF is identically zero for all ℓ. 148

14.10 Decay rate Re($\hat{\sigma}_1$) and wave frequency Im($\hat{\sigma}_1$) for $J = 10^{-3}$ versus the mode number ℓ for a *drop*. For the interval of ℓ shown, the eigenvalues from the viscous theories are real and different. The lowest decay rate is plotted in (a) and the trend exhibited by Im($\hat{\sigma}_1$) is shown in (b) for IPF, which predicts oscillatory waves with constant amplitude. 150

14.11 Decay rate Re($\hat{\sigma}_1$) and wave frequency Im($\hat{\sigma}_1$) for $J = 40$ versus the mode number ℓ for a *drop*. In this case, the eigenvalues are a pair of complex conjugates for the interval of $\ell < \ell_{\mathrm{c}}$ and they are real and different for $\ell \geq \ell_{\mathrm{c}}$. For the latter case, the lowest decay rate is plotted in (a). The symbol ℓ_{c} stands for the highest value of ℓ for which a non-zero imaginary part is obtained, i.e. progressive waves occur. For instance, $\ell_{\mathrm{exact}} = \ell_{\mathrm{c}}$ from fully viscous flow theory (exact solution); analogous definitions can be set for VPF (ℓ_{VPF}) and VCVPF (ℓ_{VCVPF}). 151

14.12 Decay rate Re($\hat{\sigma}_1$) and wave frequency Im($\hat{\sigma}_1$) for $J = 10^6$ versus the mode number ℓ for a *drop*. In this case, the eigenvalues are a pair of complex conjugates for the interval of ℓ considered in this study. 152

14.13 Experimental and theoretical time evolution of shape oscillations of an air bubble in water with oscillation mode (ℓ,m) = (15,0) under ultrasonic vibration of 20 kHz. The bar at the top of the left frame in (a) corresponds to 1.0 mm (Kojo and Ueno 2006). 153

15.1 Floquet theory $a = \mathrm{e}^{\sigma t} b(t)$ for Faraday waves on an inviscid fluid ($N = 0$); $\rho = 0.97$ g/cm^3, $\gamma = 21$ dyne/cm, $g = 981$ cm/sec^2, $\omega = 2\pi \times 15.87$ sec^{-1}, $f = g$ cm/sec^2. (a) $\ln(a)$ vs $t/(2\pi)$, (b) $a\mathrm{e}^{-\sigma t} = b(t) = b(t + 2\pi)$ vs $t/(2\pi)$, (c) $\sigma(N\nu)$ vs k. $\sigma_m = 11.1274$ sec^{-1} at $k_m = 2.4246$ cm^{-1}. 162

15.2 Floquet theory $a = \mathrm{e}^{\sigma t} b(t)$ for Faraday waves on a viscous liquid $\nu = 1$ cm^2/sec with $N = 2$ (VPF); $\rho = 0.97$ g/cm^3, $\gamma = 21$ dyne/cm, $g = 981$ cm/sec^2, $\omega = 2\pi \times 15.87$ sec^{-1}, $f = g$ cm/sec^2. (a) $\ln(a)$ vs $t/(2\pi)$, (b) $a\mathrm{e}^{-\sigma t} = b(t) = b(t + 2\pi)$, (c) σ vs k. $\sigma_m = 5.8790$ sec^{-1} at $k_m = 2.1874$ cm^{-1}. The dissipation theory with $N = 4$ (VCVPF) is stable $\Re\{\sigma\} < 0$. 163

15.3 σ_m versus ν cm^2/sec. 163

15.4 k_m versus ν cm^2/sec. 164

15.5 (a) k_m versus f/g and (b) σ_m versus f/g, for $\nu = 1$ cm^2/sec. (c), (d) σ versus k for $N = 4$ in a transition region, in which the mark $*$ denotes the maximum growth rate. 166

15.6 (a) k_m versus f/g and (b) σ_m versus f/g, for $\nu = 100$ cm^2/sec. 167

15.7 (a) k_m versus f/g and (b) σ_m versus f/g, for $\nu = 300$ cm^2/sec. For small values of f/g the potential flow solutions for Faraday waves are stable, $\sigma_m < 0$ but $N = 2$ is less stable and more like RT waves than $N = 4$. 168

15.8 Dispersion relation for glycerine-water mixture in contact with air at atmospheric pressure. Fitting the experimental data (Edwards & Fauve 1993) with the results of the FHS (solid lines) leads to $\gamma = 67.6 \times 10^{-3}$ N/m. Inset: Fitting of the experimental data for the stability threshold leads to $\nu = 1.02 \times 10^{-4}$ m^2/sec. 169

15.9 f_C/g versus $\omega/(2\pi)$. Based on the data of $\lambda_C = \lambda_C(\omega/(2\pi))$ for their exact solution in figure 15.8 of Kumar & Tuckerman(1994), the critical value f_C/g is estimated for VCVPF and VPF. VPF is closer to the eact solution than VCVPF. $\rho = 1.1848$ g/cm^3, $h = 0.29$ cm, $\nu = 1.02$ cm^2/sec, $\gamma = 67.6$ dnye/cm. 170

16.1 Capillary instability. The force γ/r drives fluid away from the throat, leading to collapse. 173

16.2 (a) The growth rate σ vs. k for case 1, mercury in water. The three potential flow based analyses agree with the exact solution well but deviate from it slightly when $k \ll 1$. (b) The vorticities ω_l^* and ω_a^* vs. k for case 1. The magnitude of the vorticity is large when $k \ll 1$ and small when k is about 1. (c) The two ratios f_l and f_a vs. k for case 1. The irrotational parts dominate when k is close to 1; the irrotational and rotational parts are comparable when $k \ll 1$ or $k \approx 2$. The dominance of the irrotational part in the maximum growth region is understandable because the Reynolds number is very high, 2.080×10^7. Both the vorticities and the two ratios could help to understand the deviation of the potential based analyses from the exact solution when $k \ll 1$. 181

16.3 (a) The growth rate σ vs. k for case 2, water in benzene. The three potential flow based analyses agree with the exact solution in the maximum growth region but deviate from it considerably when k is small. (b) The vorticities ω_l^* and ω_a^* vs. k for case 2. The magnitude of the vorticity is large when $k \ll 1$ and small in the maximum growth region. (c) The two ratios f_l and f_a vs. k for case 2. The ratios are high when k is close to 1 but close to 1 when $k \ll 1$ or $k \approx 2$. The maximum value of f_l is 10.37 here, smaller than the value 66.82 in case 1. The reason is that the Reynolds number in case 2 is smaller than in case 1. Both the vorticities and the two ratios could help to understand the good agreement in the maximum growth region and poor agreement when $k \ll 1$ as shown in (a). 182

16.4 (a) The growth rate σ vs. k for case 3, glycerin in mercury. In the maximum region, IPF and VPF overestimate the growth rate whereas VCVPF gives almost the same value as EXACT. IPF, VPF and VCVPF deviate from the exact solution considerably when $k \ll 1$. (b) The vorticities ω_l^* and ω_a^* vs. k for case 3. The magnitude of the vorticity is large when $k \ll 1$ and small in the maximum growth region. (c) The two ratios f_l and f_a vs. k for case 3. The ratios are high when k is close to 1 but close to 1 when $k \ll 1$ or $k \approx 2$. The maximum value of f_l is 1.83, much smaller than in case 1 and case 2. At the same time the Reynolds number is also much smaller than in case 1 and case 2. It is noted that the maximum value of f_a is 17.19, much larger than f_l. The reason is that the value of f_a should correspond to the Reynolds number based on ρ_a and μ_a, which is 2.08×10^7 in case 3. Both the vorticities and the two ratios could help to understand the good agreement in the maximum growth region and poor agreement when $k \ll 1$ as shown in (a). 183

16.5 (a) The growth rate σ vs. k for case 4, goldensyrup in paraffin. IPF and VPF deviate from the exact solution considerably in the whole range of $k \leq k_c = 2$. VCVPF is still in good agreement with the exact solution in the maximum growth region. (b) The vorticities ω_l^* and ω_a^* vs. k for case 4. The magnitude of the vorticity is large at almost all the values of k except when k is very close to $k_c = 2$. (c) The two ratios f_l and f_a vs. k for case 4. The maximum value of f_l and f_a does not exceed 1.3, indicating that the rotational parts are important in the whole range of k. This could explain the deviation of IPF and VPF from the exact solution in the whole range. At the same time, the curve for f_a shows that the ratio is higher in the maximum growth region than in the region where $k \ll 1$ or $k \approx 2$. This may help to understand the good agreement between VCVPF and the exact solution in the neighborhood of the maximum growth rate. 184

16.6 (a) The growth rate σ vs. k for case 5, goldensyrup in BBoil. The agreement between IPF, VPF and VCVPF with the exact solution is poor at almost all the values of k. (b) The vorticities ω_l^* and ω_a^* vs. k for case 5. The magnitude of the vorticity is relatively large at almost all the values of k, and becomes small only when k is very close to $k_c = 2$. (c) The two ratios f_l and f_a vs. k for case 5. The maximum value of f_l and f_a does not exceed 1.000035, indicating that the irrotational and rotational parts are almost equally important in the whole range of k. Both the vorticities and the two ratios could help to understand the poor agreement between IPF, VPF and VCVPF with the exact solution shown in (a). 185

16.7 The growth rate σ vs. k for case 3, SO100 in air. IPF and VPF slightly overestimate the growth rate in the region near the peak; the curve for the corrected solution (VCPVF) is almost indistinguishable from the exact solution (ES). FVF in the figure should be replaces by ES. 189

16.8 The growth rate σ vs. k for case 4, glycerine in air (a) and for case 5, SO10000 in air (b). The growth rates computed from IPF and VPF deviate considerably from the exact solution (ES), but the growth rates from the corrected solution (VCVPF) are nearly the same as the exact solution (see table 16.4). FVF in the figure should be replaces by ES. 189

16.9 The growth rate σ vs. k for case 5 (inverse), air in SO10000. The growth rate by IPF is significantly larger than that by ES; the results by VPF, VCVPF and ES are almost the same (see table 16.2). FVF in the figure should be replaces by ES. 190

16.10 Functions α, b_a, b and α_a versus real k; these functions tend to one for $k > 10$. The neutral curves of inviscid and viscous potential flow for $\ell = m$ are identical when $k > 10$; this will be seen in (16.2.33). The functions for $k > 10$ will lead to the asymptotic forms (16.2.23), (16.2.24) and (16.2.39)-(16.2.46). 194

16.11 Example of a growth rate curve defined in section 16.2.4, showing the main features: the shape, maximum ω_{Im}, k_m and the cut-off wavenumber k_c. 195

16.12 (a) ω_{Im} versus W^{-1} and (b) k_m versus W^{-1}, for $\ell = 0$ (solid line), 0.0012 (broken line), 0.012 (dashed line), 0.1 (dotted line), 0.3455 (broken dotted line), 0.5 (dash dotted line). For large W^{-1} and $\ell \neq 0$, the curves approach the asymptotic form given respectively by (16.2.23) and (16.2.24). 197

16.13 (a) ω_{Im} versus W^{-1} $(= \rho 2aU^2/\gamma)$ and (b) k_c (the upper curves) and k_m (the lower curves) versus W^{-1} for $R = 100$; the solid curve is for $\ell = 0$ and $m = 0$, the broken line for $\ell = 0.0012$ and $m = 0$, the dashed line for $\ell = 0.0012$ and $m = 0.018$, the dotted line for $\ell = 0$ and $m = 0.018$. Kelvin-Helmholtz (KH) instability for the liquid jet corresponds to $\gamma \to 0$ or $W^{-1} \to \infty$. The neutral curve is independent of the Reynolds number R. If surface tension and gravity are zero, KH flows are unstable for all k (see equation (2.27) in Funada & Joseph 2001). When $U \to 0$, we get capillary instability which is unstable to all waves with $0 < k < 2$. The interval of unstable wave $0 < k < k_c$ increases as the Weber number decreases (larger U, smaller γ). In general, the neutral curve for viscous potential flow lies above that for inviscid potential flow with equality for a given k when $m\alpha b_a = \ell b \alpha_a$ and for large $k > 10$, when $\ell = m$ $(\nu = \nu_a)$ (see eqs(16.2.36)–(16.2.38)). The values $k_m(W^{-1})$ for which the growth is maximum depends on R. The maximum growth rates ω_{Im} are finite for $W \to 0$ but the associated wavenumbers are proportional to $1/W$ for small W. 199

16.14 (a) ω_{Im} versus W^{-1} and (b) k_m versus W^{-1} for $R = 100$, $m = 0$ and various ℓ; $\ell = 0$ (solid line), 0.0012 (broken line), 0.012 (dashed line), 0.1 (dotted line), 0.5 (broken dotted line), 1 (dash dotted line). For large W^{-1} and $\ell \neq 0$, the curves approach the asymptotic form given by (16.2.46). 201

16.15 (a) ω_{Im} versus W^{-1} and (b) k_m versus W^{-1} for $R = 100$, and $m = 0$; $\ell = 0.012$ and $n = 0$ (solid line), $\ell = 0.012$ and $n = 1$ (broken line), $\ell = 0.5$ and $n = 0$ (solid line), $\ell = 0.5$ and $n = 1$ (broken line). 203

16.16 Linear impulse response. (a) Linearly stable flow; (b) linearly convectively unstable flow; (c) marginally convectively/absolutely unstable flow; (d) absolutely unstable flow (after Huerre 2000, figure 8). The pictures here are for a response to a linear impulses; stability cannot be determined from the evolution of impulses alone. Convectively unstable flows in (b) are also temporally unstable; at any x, real wavenumbers exist for which disturbances outside the unstable wedge in (b) will grow. 206

16.17 k_I versus k_R for $\ell = 0$, $R = 100$, $\beta = 4.934$, and $m = 0$. Equation (16.2.14) gives rise to three complex roots k for each prescribed set of parameters; for each of the three k's there is one value of ω_I whose sign is marked on the figure. The value $\beta = 4.934 < \beta_c = 5.134$ is subcritical. The singular point $D = 0$ and $\hat{c} = 0$ (or $c = \partial\omega_R/\partial k_R = 0$) has $\omega_I > 0$ in the subcritical case and the flow is absolutely unstable; this point is not shown but the points • that will merge into a pinch point • in figure 8.2 are identified. The solid curves are given by $D = 0$ and $\omega_I = 0$. The dashed curves are for $D = 0$, $\omega_R = 1.7178$ and $\omega_I \geq 0$. 211

16.18 k_I versus k_R for $\ell = 0$, $R = 100$, $m = 0$, and $\beta = \beta_c = 5.134$ is critical and identified by •. At this point $D = 0$, $\hat{c} = 0$, $(\omega_R, \omega_I) = (1.7304, 0)$ and $(k_R, k_I) = (2.392, -0.496)$. The dashed curve $D = 0$ and $\omega_R = 1.7304$ passes through the critical point and has $\omega_I \leq 0$. 211

16.19 k_I versus k_R for $\ell = 0$, $R = 100$, $m = 0$, and $\beta = 5.334 > \beta_c$ is supercritical. The singular point is shown as a dot • and $\omega_I < 0$ there. On dashed curves $\omega_R = 1.743$. 212

16.20 Cusp point $(\omega_R, \omega_I) = (1.7304, 0)$. ω_I versus ω_R for $\ell = 0$, $\beta = 5.134$, $R = 100$ and $m = 0$; the solid curves are for $D = 0$ and $\hat{c} = 0$, which passes through the pinch point $(k_R, k_I) = (2.392, -0.496)$ in the (k_R, k_I) plane (see figure 16.18). 212

16.21 β_c versus ℓ when $m = 0$; $R = 2000$ $(*)$, 200 $(\times)$, 100 $(+)$. 212

16.22 β_c versus ℓ when $m = 0.5$; $R = 2000$ $(*)$, 200 $(\times)$, 100 $(+)$. 213

16.23 Locus of singular points $D = 0$, $\hat{c} = 0$ for $m = 0$, $\ell = 0$, $R = 100$ (dashed line), $R = 200$ (dash dot line), $R \to \infty$ (solid line) for $10^{-3} \leq \beta \leq 10$. Critical singular points are those for which $\omega_I = 0$. $\beta = 10^{-3}$ $\times$, $\beta_c = 6.246$ $\circ$, $\beta_c = 5.134$ $\square$, $\beta_c = 5.493$ $+$ and $\beta = 10$ $\triangle$. (a) k_I versus k_R, (b) ω_I versus ω_R, (c) $\left(\partial^2\omega/\partial k^2\right)_I$ versus β. $\beta < \beta_c$ is subcritical, $\beta > \beta_c > 0$ is supercritical. The supercritical inviscid branch $R \to \infty$, $\beta > 6.246$ is degenerate $\left(\partial^2\omega/\partial k^2\right)_I = \omega_I = k_I = 0$ there. Disturbances with zero group velocity are neutrally stable. The values of β on the upper branches $k_I > 0$ of the (k_R, k_I) plane are less than $\beta_c = 6.246$ and $\omega_I < 0$. These branches are subcritical and spatially and temporally damped. The lower branches $k_I < 0$ go from subcritical values $10^{-3} < \beta < \beta_c$ for $\omega_I > 0$ (for which the disturbances are spatially and temporally amplified) to supercritical values $\beta > \beta_c$: $\beta_c = 6.246$ for $R \to \infty$ and $\omega_I = 0$, $k_I = 0$ for $\beta > 6.246$, $\beta_c = 5.134$ for $R = 200$ and $\omega_I < 0$ there, $\beta_c = 5.493$ for $R = 100$ and $\omega_I < 0$ there. Disturbances with zero group velocity are temporally damped but spatially amplified ($\omega_I < 0$, $k_I < 0$) for supercritical values of β. 215

16.24 Border between absolute and convective instability in the inviscid case $R \to \infty$, $m = 0$. The value of $\ell = 0.3455$ is asymptotic. The inviscid case is degenerate because the imaginary part of $\partial^2\omega/\partial k^2 = 0$ at the singular point. The consequence of this degeneracy is that at criticality $(\omega_I, k_I) = (0, 0)$ for all $\ell < 0.3455$. The condition $\omega_I < 0$ at the pinch point cannot be realized; ω_I at $\partial\omega_R/\partial k_R = 0$. 216

16.25 Critical Weber number β_c $(= W_c^{-1})$ versus Reynolds number R from the literature: Leib & Goldstein (1986a) for inviscid jet in an inviscid fluid, $\beta_c = 6.3$ for $\ell = 0$, denoted by dashed line; solid lines are for viscous jets in an inviscid fluid ($m = 0$) for $\ell = 0$ (Leib & Goldstein 1986b) and $\ell = 0.0013$ and $\ell = 0.03$ (Lin & Lian 1989). 217

16.26 β_c versus R comparing viscous flow (lower two curves) computed from the theory in section 16.2.10 for $m = 0$, $\ell = 0.0013$ $*$ and $\ell = 0.03$ $\square$ with viscous potential flow (upper two curves) for the same values ($\ell = 0.0013$ $+$, $\ell = 0.03$ $\times$, $m = 0$). 218

16.27 ω_I vs k and ω_R vs k for $\nu = 0$ and $\nu = 0.1$. The problem considered by Batchelor and Gill 1962 is Hadamard unstable $e^{\omega_I t} \to \infty$ as $k \to \infty$, no matter how small is t. $n = 0$ above 223

16.28 Piecewise continuous velocity modeling a shear layer. 223

17.1 Flow through an aperture in a flat plate. 229

17.2 (**a**). The stream and potential functions in the z plane. The x and y coordinates are normalized as $(x/\ell, y/\ell)$. The stream and potential functions are in the range $-C_c < \psi/(\ell U) < 0$ and $-0.375 < \phi/(\ell U) < 1.75$, respectively. The contraction coefficient $C_c = \pi/(2+\pi) = 0.611$ and the edge of the nozzle is at $(x/\ell, y/\ell) = (-1, 0)$. (**b**) The velocity in the z plane. Only half of the flow field is shown due to the symmetry. 232

17.3 Contour plot for $(p - p_v)/(\rho U^2/2)$ in the $(x/\ell, y/\ell)$ plane, (a) $K = 10$; (b) $K = 1000$. In the flow field, $p - p_v > 0$ everywhere. Thus there is no cavitation according to the pressure criterion. 233

17.4 Contour plot for $(T_{11} + p_v)/(\rho U^2/2)$ in the $(x/\ell, y/\ell)$ plane, (a) $K = 10$ and $R_e = 1$; (b) $K = 10$ and $R_e = 5$. Cavitation occurs inside the curve on which $T_{11} + p_v = 0$. Figure 17.3(a) and 17.4(a) can be compared to show the effect of the viscous stress cavitation. 234

17.5 The cavitation threshold curves on which $T_{11} + p_v = 0$ in different flows with $R_e = 1$, 2, 5, 10, 20, 50 and 100. The cavitation number is fixed at $K = 1$ in (a) and $K = 100$ in (b). Cavitation occurs inside the curve on which $T_{11} + p_v = 0$. 235

17.6 The curve on which $T_{11} + p_v = 0$ at the point $(x/\ell = -1.01,\ y/\ell = 0)$ in the R_e vs K plane. Below the curve, $T_{11} + p_v > 0$ and cavitation occurs at the point; above the curve, $T_{11} + p_v < 0$ and there is no cavitation at the point. 235

17.7 Viscous stress contours for Navier-Stokes solution (solid lines) compared to viscous potential flow solution (dashed lines) for ρ-ratio=1e^{-4} and μ-ratio=1.5e^{-4} (Top): Re =500, (Bottom): Re =100. 236

17.8 Viscous stress contours for Navier-Stokes solution (solid lines) compared to viscous potential flow solution (dashed lines) for ρ-ratio=1e^{-4} and μ-ratio=1.5e^{-4} (Top): Re =10, (Bottom): Re =1. 237

17.9 Schematic view of the orientation of the principal directions in the plane of motion for irrotational flow of a viscous fluid according to (17.3.13) on the surface of the sphere. The major axis in the ellipse represents the maximum tensile stress. The angle α puts the direction defined by the unit outward normal vector $\boldsymbol{e}_r$ into the principal direction of the maximum tensile stress. 240

17.10 Contours of critical cavitation number K_c given by the condition $T_{11} + p_\mathrm{c} = 0$ according to the maximum tension criterion for a Reynolds number $Re = 0.01$ from (a) Stokes flow; (b) the irrotational flow of a viscous fluid (17.3.17), and (c) numerical solution; the pressure criterion given by $K_\mathrm{c} = -c_\mathrm{p}$ is shown in (d) using the numerical pressure field. The cavitation number K is defined in terms of the dynamic pressure $\rho U^2/2$. For a given cavitation number K, cavitation occurs in the region where $K < K_\mathrm{c}$. A different normalization of the cavitation number and of the critical cavitation number is used for Stokes flow rather than the normalization used for the other cases (17.3.18). The contour lines for the normalization of $p_\infty - p_\mathrm{c}$ with the viscous-stress scale $\mu U/a$ are presented in parenthesis in (a). The ratio of the normalization factors is $Re/2$. 241

17.11 Contours of critical cavitation number K_c given by the condition $T_{11} + p_\mathrm{c} = 0$ according to the maximum tension criterion for a Reynolds number $Re = 10$ from (a) the irrotational flow of a viscous fluid (17.3.17), and (b) numerical solution; the pressure criterion given by $K_\mathrm{c} = -c_\mathrm{p}$ is shown in (c) using the numerical pressure field. The cavitation number K is defined in terms of the dynamic pressure $\rho U^2/2$. For a given cavitation number K, cavitation occurs in the region where $K < K_\mathrm{c}$. 242

17.12 Contours of critical cavitation number K_c given by the condition $T_{11} + p_\mathrm{c} = 0$ according to the maximum tension criterion for a Reynolds number $Re = 100$ from (a) the irrotational flow of a viscous fluid (17.3.17), and (b) numerical solution; the pressure criterion given by $K_\mathrm{c} = -c_\mathrm{p}$ is shown in (c) using the numerical pressure field. The cavitation number K is defined in terms of the dynamic pressure $\rho U^2/2$. For a given cavitation number K, cavitation occurs in the region where $K < K_\mathrm{c}$. 243

17.13 Periodic structure of stagnation points as a cartoon of the dynamics of capillary collapse. The collapse will give rise to a periodic string of liquid drops. The analysis here is local focusing on dynamics of collapse at $z = 0$. 246

17.14 (Ashgritz and Mashayek, 1995) Time evolution of the instability of a capillary liquid jet, $\epsilon_0 = 0.05$: (a) $k = 0.2$, $Re = 200$, (b) $k = 0.45$, $Re = 200$, (c) $k = 0.7$, $Re = 200$, (d) $k = 0.9$, $Re = 200$, (e) $k = 0.2$, $Re = 10$, (f) $k = 0.45$, $Re = 10$, (g) $k = 0.7$, $Re = 10$, (h) $k = 0.9$, $Re = 10$, (i) $k = 0.2$, $Re = 0.1$, (j) $k = 0.45$, $Re = 0.1$, (k) $k = 0.7$, $Re = 0.1$, (l) $k = 0.9$, $Re = 0.1$. The numbers on the figures indicate the corresponding times. 252

17.15 Liquid-bridge evolution starting from an unstable configuration. The disk diameter is 3.8 cm, the Reynolds number is 3.7×10^{-3}. The outer fluid, which eliminates buoyancy forces, has a viscosity approximately 1000 times smaller than the inner fluid. (Spiegelberg, Gaudet, and McKinley, 1994). 253

17.16 A drop of a glycerol and water mixture, 100 times as viscous as water, falling from a nozzle 1.5 mm in diameter. As opposed to the case of water, a long neck is produced (Shi, Brenner, and Nagel, 1994). 254

18.1 The flow past a circular cylinder (a) without separation of the boundary layer; (b) with separation of the boundary layer. 257

18.2 The pressure drag coefficient C_{D_p} at different radial position $r/(2a)$ computed from numerical simulation (18.1.62) for R_e=400: dash-double-dotted line - q/U_0= 4; dashed line - q/U_0= 5; dash-dotted line - q/U_0= 6. The solid straight line gives C_{D_p} computed from (18.1.61) for R_e=400. Each curve for $C_{D_p}(r)$ has two intersections with the straight line, at which C_{D_p} given by (18.1.61) is equal to C_{D_p} computed from numerical simulation at $r = a + \delta$. 266

18.3 A symmetrical airfoil moving in a liquid at an angle of attack β with a constant velocity U_0. The additional drag on the airfoil computed using the dissipation method is opposite to the moving direction of the airfoil and is defined as negative. 268

18.4 The uniform streaming flow past a rotating cylinder. 272

18.5 Comparison of the coefficient for the pressure drag C_{D_p} as a function of the radial position. (a) R_e=400, q/U_0=4. Our boundary layer analysis: dashed line – using $\delta/a = 0.17$; solid line – using $\delta/a = 0.2$. The results of numerical simulation: □. (b) R_e=400, q/U_0=5. Our boundary layer analysis: dashed line – using $\delta/a = 0.15$; solid line – using $\delta/a = 0.16$. The results of numerical simulation: □. (c) R_e=400, q/U_0=6. Our boundary layer analysis using$\delta/a = 0.14$: solid line. The results of numerical simulation: □. C_{D_p} from our boundary layer analysis can only be computed inside the boundary layer: $a \leq r \leq a + \delta$; C_{D_p} from numerical simulation is plotted up to $r = 2a$. 287

18.6 Comparison of the coefficient for the pressure lift C_{L_p} as a function of the radial position for R_e=400. Our boundary layer analysis: dash-dotted line – q/U_0=4; dashed line – q/U_0=5; solid line – q/U_0=6. Numerical simulation: □ – q/U_0=4; ∇ – q/U_0=5; ♢ – q/U_0=6. C_{L_p} from our boundary layer analysis can only be computed inside the boundary layer: $a \leq r \leq a + \delta$; C_{L_p} from numerical simulation is plotted up to $r = 2a$. 300

18.7 Scheme of the computational domain showing the Cartesian and polar reference coordinate systems. The boundary conditions correspond to: Λ_1, inflow; Λ_2, outflow; Λ_3, zero-shear stress boundaries, and Λ_4, wall with prescribed velocity and no-slip condition. 300

18.8 Influence of the dimensionless position of the outer boundaries (inlet and outlet) $\tilde{H}$ on the lift, drag and torque coefficients for $Re = 400$ and $\tilde{q} = 5.0$ (solid line with △) and $Re = 1000$ and $\tilde{q} = 3.0$ (dashed line with •). 301

18.9 O-type mesh used in the numerical simulations (M125). 301

18.10 Dimensionless vorticity profiles on the surface of the rotating cylinder for $Re = 200$. Present computations: solid line - $\tilde{q} = 3$; dashed line - $\tilde{q} = 4$; dash-dotted line - $\tilde{q} = 5$. Results of Mittal & Kumar (2003): △ - $\tilde{q} = 3$; ⋄ - $\tilde{q} = 4$; □ - $\tilde{q} = 5$. 302

18.11 Pressure coefficient profiles on the surface of the rotating cylinder for $Re = 200$. Present computations: solid line - $\tilde{q} = 3$; dashed line - $\tilde{q} = 4$; dash-dotted line - $\tilde{q} = 5$. Results of Mittal & Kumar (2003): $\triangle$ - $\tilde{q} = 3$; $\diamond$ - $\tilde{q} = 4$; $\Box$ - $\tilde{q} = 5$. 302

18.12 Streamlines for various pairs of Re and $\tilde{q}$. The rotation of the cylinder is counter-clockwise while the streaming flow is from left to right. The stagnation point lies above the cylinder. The stagnation point moves upwards as the peripheral speed $\tilde{q}$ increases for a fixed Re. 303

18.13 Vorticity contours for various pairs of Re and $\tilde{q}$. The negative vorticity is shown as dashed lines. The rotation of the cylinder is counter-clockwise while the streaming flow is from left to right. 304

18.14 Caption in the next page. 305

18.14 Variable vortical region thickness as a function of the angular position θ (solid line) for various pairs of Re and $\tilde{q}$ obtained applying the 1% criterion. In addition, the uniform vortical region thickness $\delta_{1\%}/a$ (dashed line) computed as the average of the profile is included. 306

18.15 Position of the outer edge of the vortical region based on the 1% criterion. The thick-solid line represents the edge of the vortical region with variable thickness. The thick dash-dotted line represents the edge of the vortical region with uniform thickness $\delta_{1\%}/a$. The thin-solid lines represent contours of positive vorticity while the thin-dashed lines represent contours of negative vorticity. The contours only show levels of vorticity with magnitude greater than or equal to 1% of the maximum vorticity magnitude in the fluid domain. The rotation of the cylinder is counter-clockwise while the streaming flow is from left to right. 307

18.16 Caption on the next page. 308

18.16 Pressure coefficient c_p as a function of the radial position $\tilde{r}$ from the surface of the rotating cylinder for various pairs of Re and $\tilde{q}$ for a fixed angle θ: 0° - thin solid line; 45° - solid line with $\triangle$; 90° - dashed line; 135° - dashed line with $\Box$; 180° - dashed line with $\circ$; 225° - solid line with $\triangleleft$; 270° - dashed-dotted line; 315° - dashed line with $\times$. The pressure coefficient profile given in (18.3.7) from the exact solution of the equations of motion for a purely rotary flow due to the spinning of the cylinder under the absence of the free stream is also presented (thick solid line). This pressure profile is independent of θ. The average position of the outer edge of the vortical region $\tilde{r}_\delta$ corresponding to the 1% criterion is included (vertical dashed line). 309

19.1 The form of a typical graph of the growth rate ω_I versus k. ω_{Im} is the maximum growth, $\lambda_m = 2\pi/k_m$ is the wavelength of the fastest growing wave. k_c is the cut-off wavenumber. ω_{Im} and k_m are called peak values. 318

19.2 The growth rate ω_I versus k in the axisymmetric $n = 0$ mode for IPF, using the material parameters (table 19.2) for stationary water and air with $U_a = 0$, 30, 100 and 310.38 m/sec. The values can be converted into dimensionless form (M, W) using table 19.3. 320

19.3 Maximum growth rate ω_{Im} and the associated wavenumber k_m as a function of M for $\mu_\ell = 0$, 1 cP, 300 cP, 8000 cP. The solid line denotes the axisymmetric case ($n = 0$), and the dashed line in figures for μ_ℓ =8000 cP denotes $n = 1$. 323

19.4 Growth rate versus wavenumber for stationary liquid jet ($U_\ell = 0$) in transonic air. U_a =[1, 2, 3, 4, 5, 6, 7] = [290.08, 302.08, 314.08, 326.08, 340.08, 356.08, 370.08] m/s. (a) $\mu_\ell = 0.15$ cP: as U_a increases, the maximum growth rate marked by + increases monotonically without limit. (b) $\mu_\ell = 0.175$ cP: as U_a increases, the maximum growth rate marked by + increases, changes to another peak, attains the maximun near $U_a = 310.38$ m/sec ($M = 1$), and then decreases. (c) $\mu_\ell = 0.5$ cP: as U_a increases, the maximum growth rate marked by + increases, attains the maximun near $U_a = 310.38$ m/sec ($M = 1$), and then decreases. 324

19.5 (a) The maximum growth rate ω_{Im} versus R and (b) k_m versus R, for $M = 0.5$; $n = 0$ in compressible gas (solid line) and $n = 1$ in compressible gas (dashed line). 325

19.6 (a)The maximum growth rate ω_{Im} versus R and (b) k_m versus R, for $M = 2$; $n = 0$ in compressible gas (solid line) and $n = 1$ in compressible gas (dashed line). 326

19.7 (a) The maximum growth rate ω_{Im} versus W^{-1},(b) k_m versus W^{-1}. VPF, $M = 0.5$ for $\mu_\ell = 300$ cP; $n = 0$ in compressible gas (solid line) and $n = 1$ in compressible gas (dashed line). 327

20.1 Cylinders falling in (a) Newtonian fluid (glycerin), and (b) viscoelastic fluid (2% aqueous PEO solution). In (a), the cylinder is turned horizontal by inertia; in (b), it is turned vertical by viscoelastic pressures 336

20.2 (a) Spheres in Newtonian Fluids. Spheres settling in glycerin draft (i-ii), kiss (iii), and tumble (iv-vi). They tumble because a pair of kissing spheres acts like a long body, which is unstable when its long axis is parallel to the stream. The forces in a Newtonian fluid are dispersive; the tumbling spheres are pushed apart by pressures at stagnation points between the spheres (v-vi). (b) Spheres in non-Newtonian Fluids. Spheres falling in a 2% aqueous PEO solution draft, kiss, and chain. They chain because the forces in a viscoelastic fluid are aggregative. A chain of spheres turn just like the solid cylinder in Figure 20.1.b (i-vi). Reversing time, we see that chaining, kissing, and drafting in b(vi-i) are like drafting, kissing, and tumbling in a(i-vi). 337

20.3 (a1, a2) Side-by-side sphere-sphere interactions; (b1, b2) Sphere-wall interactions; (c) A sphere in a viscoelastic liquid is sucked to a tilted wall; (d) Spheres dropped between widely-spaced walls. The dotted line is the critical distance d_{cr} for wall-sphere interaction. When $d < d_{cr}$, the sphere goes to the wall. When $d > d_{cr}$, the sphere seeks the center. 337

20.4 A 2% suspension of glass spheres (60-70 μm in size) in a highly viscoelastic polymer solution of 0.5% polyacrylamide in deionized water. (a) After loading - the particles are randomly distributed. (b) After a sideways movement on the top plate of about 3 cm. (c) After the top plate had been moved back and forth several times. (d) After further and faster movement of the top plate. (From Michele et al. 1977) 338

20.5 10% suspension of glass spheres (60-70 μm) in a polyisobutylene solution. (a) After movement on the top plate back and forth. (b) After further movement. The lines of spheres in (a) are more or less equally spaced. Further association is observed in (b) where two lines come together. (Michele et al. 1977) 339

20.6 Flow induced microstructure. Spheres line up in the direction of flow (a) Extensional flow, (60-70 μm spheres) (b) fluidization (3 cm spheres) and (c) sedimentation (3 cm spheres) in a 1% aqueous PEO solution. 339

20.7 The dimensionless normal stress T^*_{rr} as a function of the angle θ. Parameters of the liquid M1 are used in the calculation: $\rho = 0.895$ g/cm^3, $\alpha_1 = -3$ and $\alpha_2 = 5.34$ g/cm. The three curves in the figure correspond to $R_e = 1$, $a = 1$ cm; $R_e = 0.05$, $a = 1$ cm; and $R_e = 1$, $a = 0.5$ cm, respectively. 340

20.8 The streamlines of the flow over an ellipse. (a) The angle of attack $\alpha = 0°$; (b) $\alpha = 60°$. 341

20.9 The dimensionless normal stresses T^*_{nn} at the front and rear stagnation points as functions of the Reynolds number. The other two parameters are fixed: $-\alpha_1/\left(\rho a^2\right) = 3$ and $a/b = 1.67$. 343

20.10 The distribution of the dimensionless normal stress T^*_{nn} at the surface of the ellipse in flows with $-\alpha_1/\left(\rho a^2\right) = 3$ and $a/b = 1.67$. The Reynolds number is 1.0 in figures (a) and (b), and is 0.05 in figures (c) and (d). The normal stress is represented by vectors at the surface of the ellipse in (a) and (c), and is plotted against the polar angle θ in (b) and (d). 343

20.11 The dimensionless normal stresses T^*_{nn} at the front and rear stagnation points as functions of the parameter $-\alpha_1/\left(\rho a^2\right)$. The other two parameters are fixed: $R_e = 0.1$ and $a/b = 1.67$. 344

20.12 The dimensionless normal stresses T^*_{nn} at the front and rear stagnation points as functions of the aspect ratio a/b. The other two parameters are fixed: $R_e = 0.1$ and $-\alpha_1/\left(\rho a^2\right) = 3$. 344

20.13 The distribution of the dimensionless normal stress T^*_{nn} at the surface of the ellipse in flows with $R_e = 0.1$ and $-\alpha_1/\left(\rho a^2\right) = 3$. The aspect ratio is 5.0 in figures (a) and (b), and is 1.1 in figures (c) and (d). The normal stress is represented by vectors at the surface of the ellipse in (a) and (c), and is plotted against the polar angle θ in (b) and (d). 345

20.14 The moment on the ellipse in potential flow. (a) In an inviscid fluid, the high pressures at the stagnation points turn the ellipse broadside-on (across the stream); (b) In a second order fluid, the normal stresses at the two edges where the streamlines are most crowded are compressive and tend to turn the ellipse into the stream. At the two stagnation points, the stresses may change from compression to tension. Here we illustrate the situation in which the stress is compression at the front stagnation point and tension at the rear stagnation point; this pair of stresses gives rise to the moment which tends to turn the ellipse into the stream. Our calculation shows that the resultant moment of the normal stress tends to turn the broad side of the ellipse into the stream when inertia is not dominant. 345

20.15 The moment on the ellipse by the normal stress as a function of the attack angle α in the range $[0,\ \pi/2]$. The six curves correspond to six values of the parameter $-\alpha_1/\left(\rho a^2\right)$: 0, 1, 2, 3, 4 and 5; the aspect ratio is fixed at $a/b = 1.67$. 346

20.16 The moment on the ellipse by the normal stress as a function of the attack angle α in the range $[0,\ \pi/2]$. The five curves correspond to five values of the aspect ratio $a/b = 1.1$, 4, 6, 8 and 10; the parameter $-\alpha_1/\left(\rho a^2\right)$ is fixed at 3. 346

20.17 Two orthogonal views showing the cusped (a) and broad (b) shape of the trailing edge of an air bubble (2 cm^3), rising in a viscoelastic liquid (S1). The two photographs are from Liu, Liao & Joseph (1995). 349

20.18 The mapping planes for a Joukowski airfoil. In the ζ plane, the center of the circle is displaced a distance m from the origin at an angle δ from the x axis and it is in the second quadrant. The center of the mass in the z plane (x_0, y_0) is marked. 351

20.19 The normal stress on the airfoil surface as a function of the angle θ. The solid line corresponds to the inviscid Newtonian fluid with $R_e = \infty$, the dashed line to the viscous Newtonian fluid with $R_e = 10$, and the dash-dotted line to the viscoelastic fluid with $R_e = 10$ and $\beta = 0.01$. 354

20.20 The magnitude of C_L and C_D on an airfoil in the flow of a foam measured by DAG2004 against the Reynolds number. The drag is in the uniform flow direction; the direction of the lift force is opposite to what would be predicted from the theory of aerodynamics. 355

21.1 Stages in the breakup of a drop of 2% aqueous solution of polyox (WSR 301; diameter = 2.9 mm) in the flow behind a Mach 2 shock wave. Air velocity = 432 m s^{-1}; dynamic pressure = 165.5 kPa; Weber number =15,200. Time (μs): (a) 0, (b) 55, (c) 95, (d) 290, (e) 370, (f) 435. 357

21.2 Stages in the breakup of a drop of 2% aqueous solution of polyox (WSR 301; diameter = 2.9 mm) in the flow behind a Mach 3 shock wave. Air velocity = 755 m s^{-1}; dynamic pressure = 587.2 kPa; Weber number =54,100. Time (μs): (a) 0, (b) 30, (c) 45, (d) 170, (e) 195, (f) 235. 357

21.3 Stages in the breakup of a drop of 2% aqueous solution of polyacrylamide (Cyanamer N-300LMW; diameter =3.2 mm) in the flow behind a Mach 3 shock wave. Air velocity = 771 m s^{-1}; dynamic pressure = 578.1 kPa; Weber number =82,200. Time (μs): (a) 0, (b) 45, (c) 60, (d) 90, (e) 145, (f) 185, (g) 225. 358

21.4 Stripping breakup of a drop of 1 kg m^{-1} s^{-1} silicone oil (diameter = 2.6 mm) in the flow behind a Mach 3 shock wave. Air velocity = 767 m s^{-1}; dynamic pressure = 681.0 kPa Weber number =168,600. Time (μs): (a) 15, (b) 40, (c) 50, (d) 80, (e) 115, (f) 150. 358

21.5 Distance traveled vs. time. $x - x_0 = \alpha(t - t_0)^2$ where x_0 and t_0 are the extrapolated starting values from the curve fitting technique. The starting values x_0 and t_0 are uncertain within several pixels and several frames (5 μs per frame). 360

21.6 The growth rate n versus the wavenumber k from (21.1.15) for 2% PO ($M_s = 2$); $\lambda_1 = 0.21$ s. The average wavelength and scatter from a very early time in the experiment are indicated. 364

21.7 The growth rate n versus the wavenumber k from (21.1.15) for 2% PO ($M_s = 3$); $\lambda_1 = 0.21$ s. The average wavelength and scatter from a very early time in the experiment are indicated. 364

21.8 The growth rate n vs. the wavenumber k from (21.1.15) for 2% PAA ($M_s = 3$); $\lambda_1 = 0.034$ s. The average wavelength and scatter from a very early time in the experiment are indicated. Also shown by dotted lines are the average wavelength and scatter for the set of waves of small wavelength which appear to be superimposed on the long wavelength waves. 365

21.9 The effect of acceleration on the dispersion relation for 2% PO; $\lambda_1 = 0.21$ s, $\lambda_2 = 3.3 \times 10^{-4}\lambda_1$. 366

21.10 Rayleigh-Taylor waves in 2% PO. 366

21.11 Rayleigh-Taylor waves in 2% PAA. 366

21.12 Droplet configurations for 2% PAA, 2% PO, and two different silicone oils 170 μs after passing of the shock over the drop under the same conditions ($M_s = 3$). The top pair of photographs compares PAA with a silicone oil of approximately the same viscosity (1 kg m^{-1} s^{-1}). The bottom pair compares 2% PO (viscosity = 35 kg m^{-1} s^{-1}) with a silicone oil that has a viscosity of about one-third that of the PO (10 kg m^{-1} s^{-1}). 368

21.13 Capillary instability. The force γ/r drives fluid away from the throat, leading to collapse. 369

21.14 The growth rate σ vs. k from inviscid potential flow (IPF), viscoelastic potential flow (VPF), viscoelastic correction of VPF (VCVPF) and the exact solution. The growth rates for the exact solution and VCVPF are almost the same. The fluid is 2% PAA, ρ =0.99 g cm^{-1}, μ =96 P, γ =45.0 dyn cm^{-1}, λ_1 =0.039 s, $\lambda_2 = 0$ s, $J = 4.834 \times 10^{-3}$, $\hat{\lambda}_1$ =0.263. 374

21.15 The growth rate σ vs. k from inviscid potential flow (IPF), viscoelastic potential flow (VPF), viscoelastic correction of VPF (VCVPF) and the exact solution. The results of the exact solution and VCVPF are almost the same. The fluid is 2% PEO, $\rho = 0.99$ g cm^{-1}, $\mu = 350$ P, $\gamma = 63.0$ dyn cm^{-1}, $\lambda_1 = 0.21$ s, $\lambda_2 = 0$ s, $J = 5.091 \times 10^{-4}$, $\hat{\lambda}_1 = 1.676$. 375

21.16 The growth rate σ vs. k from inviscid potential flow (IPF), viscoelastic potential flow (VPF), viscoelastic correction of VPF (VCVPF) the exact solution. $J = 10^{-4}$, $\hat{\lambda}_1 = 0.1$, $\hat{\lambda}_2 = 0$. 375

21.17 The growth rate σ vs. k from inviscid potential flow (IPF), viscoelastic potential flow (VPF), viscoelastic correction of VPF (VCVPF) and the exact solution. $J = 10^{-4}$, $\hat{\lambda}_1 = 1000$, $\hat{\lambda}_2 = 0$. 376

21.18 The growth rate σ vs. k from inviscid potential flow (IPF), viscoelastic potential flow (VPF), viscoelastic correction of VPF (VCVPF) and the exact solution. $J = 10^{-4}$, $\hat{\lambda}_1 = 1000$, $\hat{\lambda}_2 = 100$. 376

21.19 The growth rate σ vs. k from inviscid potential flow (IPF), viscoelastic potential flow (VPF), viscoelastic correction of VPF (VCVPF) and the exact solution. $J = 10^4$, $\hat{\lambda}_1 = 0.1$, $\hat{\lambda}_2 = 0$. When the Reynolds number J is large, viscoelastic effects are relatively small, and the four curves are close; but differences among them can be seen near the peak growth rate. The inset is the amplified plot for the region near the peak growth rate. VCVPF is the best approximation to the exact solution. 377

21.20 The part of the stream function depending on r defined in (21.2.52), (21.2.53) and (21.2.54) for viscoelastic potential flow (VPF), viscoelastic correction of VPF (VCVPF) and the exact solution respectively. The fluid is 2% PAA, $J = 4.834 \times 10^{-3}$, $\hat{\lambda}_1 = 0.263$, $\hat{\lambda}_2 = 0$. The wave number for the maximum growth rate $k_m = 0.2135$ is chosen for the comparison. 379

21.21 The part of the stream function depending on r defined in (21.2.52), (21.2.53) and (21.2.54) for viscoelastic potential flow (VPF), viscoelastic correction of VPF (VCVPF) and the exact solution respectively. In this case, $J = 10^{-4}$, $\hat{\lambda}_1 = 1000$, $\hat{\lambda}_2 = 0$. The wave number for the maximum growth rate $k_m = 1.170$ is chosen for the comparison. 379

21.22 The part of the stream function depending on r defined in (21.2.52), (21.2.53) and (21.2.54) for viscoelastic potential flow (VPF), viscoelastic correction of VPF (VCVPF) and the exact solution respectively. In this case, $J = 10^{-4}$, $\hat{\lambda}_1 = 1000$, $\hat{\lambda}_2 = 100$. The wave number for the maximum growth rate $k_m = 0.2186$ is chosen for the comparison. 380

21.23 The growth rate σ as a function of k computed using (21.2.60) given by Chang *et al.*, (21.2.38) given by our VCVPF method, and (21.2.17) given by the exact solution. The fluid is water with $\rho = 1000$ kg/m^3, $\mu = 0.001$ kg/(m s), $\gamma = 0.0728$ N/m. The diameter of the liquid cylinder is assumed to be 0.01 m and the Reynolds number is $J = 7.28 \times 10^5$. 381

21.24 The growth rate σ as a function of k computed using (21.2.60) given by Chang *et al.*, (21.2.38) given by our VCVPF method, and (21.2.17) given by the exact solution. The fluid is a Newtonian fluid SO10000 oil with $\rho = 969$ kg/m^3, $\mu = 10$ kg/(m s), $\gamma = 0.021$ N/m. The Reynolds number is $J = 2.04 \times 10^{-3}$. 382

21.25 The growth rate σ as a function of k computed using (21.2.60) given by Chang *et al.*, (21.2.38) given by our VCVPF method, and (21.2.17) given by the exact solution. The fluid is 2% PAA with $J = 4.834 \times 10^{-3}$, $\hat{\lambda}_1 = 0.263$, $\hat{\lambda}_2 = 0$. 382

21.26 The growth rate σ as a function of k computed using (21.2.60) given by Chang *et al.*, (21.2.38) given by our VCVPF method, and (21.2.17) given by the exact solution. The fluid is a viscoelastic fluid with $J = 10^{-4}$, $\hat{\lambda}_1 = 1000$, $\hat{\lambda}_2 = 0$. 383

21.27 The growth rate σ as a function of k computed using (21.2.60) given by Chang *et al.*, (21.2.38) given by our VCVPF method, and (21.2.17) given by the exact solution. The fluid is a viscoelastic fluid with $J = 10^{-4}$, $\hat{\lambda}_1 = 1000$, $\hat{\lambda}_2 = 100$. 383

22.1 Periodic progressive wave with period $L = 2\pi/k$ and speed c. The velocity is given by a harmonic potential, with a zero horizontal average $\overline{\nabla\phi} = 0$ which as $y \to -\infty$, at great depths. The unsteady wave is produced by initially applying an asymmetric distribution of pressure to a symmetric progressive wave. It is striking that they were able to compute the shape of breaking surface waves (Fig. 22.2). 388

22.2 (Figure 8 of Longuet-Higgins and Cokelet 1976) Close-up of the wave crest at successive times. 388

22.3 One wavelenth in the z-plane transformed to a closed domain in the ζ-plane by (22.4.5). Parameters relating boundary points P to field points Q. 390

List of Tables

8.1 Selection of $e(E_o)$ for 12 cases of E_o. The deviation is given by $\delta e = e - e_o$ with (8.3.1) and $F_{r\infty}$ is computed by (8.2.35). 48

9.1 Values of the wave number, wave length, and growth rate of the most dangerous wave for the experimental conditions given in tables 1 and 2 of JBB. 62

10.1 The coefficients for the forces on the cylinder by the pressure and the normal viscous stress obtained from numerical integration. 73

11.1 Typical values of the neutral curves in figure 11.6 for air-water with ρ_a =0.0012 g/cm^3, μ_a =0.00018 poise, ρ_l =1.0 g/cm^3, μ_l =0.01 poise, g =980.0 cm/sec^2, γ =60.0 dynes/cm, H =2.54 cm. (This table was based upon the results of computation that the neutral curves with α =0.1 and 0.2 in figure 11.6 increase monotonically from the values V_s cm/sec at k =10^{-3} cm^{-1}; the curve with α =0.3 in figure 11.6 increases from the value V_s cm/sec at k =10^{-3} cm^{-1}, takes a maximum V =651.3 cm/sec at k =0.692 cm^{-1}, and then takes a minimum V_c =572.5 cm/sec (the critical) at k_c =3.893 cm^{-1}; for the other values of α, the corresponding curves give the critical V_c at k_c.) 87

11.2 Typical values of the neutral curves in figure 11.7 for air-water (as inviscid fluids) with ρ_a =0.0012 g/cm^3, μ_a =0.0 poise, ρ_l =1.0 g/cm^3, μ_l =0.0 poise, g =980.0 cm/sec^2, γ =60.0 dynes/cm, H =2.54 cm. 88

11.3 Typical values of the neutral curves for air-high viscosity liquid with ρ_a =0.0012 g/cm^3, μ_a =0.00018 poise, ρ_l =1.0 g/cm^3, μ_l =50.0 poise, g =980.0 cm/sec^2, γ =60.0 dynes/cm, H =2.54 cm; thus $\hat{\mu} = 3.6 \times 10^{-6}$. This corresponds to a high viscosity case in figure 11.8. (The curves with $\hat{h}_a = 0.5$ through 0.8 take almost the same minimum value at $k = k_c$, though the values at $k = 10^{-3}$ cm^{-1} change as V_s = 1018-1287 cm/sec and $\tilde{C}_{Rs}$ =0.0011-0.0003 cm/sec.) (see table 11.4 for the maximum growth rate.) 89

11.4 Wave number, wave length and wave speed for the maximum growth rate (11.3.49). 91

14.1 The value of each term in (14.1.30) normalized by A^E for SO10000 oil at different wave numbers; term1 $= \partial\left(\phi^J - \phi^E\right)/\partial t$, term2 $= g(\eta^J - \eta^E)$, term3 $=2\nu\partial^2\left(\phi^J - \phi^E\right)/\partial y^2$, and term4 $= 2\nu\partial^2\psi^E/\partial x\partial y$. 128

14.2 The values for the cutoff wave number k_c for water, glycerin, SO10000 oil and the liquid with ν= 10 m^2/s. k_c decreases as the viscosity increases. 130

16.1 The properties of the five pairs of fluids used to study capillary instability and the controlling dimensionless parameters l, m and J. 178

16.2 Data of the maximum growth rate and the associated wave-number. 180

16.3 The properties of five fluids surrounded by air used to study capillary instability and the Reynolds number $J = Oh^2$ where Oh is the Ohnesorge number. 188

16.4 Maximum growth rate σ_m and the associated wavenumber k_m for VCVPF and ES in the 5 cases shown in table 16.1 (A) and in the 5 inverse cases (B) (see § 7), e.g. air-mercury. 190

16.5 Data of various liquid-gas cases. 204

16.6 Parameters of the growth rate curves identified in figure 16.11 for the 10 cases of liquid-gas flow in Table 16.5. Viscous (VPF) and (IPF) are compared. 205

16.7 Critical values of $\beta = \beta_c(\ell, R, m)$ at a generic singular point ($D = 0$, $\hat{c} = 0$). At such a point the group velocity $\partial\omega_R/\partial k_R = 0$, (k_R, k_I) is a pinch point; (ω_R, ω_I) is a cusp point. A critical singular point also has $\omega_I = 0$. When $\beta < \beta_c$ the flow is subcritical (absolutely unstable) and disturbances with zero group velocity are amplified ($\omega_I > 0$, $k_I < 0$). When $\beta > \beta_c$ (convectively unstable) these disturbances decay temporally ($\omega_I < 0$, $k_I < 0$). 214

16.8 Inviscid fluids ($R \to \infty$, $m = 0$). Values of (k_R, k_I) at pinch point singularity (see figure 16.24) indexed by the density ratio ℓ. The values of the frequency ω_R and the Weber number parameter β ($= W^{-1}$) are at the pinch point are also listed. Pinch point singularities do not exist when $\ell > 0.3455$; in this case all flows are absolutely unstable. 216

18.1 Comparison of the coefficients for the pressure lift and torque on the cylinder obtained from Glauert's solution, the simple modification of Glauert's solution and numerical simulation. In the simple modification of Glauert's solution, we use an effective boundary layer thickness δ_L/a, which is determined by matching C_{L_p} computed from our simple modification (18.1.49) to the results of numerical simulation. For (R_e, q/U_0)=(1000, 3), $\alpha > 1$ for both our simple modification and Glauert's solution. These solutions are not expected to converge to the true results. 264

18.2 The values of δ_{D1}/a and δ_{D2}/a at which C_{D_p} given by (18.1.61) is equal to C_{D_p} computed from numerical simulation (18.1.62). The magnitude of the vorticity on the circle with the radius $r = a + \delta_{D1}$ or $r = a + \delta_{D2}$ was estimated from the numerical data and expressed as a certain percentage of the maximum magnitude of the vorticity field. This percentage is between 12.6% to 20.4% at $r = a + \delta_{D1}$ and is between 0.003% to 0.913% at $r = a + \delta_{D2}$. 267

18.3 The calculation of C_{L_p} (18.1.49) and C_T (18.1.44) on the cylinder using δ_{D1}/a determined by matching C_{D_p} as an effective boundary layer thickness. The results are in fair agreement with the numerical data shown in table 18.1. This demonstrates that δ_{D1}/a can be used not only as an effective boundary layer thickness for C_{D_p}, but also for C_{L_p} and C_T. 267

18.4 The integral I as a function of the attack angle β and the nose sharpness parameter ε (the smaller ε, the sharper the nose). The drag coefficient can be obtained by $C_D = -I/(2R_e^{'})$, where the Reynolds number $R_e^{'} = \dfrac{\rho U_0 c}{\mu}$. Here $c \approx l/4$, where l is the length of the airfoil. 269

18.5 The comparison of the coefficients for the drag, lift and torque with the simulation results for $R_e = 200$ and q/U_0=4. The lift and torque computed using δ/a =0.24, 0.25 or 0.26 are in reasonable agreement with the results of numerical simulation. The drag, especially the drag due to the pressure, does not agree well with the simulation results. When δ/a=0.28, the value of q/Q is such that $\alpha = 2U_0/Q > 1$, which makes the power series expansions of the solutions in terms of α divergent. The calculation can be performed but cannot be expected to converge to the true result. 283

18.6 The comparison of the coefficients for the drag, lift and torque with the simulation results for $R_e = 200$ and q/U_0=5. The lift and torque computed using δ/a =0.2, 0.21 or 0.22 are in excellent agreement with the results of numerical simulation. The agreement of drag, especially the drag due to the pressure, is not good. When δ/a=0.35, $\alpha = 2U_0/Q > 1$, and the power series expansions of the solutions in terms of α are divergent. 283

18.7 The comparison of the coefficients for the drag, lift and torque with the simulation results for $R_e = 400$ and q/U_0=4. The lift and torque computed using δ/a =0.17 or 0.18 are in excellent agreement with the results of numerical simulation. The agreement of drag, especially the drag due to the pressure, is not good. When δ/a=0.23, $\alpha = 2U_0/Q > 1$, and the power series expansions of the solutions in terms of α are divergent. 284

18.8 The comparison of the coefficients for the drag, lift and torque with the simulation results for $R_e = 400$ and q/U_0=5. The lift and torque computed using δ/a =0.14 or 0.15, and the drag computed using δ/a =0.16 are in good agreement with the results of numerical simulation. When δ/a=0.25, $\alpha = 2U_0/Q > 1$, and the power series expansions of the solutions in terms of α divergent. 284

18.9 The comparison of the coefficients for the drag, lift and torque with the simulation results for $R_e = 400$ and q/U_0=6. The drag, lift and torque computed using $\delta/a = 0.14$ are in excellent agreement with the results of numerical simulation. The calculation is reasonable accurate in the range $0.135 \leq \delta/a \leq 0.145$. 285

18.10 The comparison of the coefficients for the drag, lift and torque with the simulation results for $R_e = 1000$ and q/U_0=3. The lift and torque computed using $\delta/a = 0.1$ or 0.12 are close to the results of numerical simulation. However, it should be noted that $\alpha = 1.17 > 1$ when $\delta/a = 0.12$ and the power series expansions of the solutions in terms of α divergent. This is caused by the relatively low value of the speed ratio $q/U_0 = 3$. If Glauert's solution is used for this case, $\alpha = 1.064$ and Glauert's solution also diverges. 285

18.11 The comparison of the solution in this work, using δ/a=0.25, 0.21, 0.17, 0.15, 0.14 and 0.12 for (R_e, q/U_0)= (200, 4), (200, 5), (400, 4), (400, 5), (400, 6) and (1000, 3) respectively, with the simulation results and Glauert's and Moore's solutions. Note that in our problem, the drag on the cylinder is negative if it is in the uniform flow direction; the drag is positive if it is opposite to the uniform flow direction (see figure 18.4). We call the readers' attention to the fact that $\alpha > 1$ in our solution and in Glauert's solution when (R_e, q/U_0) = (1000, 3); the solutions are not expected to converge to the true results. 286

18.12 Properties of the meshes considered in the numerical simulations. 293

18.13 Comparison between the lift and drag coefficients acting on the surface of the rotating cylinder, C_L and C_D, computed in the present study with the results of Mittal & Kumar (2003). 294

18.14 Radial position of the outer edge of the vortical region $\tilde{r}_\delta$ and thickness of the vortical region $\delta_{1\%}/a$ based on the 1% of the maximum vorticity magnitude criterion for various pairs of Re and $\tilde{q}$. 296

18.15 Numerical results for the lift and drag coefficients, C_L and C_D, corresponding to the forces acting on the cylinder. The decomposition of these values in their corresponding components from pressure (C_{L_p} and C_{D_p}) and viscous shear stress (C_{L_f} and C_{D_f}) are included. 297

18.16 Comparison between the numerical results for the dissipation $\tilde{\mathcal{D}}$ determined through numerical integration of (18.3.10) and the predictions from (18.3.11) assuming irrotational flow of a viscous fluid in the entire domain for various Re and $\tilde{q}$. Computed contributions from inside and outside the vortical region (VR) are included. The radial position of the outer edge of the vortical region $\tilde{r}_\delta$ is determined by matching C_{D_p} given by the VCVPF analysis in §18.1 and the corresponding numerical results. 298

19.1 Representative dimensional parameters of sound waves. $\frac{4v_0}{3C_0^2}$ and $\frac{4}{3}\frac{v_0}{C_0}$ are time and length scales respectively (equation (19.1.16)). $k\frac{3C_0}{4v_0}$ is the cut-off wave number and $w_1\frac{3C_0^2}{4v_0} = w_2\frac{3C_0^2}{4v_0}$ is the frequency when k is the cut-off wave number (equation (19.2.1)). $k_1\frac{3C_0}{4v_0}$ and $k_2\frac{3C_0}{4v_0}$ are the wave numbers when the frequency of the sound wave $w\frac{3C_0^2}{4v_0} = 10^9$ s^{-1} (equation (19.2.2)). The values are calculated using the properties of the liquids at 15°C : $\rho_{\mathrm{w}} = 1$ g/cm^3, $\mu_{\mathrm{w}} = 0.0114$ g/cm sec, $C_{\mathrm{w}} = 1.48 \times 10^5$ cm/sec for water; $\rho_{\mathrm{w}} = 1.26$ g/cm^3, $\mu_{\mathrm{w}} = 23.3$ g/cm sec, $C_{\mathrm{w}} = 1.9 \times 10^5$ cm/sec for glycerin. 313

19.2 Properties of air-water. 319

19.3 Typical values and nondimensional parameters for various U_a ($U_\ell = 0$). 321

19.4 Maximum growth rate parameters (figure 19.2) for different values of M: (a) IPF; (b) $\mu_\ell = 1$ cP, $m = 1.8 \times 10^{-2}$; (c) $\mu_\ell = 300$ cP, $m = 6 \times 10^{-5}$; (d) $\mu_\ell = 8000$ cP, $m = 2.25 \times 10^{-6}$. 322

20.1 The lift, drag and torque coefficients on a Joukowski airfoil in the potential flow of a second-order fluid as a function of the controlling parameters R_e and β (20.15.4). The profile of the airfoil is determined by $m = 0.0911$ and $\delta = 0.688\pi$, and the angle of attack is fixed at $\alpha = 0$. 354

21.1 359

21.2 Curve-fitting parameters and initial accelerations for the liquid drops specified in table 21.1. 360

21.3 2% PO ($M_s = 2$). Values of the wavenumber k, wavelength l and growth rate n of the most dangerous wave for the experimental conditions given in tables 21.1 and 21.2; the retardation time λ_2 is changed against the relaxation time λ_1. The values of k and n predicted by viscoelastic potential theory are higher than the corresponding fully viscoelastic predictions. The differences are indicated as a percentage of the fully viscoelastic values. 365

21.4 As table 21.3 but for 2% PO ($M_s = 3$). 365

21.5 As table 21.3 but for 2% PAA ($M_s = 3$). 365

21.6 Comparison of measured breakup times (defined as the time at which liquid first starts to 'blow-off' the perimeter of the drop) with predicted times $\hat{t}_b$ calculated from equation $\hat{t}_b = \ln M/n$ with $M = 10$ and using values of n from the fully viscoelastic analysis. 368

21.7 Maximum growth rate σ_m and the associated wavenumber k_m for viscoelastic potential flow (VPF), viscoelastic correction of VPF (VCVPF) and the exact solution in Figs. 21.14–21.19. For inviscid potential flow (IPF) solution, k_m =1.394 and σ_m =0.9711 in all the 6 cases. 377

21.8 The growth rate σ computed from viscoelastic potential flow (VPF), viscoelastic correction of VPF (VCVPF) and the exact solution at the same wave number k_m. In the exact solution, k_m is the wave number for the maximum growth rate. 378